The Relationship between the Composition and Mechanical Properties of Articular Cartilage

Submitted by James Stephen Bell, to the University of Exeter as a thesis for the degree of Doctor of Philosophy in Physics, December 2010.

I certify that all material in this thesis which is not my own work has been identified and that no material has previously been submitted and approved for the award of a degree by this or any other University.

.....James Bell

Abstract

Articular cartilage (AC) is a soft connective tissue that lines the ends of synovial bones in joints. It is responsible for absorbing impact loads and resisting shear associated with joint articulation. Pathologies such as osteoarthritis have symptoms including degradation and sometimes complete loss of the articular cartilage, which can lead to poor load support and considerable pain. There has been considerable work in the field of cartilage mechanics. The transient deformation behaviour of loaded cartilage has been examined using several different experimental approaches, and complex models have been developed to accurately describe this behaviour.

The microstructural response of AC to load is less well understood, however. The aim of this work was to investigate the anisotropy and heterogeneity of cartilage and its effect on the load bearing characteristics. Firstly, existing experimental data were used to create a layered finite element model of cartilage under load. Using this model, three sets of material parameters were evaluated for their suitability in reproducing experimentally observed strains, as well as minimising peak stresses. It was found that only by including the heterogeneity associated with collagen fibre orientation could the layer boundary deformations be exactly modelled, whilst preventing potentially damaging interfacial shear.

Tensile testing of cartilage from the equine metacarpophalangeal joint, using samples obtained from each individual layer, was performed to validate findings from the model as well as to determine the variation in mechanical properties in regions of different weight bearing characteristics. It was found that the tensile stiffnesses varied with depth as predicted by the model, demonstrating an average value of 31.3 MPa at the surface and 9.4 MPa in the radial zone, although there was considerable variation. Polarised light microscopy was used to determine the preferential collagen orientation, as well as qualitatively assess the angular spread and other patterns in collagen organisation. It was found that the appearance of the collagen network varied both with depth and location on the joint, with high weight bearing regions showing more isotropic fibre distributions below the surface than low weight bearing regions.

To directly probe the microstructural response of AC to load, the tensile loading rig

was modified to allow simultaneous imaging of the sample using two photon fluorescence microscopy. This allowed the relative displacement of cells and elastin fibres, which are intrinsically fluorescent, to be observed at increasing levels of strain. From locations and orientations of these features, the strain field could be calculated at two length scales: in the vicinity of specific elastin fibres (microns) and intercellular strains averaged over whole stacks (hundreds of microns). The strains at the two different scales did not correlate, suggesting that the microscopic strain environment varies considerably. The elastin fibre network was also investigated, and it was found that fibres appear to interconnect both at pericellular matrices, as well as at 'nodes' in the extracellular matrix.

Acknowledgements

I would first like to thank Peter Winlove, my primary supervisor, for his help and encouragement over the past 4 years. Peter allowed me to take control and steer this project wherever my interest took it, and always made himself available for discussion, which often took place every day of the week.

I would also like to thank my two secondary supervisors, Chris Smith and Hamid Dehghani, for their input with respect to mechanics, FE and data analysis.

I am also indebted to all my colleagues for their advice and assistance, especially towards the start of my project. Specifically I would like to thank Kenton Arkill for the early discussions about cartilage and dissection, John Hale for his expert programming and image analysis advice, Julian Moger for his assistance with the multiphoton microscope, Ellen Green and Dick Ellis for technical advice in the lab, Jessica Mansfield for help with both the multiphoton and polarised light microscopes, as well as design of the stretching rig, and Dave Colridge for all manner of other technical help.

Lastly I would like to thank all my friends and family for their support, especially at the end of the project.

Contents

List of Figures

List of Tables

Nomenclature

AC	Articular cartilage
AFM	Atomic force microscopy
BC	Boundary condition
CARS	Coherent anti-stokes Raman scattering
ECM	Extracellular matrix
FCD	Fixed charge density
FEM	Finite element method / model
FTIR	Fourier transform infrared microscopy
GAG	Glycosaminoglycan
ISF	Interstitial fluid
MCP	Metacarpophalangeal (joint)
MRI	Magnetic resonance imaging
OA	Osteoarthritis
PCM	Pericellular matrix
PG	Proteoglycan
R	Radial (layer of articular cartilage)
RA	Rheumatoid arthritis
SAXS	Small angle X-ray scattering
SEM	Scanning electron microscopy
SHG	Second harmonic generation

Ta	Tangential (layer of articular cartilage)
TEM	Transmission electron microscopy
TPE	Two photon excitation
TPF	Two photon fluorescence
Tr	Transitional (layer of articular cartilage)

Chapter 1

Introduction and Background

This thesis concerns the structure and function of articular cartilage at a microscopic level. Work involving numerical modeling, mechanical testing and nonlinear microscopy of cartilage has been performed, and is documented in the results chapters (3-5). This chapter aims to provide a comprehensive summary of the literature on cartilage composition, anatomy, mechanics and imaging techniques.

This chapter begins by introducing articular cartilage and its role as a soft tissue in the human body. The main constituents of articular cartilage are defined and their role discussed. The anatomy of the equine metacarpophalangeal joint is then discussed, as it is the source of cartilage samples used in all the experiments in this thesis. The following section goes into detail about mechanics and is split into two sections. The first section describes the various different mechanical experiments that can be performed on articular cartilage, and their relevance to cartilage physiology. The second section deals with the mathematical models that have been used to describe the mechanical response of articular cartilage to load. The third section briefly describes the finite element method for solving a mechanical loading problem. The final section summarises the various techniques that have been used to image cartilage. Details are included about two photon fluorescence, a nonlinear imaging modality used in Chapter 5 for imaging cells and elastin.

1.1 Cartilage Structure and Function

1.1.1 Overview

Cartilage is a soft connective tissue present within many parts of the human body. The primary functions of cartilage usually include absorbing impact and preventing bone-to-bone contact. A more detailed discussion about the functions of various types of cartilage

is included in the next subsection. Cartilage is avascular, aneural and alymphatic due to the forces and wear it sustains, and is therefore slow and ill-equipped to repair from injury and damage. Articular cartilage (AC) is specific to synovial joints in which it has the additional function of providing a low friction surface. Arthritis is a group of conditions affecting synovial joints of which there are two main diseases: osteoarthritis (OA) and rheumatoid arthritis (RA). RA is a painful autoimmune disease which can cause joints to swell and become deformed. OA is a degenerative disease which results in the wear and failure of AC, and affects approximately 80 % of people over the age of 65 and essentially everyone over the age of 80 in the USA [1]. Clearly, there is a great need to continue developing treatments for OA, and to do so we must thoroughly understand both the contributing factors to the development of OA, as well as the material on which it has such a detrimental effect [2].

Cartilage is a porous material with 4 major components:

- A collagen fibre network
- Proteoglycan (PG) molecules
- Chondrocytes
- Interstitial fluid

The first two components are referred to as the extracellular matrix (ECM), which has the primary role of endowing tissues with specific mechanical and physicochemical properties, as well as to provide a framework for chondrocyte (cell) support and migration [3]. The interstitial fluid is water which contains dissolved electrolytes. PGs can be described as solid or fluid depending upon the timescale in question. Over short timescales ($t \sim$ minutes) PGs act as a porous solid matrix through which interstitial fluid can flow. Over longer timescales the PGs act as a viscoelastic gel which can flow around the collagen fibre network.

1.1.1.1 Cartilage Types

There are three main types of cartilage. Hyaline cartilage is the most common and is the type to be considered in this project. Other types of cartilage include elastic cartilage and fibrocartilage. Elastic cartilage contains elastin fibres in much higher density than the other types. Its role is to provide support, yet allow a relatively large range of movement without incurring damage. Examples of elastic cartilage can be found in the earlobe and epiglottis.

Fibrocartilage contains predominantly collagen fibres, with significantly smaller proportions of PG and interstitial fluid. It is the only cartilage type to contain type I collagen.

As such, fibrocartilage is very tough and is well-suited to its job of providing support and absorbing shocks in areas such as in the human spine (as intervertebral disc) and knee (as meniscus).

Hyaline cartilage contains closely packed type II collagen fibres but not to the same degree as fibrocartilage. It is tough, yet somewhat flexible. Hyaline cartilages are generally surrounded by dense, fibrous periochondria [4] which provide mechanical support, as well as connections to other connective tissues. Hyaline cartilage can be found in areas such as between the ribs and sternum, the nose, and covering the articulating surfaces of joints where it is referred to as *articular cartilage*.

1.1.1.2 Function and Physical Properties

Cartilage exhibits very heterogeneous characteristics [5]. It is known that cartilage is an inhomogeneous, fibrous material with collagen fibre orientation varying with both depth [6] and load [7]. PG concentration and composition varies with depth, and the glycosaminoglycan (GAG) side chain types vary in abundance [8]. The fixed charge density associated with PGs (see Section 1.1.2.2) varies with depth, ranging from a value of approximately $8000\,\mathrm{mEq\,kg^{-1}}$ at the articular surface to $13000\,\mathrm{mEq\,kg^{-1}}$ in the deep zone. The volume fraction of interstitial fluid varies with depth with values varying from 85 % at the surface to 70 % in the deep zone [9]. Chondrocytes vary in shape between the layers, appearing as discs with short axis aligned radially at the surface, appearing mostly spherical at depths of $50\,\mu$m to $100\,\mu$m, and appearing stretched in the radial direction below.

Between the articular cartilage and subchondral bone is a layer of calcified cartilage. This region is generally much stiffer than the overlying cartilage [5], but significantly less stiff than the underlying bone [10]. The boundary between the calcified cartilage and the AC is referred to as the tidemark, which tends to advance and duplicate in disease such as OA. The boundary between the calcified cartilage and subchondral bone is referred to as the cement line, and it generally follows a bumpy, irregular path resulting in the thickness of the calcified cartilage varying considerably across the joint. It has been shown histologically that in some places the AC meets the subchondral bone and even the marrow spaces without passing through any calcified cartilage at all [11].

Such heterogeneities within the cartilage structure are likely to have a significant effect on the mechanical properties. It has been shown using simple unconfined compression tests that cartilage does not strain equally in the two Cartesian axes perpendicular to the direction of load [12]. The two axes along which the lateral strain was measured were chosen to be parallel and perpendicular to the *split line*. The split line is the direction

in which cartilage would split should it be pricked with a hemispherically ended pin. It is generally accepted that the split line has some correlation with surface collagen orientation within the vicinity of the prick [13], however it is not reliable nor rigorous. This hypothesis is supported by the results in the work above where it is reported that the equilibrium strain parallel to the split line is approximately half the value perpendicular to the split line.

The AC in a synovial joint will experience different stresses and strains depending upon the location within the joint, the type of activity being undertaken, as well as the state of pathogenesis. Gaining an understanding of the propagation of stress through the AC at a *microscopic* level is the key to understanding the onset and development of OA, and is one of the main focuses of this work. Before one can start hypothesising about small-scale cartilage mechanics however, a detailed understanding of each of the components is needed.

1.1.2 Cartilage Constituents

1.1.2.1 Collagen

Collagen is one of the main structural components of biological tissue, providing mechanical integrity and strength to animal bodies [14]. Collagen is a hierarchical structure (Figure 1.1), which is characterised by its high tensile modulus and strength. At the molecular scale, the basic unit of collagen is the tropocollagen molecule which consists of three helical polypeptides (pitch 0.87 nm), which are arranged themselves in a right-handed super helix (pitch 8.7 nm). Tropocollagen molecules are approximately 300 nm long and 1.5 nm in diameter, and self-assmble into striated structures to form fibrils $20\,\text{nm} - 40\,\text{nm}$ in diameter. The tropocollagen molecules are staggered by a distance of approximately 68 nm, denoted D. Figure 1.1(B) illustrates how a section of a fibril of width D is periodic every 5 molecules, and contains a total length of collagen of 4.4D in each period. Bundles of fibrils form fibres which vary in diameter between $0.2\,\mu$m and $12\,\mu$m. It remains unclear how long individual collagen fibres are, and therefore whether fibres are continuous from the deep zone through to the surface.

There are more than 20 types of collagen [15, 16] with more being discovered each year. Collagen types (typically denoted by a Roman numeral) are determined by the amino acid sequence in the tropocollagen molecule. The most abundant collagen types in the human body are I, II, III and IV. Type II collagen is one of the primary constituents of healthy AC, occupying $60\,\% - 70\%$ of the dry weight [17]. Apart from small amounts of other collagens in the pericellular matrix (e.g. type V), other types of collagen are only found in AC under the effect of disease, such as types I and III [18] and type X [19].

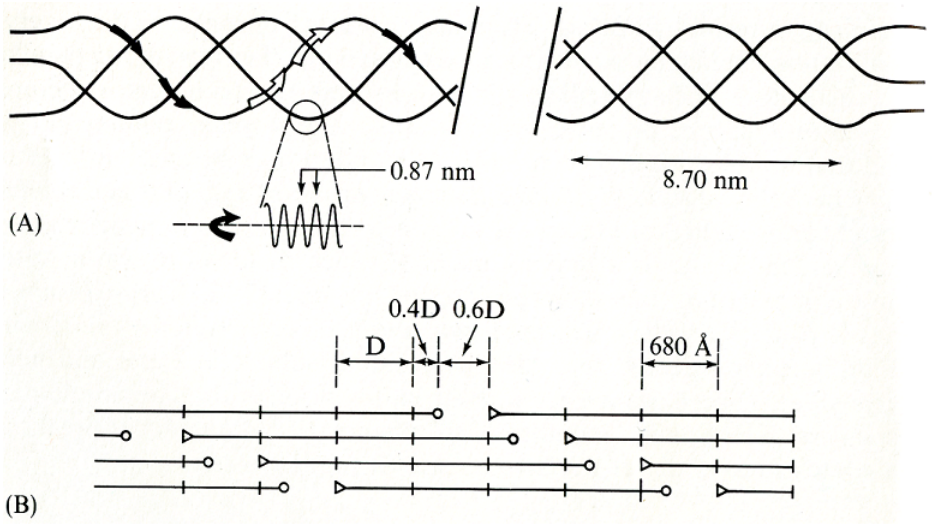

Figure 1.1: Collagen hierarchical structure detailing (A) the geometry of the tropocollagen molecule, and (B) the striated and staggered arrangement of tropocollagen molecules in a collagen fibril [14].

These pathogenic changes are attributed to cellular malfunction leading to synthesis of unusual alpha chains [20].

Collagen has a tensile modulus of around 50 MPa [21] and is responsible for the high tensile load support of tendons and ligaments. Collagen does not provide significant resistance to compressive stress due to its high slenderness ratio, however it provides indirect support in AC by balancing the osmotic swelling effect of the proteoglycans (explained in the next subsection). The collagen network in AC is highly anisotropic and therefore confers complex mechanical properties. A highly simplified diagram of the variation of collagen alignment with depth into cartilage can be found in Figure 1.2, illustrating the tangential orientation at the articular surface, passing through a gothic arch arrangement into radial alignment. This is referred to as the Benninghoff model [6]. The orientations of collagen fibres provide a means of describing cartilage in layers, with the naming convention Tangential, Transitional and Radial being used throughout this work. The collagen content also varies with depth, being most abundant at the surface and least abundant in the deep zone Muir et al. [22].

The Benninghoff model can be extended into 3D by describing collagen as a network of overlapping 'leaves' connected by small fibres [1]. This leaf structure has been visualized using scanning electron microscopy (SEM) [23, 24], which showed that collagen takes the form of relatively thick ($50 - 60\,\mu$m) fibres in the radial zone, fibrillating into a pseudo-randomly orientated network in the transitional zone before flattening into a tangential arrangement of thin lamellae between 1 and 3 fibrils thick near the surface. Fibrils in the surface lamellae appear to cross at varying angles suggesting there is not a strong prefer-

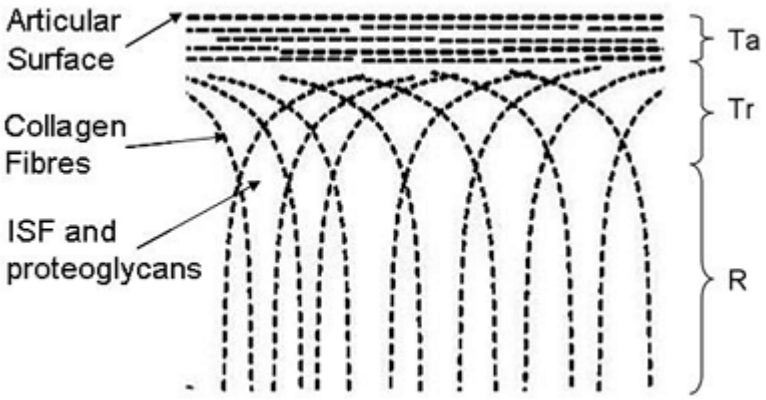

Figure 1.2: Schematic diagram illustrating the anisotropic alignment of collagen fibres in articular cartilage. Cartilaginous layers, labelled as tangential (Ta), transitional (Tr) and radial (R) are shown.

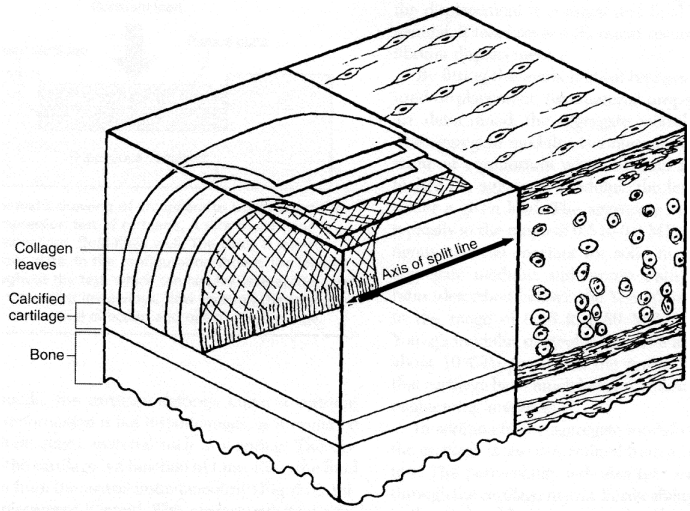

Figure 1.3: Collagen leaf structure in articular cartilage (adapted from [1]).

ential orientation in the tangential plane, however split line testing suggests a significant, repeatable trend [25, 13].

Split line testing involves puncturing a specimen multiple times with a flat or hemispherically ended awl. Specimens are usually then coated with a dye (typically Indian Ink) in order to observe the morphology of the puncture [25]. The punctures create elliptical holes, and the long axes of the ellipses are referred to as the *split line direction*. The discovery of split lines was first made by Hultkrantz [26]. The split line direction is generally regarded as being a good approximation of the preferential orientation of collagen at the surface, as shown by Kamalanathan and Broom [13], and is supported by work by authors such as Maroudas et al. [12] in which cartilage is shown to be significantly more compliant perpendicular to the split line than parallel to it. Split line testing is used to determine rough trends in collagen orientation in Section 4.2.

It is unlikely that the leaf structure of AC is as pronounced as SEM images have shown,

as the preparation process involves chemical treatment, dehydration and cryofracture which are each highly invasive and destructive. A less invasive method for measuring the orientation of collagen involves measurement of X-ray diffraction through cartilage samples [27, 7, 28]. The distribution of diffraction peaks relates directly to the orientation of collagen along the X-ray beam. These works support the Benninghoff model for collagen alignment, but also provide quantitative information for the spread of angles around the Benninghoff trend, as well as surface trends and deviations due to external loading and/or disease. Visible light microscopy has also been used (enhanced using phase contrast or polarization techniques) to either directly image collagen fibres [29, 30], or determine microscopic trends in orientation [31, 32] without the use of stains, but requiring thin histological sections to avoid scattering. Advances in nonlinear microscopy over the past decade, particularly second harmonic generation (SHG), have enabled stain-free images of collagen at the cellular scale to be acquired from samples without the requirement of thin histological sections [33]. This allows 3D reconstructions of the *in situ* cartilage structure to be obtained.

The reorientation of the collagen network under normal external load is complex due to the anisotropy of the ECM. It has been shown that under increasing load the first orientation change occurs at the surface where tangential fibres are compacted [28]. Even a tiny tare load of $\leq 15\,\mathrm{Pa}$ causes the Ta fibres to compact sufficiently to significantly restrict fluid flow through the articular surface [34]. At higher loads the Ta layer continues to compact to a fraction of its original thickness, the Tr region experiences strain approximately one quarter that of the Ta layer, and the radial fibres begin to lean. At very high (damaging) loads, the radial fibres lose tension and are observed to bend or crimp.

Although healthy articular collagen is always arranged in the Benninghoff architecture, there are still marked differences in the relative thickness of layers, the depth-dependent angular distribution of fibres and the volume fraction of collagen. Muir et al. [22] showed using electron microscopy and chemical analysis that the collagen density was significantly higher at the surface than at any other depth. The behaviour varied between samples but the general trend showed a minimum in collagen density in the deep zone before increasing slightly towards the tidemark. Moger et al. [7, 28] have shown that the relative thickness of cartilage layers may be location-specific, and hypothesise that this is due to the different loading conditions the AC is exposed to. Regions of high shear loading would require a larger shear modulus to prevent damage which may suggest more strongly orientated tangential zone, while regions of high normal loading may require the opposite. Despite the Benninghoff structure being widely accepted as macroscopically accurate, tangential fibres have been found in the mid zone [31].

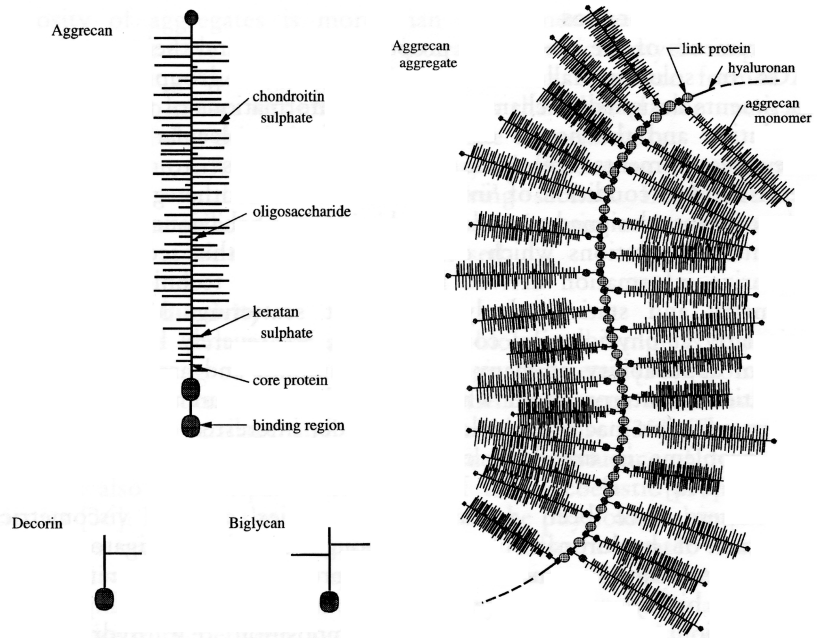

Figure 1.4: A schematic of the various forms proteoglycans take in articular cartilage, the most common of which is aggrecan (top left), which can aggregate into aggrecan aggregate (right). Not all proteoglycans are long chain molecules, the smallest, decorin, contains only one GAG side chain. [35]

1.1.2.2 Proteoglycan

Proteoglycans (PGs) are large molecules consisting of a protein core covalently bonded to one or more glycosaminoglycan (GAG) side chains. PGs form the major subclass of the glycoproteins which are referred to in older histology texts as the 'ground substance' of the ECM [35]. PGs are a major constituent of the ECM, comprising between 5 % and 15 % of the dry weight of AC [17] and are largely responsible for its compressive stiffness, as well as the flow behaviour of the interstitital fluid (ISF). PGs are unbranched monomers which aggregate with hyaluronan filaments into macromolecules up to 2×10^8 Da in weight, and 2 μm in length [36, 37] (Figure 1.4). Aggrecan is the most abundant PG and consists primarily of the GAGs chondroitin sulphate and keratan sulphate, which have been shown to vary in concentration with depth into the tissue [8].

GAGs are long, unbranched carbohydrates of repeating disaccharide units containing sulphate and carboxylate groups which dissociate in water at neutral pH. Proteoglycans therefore contain fixed negative charges surrounded by a cloud of mobile counter ions in the ISF, which give rise to the Donnan osmotic pressure [38] causing AC to imbibe water and swell. GAGs are so hydrophilic that their swollen state can be up to 1000 times greater in volume than their unhydrated state. This swelling behaviour is derived from two physical phenomena: [39]

- The electrostatic repulsion of fixed negative charges.
- Osmosis caused by the ratio of dissolved mobile electrolyte concentrations between the ISF and bathing solution.

The total swelling pressure is governed by the amount and type of GAG present within the tissue, as well as the electrolyte concentration and pH of the bathing solution. There has been extensive investigation of the swelling behaviour of GAGs involving osmometry [40] as well as mechanical testing of intact tissue explants [41, 42], proteoglycan-free explants [43] and hydrogels [44]. Although each investigation provides only an approximation of the Donnan osmotic pressure, there is considerable agreement across the literature as to the electromechanochemical behaviour of AC. Each investigation demonstrated an exponential decrease in the fluid pressure with increased NaCl concentration, falling by around 60 % when varied from physiological (0.15 M) to 1 M solutions. This is due to electrostatic shielding of the positively charged ions [45]. The same effect is observed when lowering the pH of the tissue, [42] which has the effect of lowering the fixed charge density (FCD) of the cartilage and thereby reducing electrostatic repulsion. This continues until pH 2.5, at which the cartilage reaches the isoelectric point and is charge neutral. At pH values below 2.5 the swelling increases again due to positive charge repulsion. The FCD of articular cartilage in the human femoral condyle *in vivo* at a depth of 0.5 mm is approximately 80 mequivkg^{-1} [5]. Physiological values for the osmotic pressure of articular cartilage generally fall in the range of between 0.35 MPa and 0.4 MPa [40, 46].

The swelling pressure and relative GAG abundance varies considerably with depth into AC. Lipshitz et al. [47] investigated the depth dependent swelling ratio by taking sections of cartilage from different depths and comparing their wet and dry weights. It was found that the swelling ratio was at its highest in the surface quarter, and dropped steadily to half the peak value at the deepest point. This correlates with measurements of water content made by Venn and Maroudas [48] who stated values of 74% at the surface and 67% in the deep zone. Bayliss et al. [8] used gel chromatography to determine the variation in GAG content with depth, and found that chondroitin sulphate was the most abundant with the highest amount found in the mid zone. Keratan sulphate was the only other GAG of significant quantity, and its quantity increased with depth into the tissue. Buckwalter and Rosenberg [49] performed electron microscopy on cartilage from varying depths and found that the keratan sulphate GAGs attach to the inner regions of aggrecan while the larger chondroitin sulphate GAGs attach to the peripheral regions. PGs have been documented to decrease in size with depth [8], providing a potential reason for the associated increase in the keratan sulphate:chondroitin sulphate ratio.

The electrochemical swelling of GAGs coupled with tension in the interlinked collagen fibre network provide cartilage with its inherent stiffness. The effect of swelling and

changes in GAG content on the mechanical properties of cartilage has been investigated [32, 50, 51] as well as the effect of changing the bathing solution [52]. An increase in GAG content correlates with an increase in the compressive stiffness of cartilage, while an increased concentration of salt in the bathing solution makes the sample more compliant. Investigations into the deformation behaviour of full thickness plugs of articular cartilage (e.g. [34]) have shown that the surface zone deforms much more readily than the other layers of AC and have attributed this behaviour to a smaller PG volume fraction.

Despite being the two major components of the ECM, it remains unclear how proteoglycans interact with collagen fibrils. Electron histochemistry [53] has shown ordered arrangements of PGs parallel to nearby collagen fibrils, as well as inside them. Most theoretical treatments of cartilage mechanics which include osmotic swelling effects assume that the swelling pressure is transfered directly to the collagen fibres which are held in tension. This can be explained qualitatively by assuming the collagen network acts as a cage or semi-permeable membrane around PG molecules, with pore gaps sufficiently small that the PGs are effectively trapped. This assumption has been justified in work focussed on the effect of large scale swelling in degenerate cartilage [2] whereby increased water content and volume of cartilage samples are accompanied by damage to the collagen fibre network. This has been confirmed using Nomarski light microscopy [30, 54, 29] which reveals striations and loss of interconnectivity of the collagen fibre network in degenerate cartilage. A loss of interconnectivity limits the ability of the collagen network to restrict osmotic swelling, and hence the cartilage increases in volume.

Another fundamental property of PGs is their low hydraulic permeability. When external load is applied to an AC sample, the equilibrium force balance between the osmotic swelling pressure and collagen tension is perturbed. The hydrostatic pressure becomes greater than the osmotic force and thus fluid is exuded. The rate of fluid exudation is dependent upon the pressure gradient and the permeability of the AC, which can vary considerably with depth, location on the joint, solid network strain and state of degeneration. A typical value for the hydraulic permeability of the surface of AC samples is $5.8 \times 10^{-16}\,\mathrm{m^4N^{-1}s^{-1}}$ [55, 56] with an average pore size of 60Å. Such small values can result in stress-relaxation timescales of several hours [57]. Stress bearing is shared between the solid and fluid phases of the AC and outside of equilibrium there is a transfer of stress from fluid to solid [58, 44, 59] until the load bearing is roughly equal. A higher FCD results in a higher peak stress after compression [59]. This low intrinsic permeability associated with PGs endows AC with the ability to absorb impacts as high as 28 MPa without failure, despite failing regularly at significantly smaller static loads of 15 MPa or less [60].

1.1.2.3 Elastin

Elastin is an elastic protein which is common in the ECM of mammals. It exhibits remarkable extensibility, being able to extend to strains of 70 % and still recover completely [5]. Elastin, like collagen, can form numerous different structures depending upon the mechanical environment of the tissue. Unlike collagen, however, the elastin base unit, tropoelastin, does not vary in its composition. The various arrangements of elastin include [61]:

- Solid, branching and unbranching, varying thickness fibres (ligaments)
- Concentric lamellae (blood vessels)
- 3-D networks of fine fibrils (elastic cartilage)

In some tissue, such as the skin and lungs, elastin occurs in more than one of the above forms. In general, elastin is found in tissues which undergo large strains where a rubber-like mechanical response is required.

The ability of elastin to recover completely from substantial strain is due to its chemical structure. Detailed descriptions of the structure and physicochemical properties of elastin can be found in [62, 63, 64], a brief description follows here. The work done when deforming a structure can be described in terms of the Helmholtz free energy ΔA, which is defined as:

$$\Delta A = \Delta E - T\Delta S \tag{1.1}$$

where ΔE is the change in internal energy, T is the temperature and ΔS is the change in entropy. Conventionally, energy elasticity (associated with deformations that contribute to the internal energy) arises from distortion of molecular bonds, and therefore only allows elastic recovery over a small range of strains. The ability of elastin to recover from significant strain is due to its deformation being almost entirely *entropic* over a large range of strains, i.e. the contribution to the free energy is associated primarily with a change in entropy. The molecular structure of elastin allows a large number of degrees of freedom in its relaxed form, which then reduce when a strain is applied (see Figure 1.5). The large range of strains over which elastin can recover is associated with sparse cross-linking between constituent molecules, which provides little constraint to the range of configurations available.

Elastin was first found in the surface layer of articular cartilage by Hesse [65] using SEM, who simultaneously discovered a network of oxytalan in the upper radial zone. The

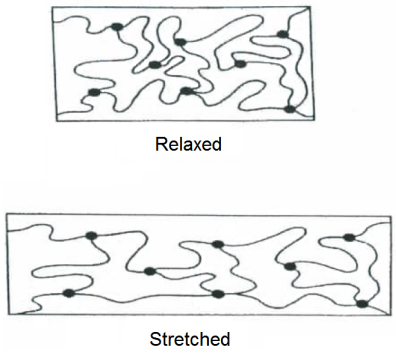

Figure 1.5: An entropic material in a relaxed and stretched state. As the sample is stretched, the freedom of the marked points to move is restricted, resulting in a decrease in entropy.

elastin fibres revealed two morphological components: a central homogenous, amorphous core surrounded by a ring of microfibrils 10 nm in diameter. The thickest fibres are approximately 1 μm in diameter [66]. Elastin was subsequently found in the pericellular matrix of some cells by Naumann et al. [67] using immunohistochemical techniques. The first case of fibrous elastin being imaged in a stain-free intact sample was performed by Yeh et al. [68] using two photon fluorescence, and the work of Mansfield et al. [66] went on to characterise its network structure and abundance.

The elastin network in the equine metacarpophalangeal joint (Section 1.1.3) consists predominantly of long, straight fibres which are occasionally branched. Arrangement of the fibres varies depending upon the location of the joint, showing a parallel arrangement around the cortical ridge and a more crossed arrangement either side. Fibres are generally limited to the superficial 50 μm of the AC and are particularly abundant in the uppermost 10 μm, however they have been observed as deep as 175 μm. The elastin in the pericellular matrix does not appear fibrous when imaged using TPF, although it is unclear whether it is completely amorphous or contains microfibrils below the limit of resolution [66].

1.1.2.4 Chondrocytes

Chondrocytes are the only types of cell found in cartilage and are responsible for producing and maintaining the ECM. Chondrocytes vary in size and morphology depending upon depth from the articular surface. The surface 3 μm-5 μm of AC is fibrous and contains no cells, although they are at their most abundant in the rest of the tangential region where they appear as flat discs in plane with the surface. In the transitional layer cells become more spherical and are arranged in a disordered manner, before becoming arranged in columns in the radial layer . The radial alignment of chondrocytes gives the appearance that parallel radial collagen fibres are arranged in bundles, however this may be due to

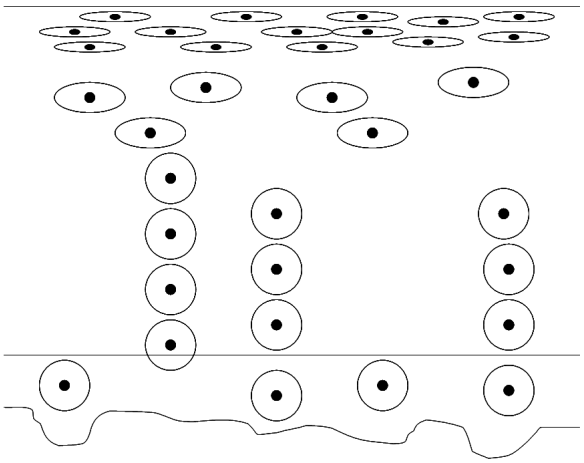

Figure 1.6: Variation in the morphology of chondrocytes through the depth of articular cartilage. The horizontal straight and irregular lines correspond to the tidemark and cement line, respectively.

artifacts associated with SEM [69]. Radial columns of chondrocytes are separated by distances of between 10 μm and 80 μm. Chondrocytes are 10 μm in diameter on average [5]. As cartilage is avascular, chondrocytes rely on mass transport via fluid flow for nutrition meaning the ability of cartilage to self-repair is both slow and limited.

The flow of fluid, and therefore the transport of nutrients, through cartilage occurs via both diffusion and external loading. The cellular metabolism therefore varies depending upon the amount and type of load bearing experienced by the cartilage. The pathway for nutrient transport in mature articular cartilage has been shown to be primarily via the synovial fluid, however in immature cartilage there is evidence for nutrient transport via the subchondral bone [70]. There has been extensive work linking chondrocyte biosynthesis with load application, reviewed by Grodzinsky et al. [71], which can be roughly generalized into two fields: variations in cartilage composition under abnormal loading conditions, and the behaviour of chondrocytes in gel cultures under varying loading conditions. The former involves either changing loading conditions in intact animal joints and performing histology after a given amount of time (e.g. [72]) or examining cartilage explants after prescribed loading with a rig. It is found that dynamic loading enhances biosynthesis [73] whereas static loading inhibits it [74]. The use of three-dimensional agarose gel cultures allow for more detailed analysis of the variation in biosynthesis associated with loading conditions [75, 76, 77]. It was shown by Buschmann et al. [76] that the existence of local matrix around a chondrocyte significantly affects its response to mechanical stimuli. Ng et al. [77] created an agarose culture which preserved the depth of the explanted chondrocytes, and found that the matrix synthesised by the cells matched that of the region from which the cells were originally taken, suggesting the technique may be feasible for regeneration of the anisotropic ECM of cartilage.

The local matrix surrounding the chondrocyte is referred to as the pericellular matrix (PCM), and it has a significantly different composition and set of mechanical properties to the rest of the ECM (sometimes referred to as the interterritorial matrix). The combined chondrocyte and PCM is referred to as a chondron. There is considerable research into the PCM as it regulates mechanotransduction (synthesis of matrix proteins caused by mechanical signalling pathways in the cell) and protects the cell hydrodynamically. For an extensive review of work related to chondrons in AC readers are directed to Poole [78]. The mechanical properties of cells and their PCMs have been measured using micropipette aspiration [79, 80] and it was found that the PCM behaves viscoelastically, with an equilibrium Young's modulus between that of the cell and the surrounding matrix (around 24 kPa). Finite element models of varying complexity have been created [81, 82] to find the distribution of stress and strain within the chondron, as well as investigate the effects of changes in mechanical properties associated with osteoarthritis. It was suggested by Alexopoulos et al. [82] that a possible role of the PCM was to provide a more uniform mechanical environment for the cell in a tissue as varied as AC.

1.1.3 The Equine Metacarpophalangeal Joint

The metacarpophalangeal joint, more commonly known as the fetlock joint in equids and other large animals, connects the third metacarpal/metatarsal with the proximal phalanx. It is a synovial ginglymus (hinge joint) which allows flexion and extension. It was selected as the joint to study in this thesis primarily due to the availability of samples from horses of all ages, and therefore with joints of different states of degeneration. Other advantages include its similarity with the human knee joint, the availability of samples of all ages from the local abattoir, and the lower risk of infection than that associated with handling human and bovine samples.

The load bearing nature of the metacarpophalangeal joint varies considerably depending upon the size, health and type of activity the horse is undertaking. Horses vary considerably in size and mass. Small ponies stand around 12 hands high or less (1 h = 102 mm, measured up to the base of the neck) and weigh under 300 kg, whereas shire horses can stand over 18 hands high and weigh over a tonne [83, 84]. Being a sesamoidal joint which undergoes a comparatively large amount of flexion, the articular cartilage of the metacarpophalangeal joint is exposed to a number of different stress conditions. These range from large normal loads caused by transmission of weight from the body of the horse to the hoof, to shear loads caused by the cartilage surfaces articulating across each other. The joint often suffers from disease such as osteoarthritis [85], particularly in athletic horses [86].

Figure 1.7: Cartilage surfaces of the equine metacarpophalangeal joint: Metacarpal (top left), sessamoids (top right), proximal phalanx (bottom).

1.1.3.1 Joint Anatomy

Despite sharing features with the human knee joint, the metacarpophalangeal joint is in fact the equivalent of the knuckle on a human hand. The joint connects the metacarpal (thoracic limb) or the metatarsal (pelvic limb) to the proximal phalanx. The metacarpophalangeal joints investigated in this work all originate from the equine thoracic limb. The joint includes two sesamoid bones (medial and lateral) on the posterior side of the joint, which articulate with the proximal phalanx over the articular surface of the metacarpal. Figure 1.7 shows the articular surfaces of the three boney components of the joint after dissection.

The bone structure of the lower thoracic limb is described in Figure 1.8. Veterinary terminology is different to that used casually by horse owners, so the casual naming convention in the figure is accompanied by the veterinary equivalent in the caption.

The bone structure of the lower leg in a standing position is predominantly straight, apart from at the metacarpophalangeal joint where the leg naturally bends ventrally. The resulting overhang leads to large torque about the joint, which necessitates the role of the *suspensory apparatus* and surrounding tendons [88]. The suspensory apparatus consists of the interosseus, proximal sesamoid bones and sesamoidean ligaments, (see Figure 1.9) and has the primary role of holding the sesamoid bones in a supporting position over the distal end of the metacarpal, whilst maintaining sufficient tension that the joint does not

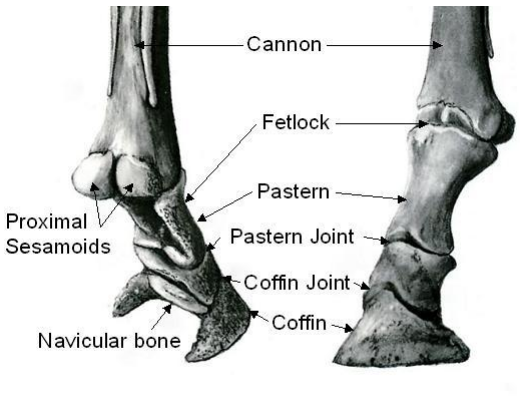

Figure 1.8: The bone structure of the lower equine thoracic limb viewed obliquely from the back (left) and front (right). Casual naming convention is used. Veterinary terminology: Cannon - Metacarpal; Fetlock - Metacarpophalangeal joint; Upper pastern - Proximal phalanx; Lower pastern - Middle phalanx; Coffin - Distal phalanx; Navicular bone - Distal sessamoid.[87].

hyperextend. The interosseus connects the proximal side of the sessamoids to the carpals. The sesamoid bones articulate over the palmar side of the metacarpal to reduce friction between the suspensory apparatus and the rest of the joint. The sesamoidean ligaments (short, cruciate, oblique and straight) connect the distal side of the sesamoids to the proximal and middle phalanges. As well as the suspensory apparatus, the superficial digital and deep flexor tendons also support the joint. These pass over the sesamoids and connect the radius to the proximal and middle phalanges, and the carpus to the distal phalanx, respectively.

1.1.3.2 Contact and Loading

The bone and ligament structure described previously distributes load across the articular surfaces in a complex manner that is not fully understood. In order to investigate the physiological loading of the joint, the various ways in which a horse moves and loads its legs must be understood. There are four gaits a horse uses when walking or running, each of which are dependent upon speed. These are walking, trotting, cantering and galloping [89]. The trotting gait is shown in Figure 1.10 as an illustration.

Walking is a four-beat gait and involves the movement of a single leg at a time while the other three remain on the ground.

Trotting is a two beat action where diagonally opposing legs move simultaneously (see Figure 1.10). Trotting is also referred to as jogging, as there is a period of suspension where all the legs are momentarily off the ground.

Cantering is a three beat action in which two diagonally opposing legs move in unison, while the other two move with phases before and after the coupled pair. This means that

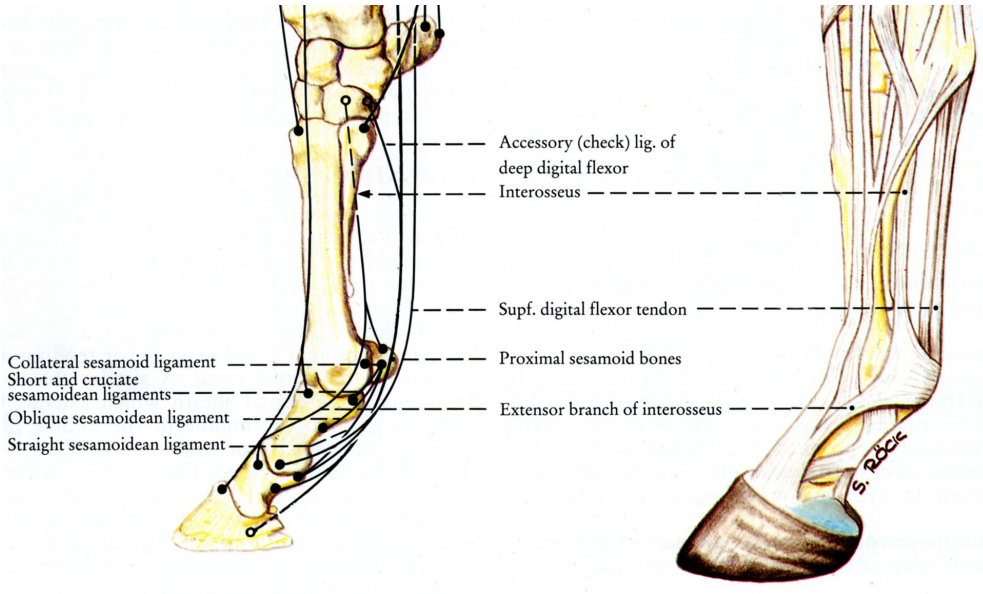

Figure 1.9: The musculature of the lower portion of the equine thoracic limb. [88].

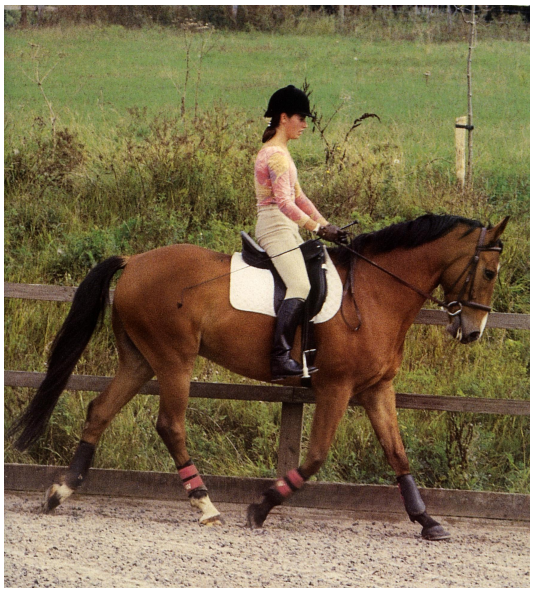

Figure 1.10: A horse trotting. [89].

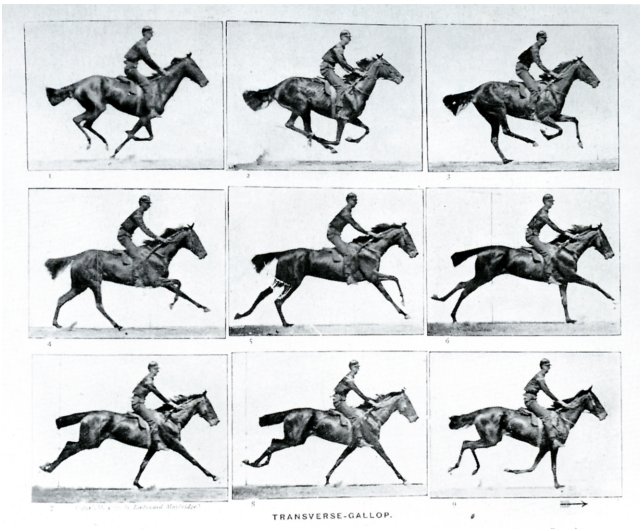

Figure 1.11: Early action photography of a horse galloping taken by Edweard Muybridge. [90].

Gait	Applied load (N)	Contact area
Walk	1800	$63.2\% \pm 4.6$
Trot	3600	$71.5\% \pm 3.5$
Canter	5400	$75.5\% \pm 4.1$
Gallop	10500	$86.7\% \pm 3.2$
Jump	12000	$95.0\% \pm 0.9$

Table 1.1: Loads and contact areas of the proximal phalanx in the equine metacarpophalangeal joint under simulated physiological loading conditions. Values taken from [91]

there is a period of time in each cycle where a single leg is supporting the weight of the horse.

Galloping is the fastest gait and a four beat action which is similar to the canter. The canter leads into a gallop by introducing a slight phase difference in the coupled movement, as well as accentuating all the movements and extending the suspension time. Until the 1860s there was debate as to whether there was a moment during a horse's gait when all four legs left the floor. Edweard Muybridge proved this was the case with one of the earliest examples of action photography [90]. Figure 1.11 is a copy of part of his original work, and shows a horse at progressive time intervals in the act of galloping.

Brama et al. [91] investigated the distribution and magnitude of load in the metacarpophalangeal joints under conditions simulating the four gaits. The experiment involved the static loading of transected legs in a position mimicking the weightbearing attitude close to the midstance phase. The assumed loads and calculated contact areas are shown in Table 1.1. These values are based on a mean body mass of 600 kg and correspond to 30 %, 60 %, 90 %, 170 % and 200 % of the total bodyweight, respectively. The results

show that the regions of highest load are the middle of the saggital groove and the dorsal side of medial plateu midway between the saggital groove and the medial edge of the joint. This provides insight into the normal load support of the articular surface of the proximal phalanx, however it is questionable whether the use of static loads (with durations of over a minute) truly reflect the loading conditions of a joint which, physiologically, is loaded dynamically.

The equine metacarpophalangeal joint is highly complex, and the cartilage inside the joint will experience a range of normal and shear forces *in vivo*. As weight is borne down on a leg, the cartilage experiences a normal force and the joint articulates. This articulation is resisted by the suspensory apparatus which acts as an extra shock absorber in parallel with the cartilage. As weight is further transfered to the leg in question, the increased force coupled with articulation of the joint leads to a shear force between the articulating surfaces of the joint. It is therefore assumed that the regions on the metacarpal that experience the largest shear loads are the regions which are in contact with the other articulating surfaces when the joint is fully flexed. It has been shown [92] that samples of AC from regions of high normal load bearing have significantly different mechanical characteristics to other regions, so an understanding of the *in vivo* loading characteristics is vitally important to understand the mechanical requirements, and functional variation of cartilage.

1.1.4 Cartilage Disease

Cartilage is prone to disease and, although it is not an inevitable consequence of aging, it is the elderly who suffer from it most. In the USA approximately 80% of people over the age of 65, and almost everyone over the age of 80 suffer from a form of joint disease [1]. The two main types of joint disease are rheumatoid arthritis and osteoarthritis.

Rheumatoid arthritis is a systematic autoimmune disease that affects all synovial tissue. Although much rarer than osteoarthritis, its symptoms can be considerably more severe, including considerable inflammation of the synovial membrane and joint capsule, ankylosis (stiffening and seizing of joints), bone and cartilage loss, joint disfigurement and pain. Rheumatoid arthritis is an area of ongoing research, but as its pathogenesis is related to the immune system and not primarily mechanical and compositional variations in cartilage, it is not covered in this work.

Osteoarthritis (OA) is the gradual degradation of articular cartilage, causing sub-optimal conditions for joint articulation and load support. Despite cartilage being aneural, osteoarthritis can cause significant pain, the origins of which are not completely understood but are likely to be related to swelling of the surrounding tissue and abnormal force

	Grade		Grade
I. Structure		III. Safranin-O staining	
a. Normal	0	a. Normal	0
b. Surface irregularities	1	b. Slight reduction	1
c. Pannus and surface irregularities	2	c. Moderate reduction	2
d. Clefts to transitional zone	3	d. Severe reduction	3
e, Clefts to radial zone	4	e. No dye noted	4
f. Clefts to calcified zone	5		
g. Complete disorganization	6		
II. Cells			
a. Normal	0		
b. Diffuse hypercellularity	1	IV. Tidemark integrity	
c. Cloning	2	a. Intact	0
d. Hypocellularity	3	b. Crossed by blood vessels	1

Table 1.2: Mankin scale. Score is calculated by adding together the rank in each company.

transmission through the joint.

The effects of OA on articular cartilage are many. The most apparent physical effect upon initial inspection of pathologic AC is fibrillation of the surface, and in severe cases the complete absence of cartilage from regions of the joint. OA does not always exhibit surface characteristics however, as Broom and Flachsmann [54] discovered when examining samples in the early stages of osteoarthritis. Despite this, many experiments investigating effects of OA involve a preliminary investigation of the articular surface. Such investigations can be made semi-quantitative by assigning a sample grade based on the severity of deviation from the healthy state, for instance using the Outerbridge scale [93, 29]. A more thorough and quantitative analysis is the Mankin scale [94], which involves grading a sample based on histochemical observations of the surface structure, cells, Safranin-O staining and tidemark integrity, see Table 1.2. The Mankin scale has been criticized, however, for not reliably measuring the ability of a joint to function normally [57].

Imaging and/or mechanical testing experiments are performed to assess the health of a sample of cartilage, and Boos et al. [19] suggest that a clear and reliable early sign of OA is the clustering of chondrocytes. The clustering of chondrocytes is indicative of a change in *phenotype* which is accompanied by a change in apoptotic behaviour [95] and synthesis of collagen types not native to healthy AC [18, 19]. Distributions of foreign collagen types in OA vary depending upon severity, with most of the new collagen restricted to the pericellular matrices of clustered or enlarged cells. Collagen types I and III are generally found in the superficial zone [18], and type X is predominantly synthesised in the middle and deep zones[19]. Although the quantities of the different collagen types synthesised are small as compared to the amount of native collagen (a maximum of 20 % [19] as opposed to 70 %), their presence may still have a significant effect, particularly

on mechanochemical signal transduction in chondrocytes. The presence of different collagen types in the pericellular matrix potentially explains the change in the associated viscoelastic properties reported by Guilak et al. [79]. Such changes in the mechanical environment of the cell will change its synthetic behaviour [96], which will in turn further deviate the cartilage from its healthy state.

As well as affecting collagen and cell phenotypes, OA also has a considerable impact on the mechanical characteristics of cartilage generally. The largest differences are observed in the water content, permeability and aggregate modulus (explained later) [57]. Each of these changes correlate, suggesting they have the same root cause. It was reported by Armstrong and Mow [57] that water content varies between 72 % and 89 %, permeability varies between $0.5 \times 10^{-14}\,\mathrm{Nsm}^{-4}$ and $10 \times 10^{-14}\,\mathrm{Nsm}^{-4}$ and equilibrium aggregate modulus varies between 0.3 MPa and 1.7 MPa. These are enormous changes and will have large effects on the deformation behaviour of the cartilage under load [97], and therefore the ability of the joint to support weight [1]. Despite these large variations in AC at different stages of disease, the use of mechanical stiffness and/or the thickness of samples is not recommended as an indicator of the health of AC, as experiments [54] have shown poor correlation. This is due to the large variation in the stiffness and thickness of AC across the joint surface.

Possibly the largest contributing factor to these changes is the breakdown of the native collagen network. Chen and Broom [30] reported images of striations in the radial layer of osteoarthrotic cartilage using Nomarski light microscopy. When imaged using transmission electron microscopy (TEM), it was clear that collagen fibrils were less interlinked than healthy cartilage, and will thus provide less support for osmotic swelling. When samples of osteoarthrotic cartilage were placed in baths of distilled water, they swelled to many times the size of equivalent healthy samples, despite stating decreased GAG content.

It is still debated whether the pathogenesis of OA is linked to genetics or physical wear. Idiopathic OA has been observed to occur in familial clusters, suggesting a genetic component. Holderbaum et al. [98] discuss the constituents of cartilage susceptible to genetic influence and the mutations which can lead to OA. There has been considerable work investigating the effect of load on matrix synthesis and the onset of OA. Complete deweighting of joints [99] increases the rate of tidemark advancement into the cartilage, a process that usually occurs slowly with age. Likewise, reducing the amount of dynamic loading limits the flow of fluid and therefore the flow of nutrients to cells [100, 70]. Grodzinsky et al. [101] investigated the effects of different loading types on the synthetic behaviour of cartilage and found that no loading or prolonged static loading reduces the rates of biosynthesis, whereas dynamic loading led to an increase.

In summary it would appear that in order to minimise the onset of OA a balance is needed in the amount of load applied to joints. Extreme cases such as overloading and unloading accelerate the onset of OA. Seedholm et al. [102] verified this result by relating the lifestyles and conditioning of individuals to the degree of OA in their knees. It was found that lesions occurred at flexions of 40° to 80° which corresponded to regions that were not regularly loaded. It was concluded that during day-to-day activity the loaded AC conditions itself to support load, and that damage is sustained when high stresses are applied to regions which have not been conditioned.

1.2 Mechanics

When cartilage is in a state of equilibrium, the internal stresses balance each other. These internal stresses are the Donnan osmotic swelling pressure associated with the proteoglycans, and the tensile stress in the collagen network. If a sample of cartilage is loaded, its internal stress distribution is perturbed from equilibrium. The force balance can then be expressed as:

$$L = T + \Pi \tag{1.2}$$

where L is the applied load, T is the tension in the collagen fibre network, and Π is the Donnan osmotic swelling pressure. This relation has been experimentally verified by Maroudas et al. [12] whereby cartilage was loaded and the osmotic pressure measured. The osmotic pressure remained constant until a critical load, above which it increased. Up to this point, the applied load was being balanced by a drop in the collagen tension, see Figure 1.12.

It has been discussed in the previous section that cartilage is a highly heterogeneous, anisotropic material, with orientation and quantity of each of its constituents varying with depth and location across the articular surface. It follows then, that a number of different mechanical testing experiments need to be defined in order to characterise the deformation and load support behaviour of AC. The theoretical treatment of cartilage mechanics has been considered from different perspectives, with the current most comprehensive transient models being the fibril reinforced poroviscoelastic model, and the tri-/quadriphasic models.

1.2.1 Experimental Mechanical Testing

The following subsection summarises and provides examples of the five main types of loading experiment. Each experiment probes different combinations of mechanical properties

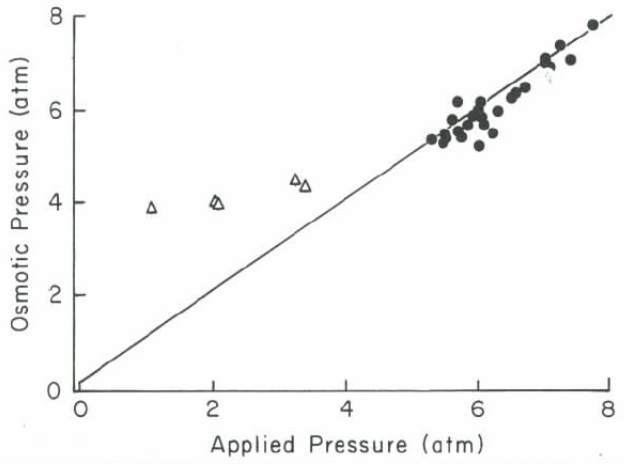

Figure 1.12: Comparison between applied and PG osmotic pressure at equilibrium, from compression tests performed by Maroudas et al. [12]. Triangular data points correspond to applied pressure values below the Donnan osmotic pressure, and round data points correspond to values above. .

of AC.

1.2.1.1 Confined Compression

A confined compression experiment involves excising a cylindrical plug of cartilage with a portion of the underlying bone from the joint in question and placing it in a confined, impermeable compartment where it fits snugly (Figure 1.13) . Samples are then loaded normally using a porous platen with cross sectional area equal to that of the sample. Stress and deformation data are taken using relevant transducers in the loading apparatus. As the load is applied in one direction, this loading method is often referred to as uniaxial confined compression. Ideally, there will be no friction between the sample and the compartment, and no exudation of fluid along the radial boundary, meaning that the deformation and fluid flow can be treated as one-dimensional variables. The dependent variables dictating the deformation of a sample in confined compression are the *aggregate modulus* (the resistance of the material to uniaxial volumetric strain), the permeability and the fluid content. Each of these values are strain dependent [103]. In practise, the porous platen does not provide a perfectly free draining boundary for exudation of interstitial fluid, and samples do not fit perfectly into the confining chamber. To overcome this problem, a small tare load is usually applied prior to carrying out an experiment [104].

Armstrong and Mow [57] performed confined compression experiments to obtain data for the equilibrium aggregate modulus and permeability of cartilage and its variation with disease. Sample degeneration was assessed using the Mankin scale (Table 1.2). It was found that sample degeneration correlated strongly with an increased water content

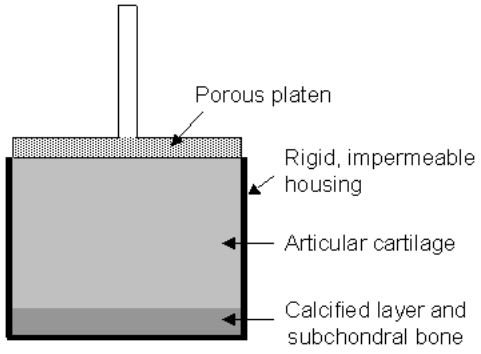

Figure 1.13: Schematic of a confined compression experiment.

and permeability and decreased aggregate modulus. This behaviour is summarised by Maroudas [2] as being due to collagen breakdown, and is explained in more detail in Section 1.1.4. Confined compression experiments were also used in investigating the electromechanochemical properties of AC [41]. In this work, bovine AC samples were compressed in baths of varying concentration NaCl solutions, and it was found that the average aggregate modulus varied from 1.1 MPa at 0.005 M NaCl to 0.27 MPa at 1.0 M NaCl. In this paper an effect referred to as the *chemical stress* is introduced which defines the force needed to prevent a material from osmotically expanding when placed in a lower molarity bathing solution.

Direct fluid transport measurements were made by Torzilli et al. [34] by incorporating a radiotracer (tritiated water) into the interstitial fluid of a sample. It was found that diffusion of ISF when the sample was unloaded was faster than convection caused by loading up to maximum physiological loads. Another highly significant result obtained using this technique was the rate of fluid exudation and recovery of samples under varying load. Even a tiny tare load of ~ 25 kPa restricted fluid imbibition following a compression experiment to less than half of that completely unloaded. This suggests the surface layer of AC compacts at low normal stress, and this compaction considerably reduces its permeability. This result calls into question the accuracy of permeability data taken from other compression experiments. This point was investigated further by Gu et al. [105] by performing confined compression experiments on agarose gels of varying concentration and measuring the deformation dependent permeability using linear biphasic theory (Section 1.2.2.4), and it was found that the permeability drop was not as significant as that of the surface layer of AC.

The confined compression experiment can be extended to investigate the fluid pressurisation in loaded AC by including a pressure transducer inset into the base of the compression chamber [58, 106]. It is predicted by biphasic theory that the interstitial fluid initially supports the majority of an applied load, and this experiment verifies the theory experimentally. Soltz and Ateshian [58] examined the load support during stress relaxation and

creep experiments (see Section 1.2.2.2) and found that the pressure in the ISF supported more than 90 % of the total stress for durations as long as 725 ± 248 s and 404 ± 229 s, respectively. The fluid pressure tended towards zero as the samples reached equilibrium demonstrating a stress-transfer mechanism from the fluid phase to solid. Soltz and Ateshian [106] then investigated fluid pressure in dynamic loading and found that above a characteristic loading frequency of 0.00044 Hz the magnitude and phase of the fluid pressurization matched that of the applied stress. Below this frequency, there was a distinct phase shift of the displacement and fluid pressure from the applied load, suggesting that the material is behaving viscoelastically (see Section 1.2.2.2).

Measurement of depth dependent strains and therefore depth dependent material parameters are possible by combining confined compression experiments with an imaging technique. Schinagl et al. [107] and Chen et al. [108] performed confined compression experiments of cartilage samples whilst also measuring intercelullar strains via epifluorescent microscopy of labeled chondrocytes. The aggregate moduli measured in these experiments were found to vary considerably with depth. The aggregate modulus of AC from the patellofemoral groove in the bovine knee joint varied from 0.079 ± 0.039 MPa at the surface to 2.10 ± 2.69 MPa at the deepest layer measured [107]. The same measurements taken from AC in the human femoral head yielded aggregate moduli varying between 1.16 ± 0.020 MPa at the articular surface, to 7.75 ± 1.45 MPa in the deepest layer tested [108]. It was noted in the latter investigation that trends in the stiffness of the cartilage did not correlate with those of the FCD.

1.2.1.2 Unconfined Compression

An unconfined compression experiment is similar to the confined compression experiment, only the radial boundary of the cylindrical plug is unrestricted, allowing outward radial deformation, see Figure 1.14. This means the porous solid matrix no longer undergoes a volumetric strain, and at equilibrium, it is the Young's modulus of the solid phase of the sample which determines the deformation. Assuming isotropy, the relationship between the Young's modulus E, and the aggregate modulus H_A, is: [109]

$$H_A = \frac{1-\nu}{(1+\nu)(1-2\nu)}E \tag{1.3}$$

where ν is the Poisson's ratio. The freedom to expand provides information about the Poisson's ratio and how it varies about the circumference. Maroudas et al. [12] performed an unconfined compression experiment to determine the radial strain behaviour of samples parallel and perpendicular to the split line, and found the value in the perpendicular direction to be twice that in the parallel direction. This provided strong evidence for the

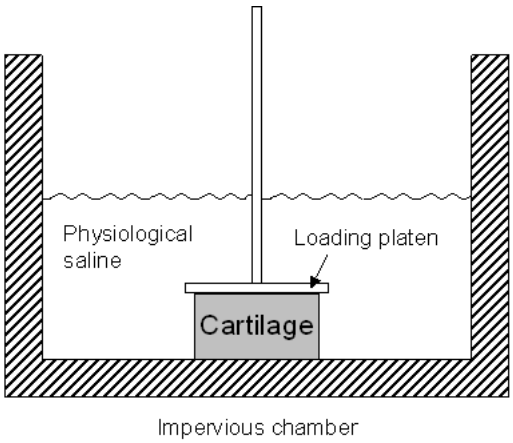

Figure 1.14: Schematic of a standard unconfined compression experiment. The loading platen can be porous, depending upon whether the rate of radial fluid efflux is being measured.

use of the split line test as a means of ascertaining preferential collagen fibre orientation at the articular surface. This effect has also been modelled using an anisotropic fibril-reinforced poroelastic model [110].

The unconfined compression test has been used to find the elastic material parameters of the solid phase of articular cartilage. Accurate values for the elasticity parameters of the solid phase of AC are needed to create accurate models for the deformation of cartilage under load. Jurvelin et al. [109, 111] used a combination of an unconfined compression test and optical microscopy to calculate the depth-averaged Poisson's ratio of AC from bovine shoulder joints. Two techniques were used for finding the Poisson's ratio: i. Direct measurement of lateral expansion through analysis of images taken perpendicular to the direction of loading, and ii. Indirect measurement by measuring equilibrium elastic moduli in confined and unconfined compression experiments, and extrapolating the Poisson's ratio using equation 1.3. It was found that AC from various regions of the canine knee joint had aggregate moduli varying from 1.113 ± 0.141 MPa to 2.084 ± 0.409 MPa and Poisson's ratios varying from 0.070 ± 0.016 to 0.236 ± 0.026. These values are in good agreement with those reviewed in the literature, i.e. $E = 0.41$-0.85 MPa and $\nu = 0.06$-0.18 MPa [112]. Wang et al. [113] took this technique further by performing multiple unconfined compression tests on cubic samples in different directions and varying the plane being imaged in order to determine the orthotropic elastic material parameters. This data is of considerable relevance to the work detailed in Chapter 3, specifically the calculation of the elastic D-matrix, Equation 3.1.1.

The electrochemical contribution to the mechanical stiffness of PGs and dissolved ions in the interstitial fluid has been discussed in Section 1.1.2.2. Sokoloff [114] performed unconfined compression creep tests of samples in several different bathing solutions and

investigated the surface deflection and recovery. The bathing solutions included distilled water, two different concentrations of NaCl, $N(CH_3)_4Cl$, monovalent, divalent and trivalent cations, anions and viscous solutions. The behaviour discussed earlier was observed, with some interesting extra observations. The divalent and trivalent cations caused large deformations under load, however while the deformations induced in the divalent solution were reversible when the sample was placed in physiological saline, those induced in the trivalent solution were not. Introduction of long chain molecules into monovalent and nonelectrolyte solutions to increase the viscosity had little effect on the deformation behaviour or recovery of the samples, suggesting the tissue selectively excludes long-chain polymers and effectively works as a rapid ultrafilter.

The fluid load support mechanism in confined compression discussed in the previous section becomes less clear when considering unconfined compression, as fluid can exude radially. Park et al. [115] investigated this by introducing a pressure transducer into the base of an unconfined compression chamber to measure the interstitial fluid pressurization. It was found that although peak fluid load support is not as great as in confined compression, it still corresponds to the majority of the applied load with values of $79\pm11\%$ and $69\pm15\%$ at the surface and deep zones of human femoral condylar articular cartilage, respectively, and $94\pm4\%$ and $71\pm8\%$ for bovine calf articular cartilage from the femoral surface of the knee joint. These results go some way towards explaining the deformation and damage caused by large dynamic and static loading performed by Flachsmann et al. [60]. In this investigation, AC samples from the the bovine patellar were loaded with a transparent indenter whilst simultaneously imaged for surface rupture. Samples were loaded statically (Figure 1.19) and dynamically. It was found that 60% of specimens tested statically at 15 MPa ruptured across the articular surface, with rupture generally in the split line direction. In contrast, however, no rupture was recorded under dynamic loading as high as 28 MPa. This suggests that the initially high fluid load support is important for preventing damage to the solid phase of AC.

There are many mechanical models which describe the mechanical behaviour of soft tissue, some of which are described in Section 1.2.2. In order to verify and improve such models, comparison with experiment is necessary. The unconfined compression experiment involves deformation and fluid flow in all three dimensions, and provides a good test for a mechanical model when combined with histology and imaging. Julkunen et al. [32] performed unconfined compression experiments on bovine knee and shoulder cartilage in order to obtain transient deformation data, as well as Poisson's ratios for the samples. The results from these experiments were compared with data from the fibril reinforced poroviscoelastic model, which in turn was based on data from fourier transform infrared and polarized light microscopy. It was concluded that the combination of imaging and

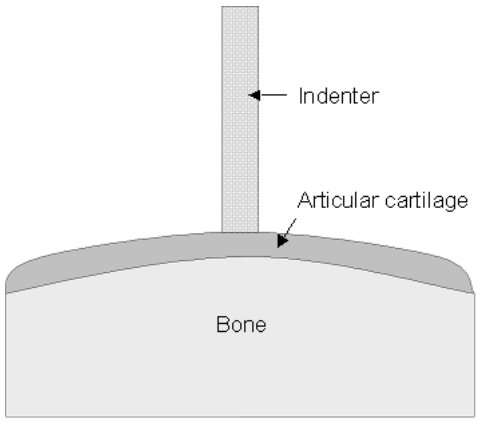

Figure 1.15: An indentation test.

FE modelling was sufficient to determine the mechanical behaviour of AC without requiring potentially damaging mechanical tests. Naili et al. [116] on the other hand used the opposite approach, defining a poroelastic mechanical model based upon the unconfined deformation behaviour of a sample. Equilibrium stress and strain data yielded Young's moduli and Poisson's ratios for three different materials, while hydromechanical tests and viscometry yielded the permeability of the materials and the viscosity of the imbibing fluid. With these parameters defined, it was shown that the poroelastic model recreates the transient force and pressure data to a reasonable degree of accuracy.

1.2.1.3 Indentation Testing

The indentation test is a less invasive method of determining the mechanical behaviour of a sample, as it does not require the excision or preparation of a sample. An indentation test involves pressing a cylindrical indenter with either a flat or hemispherical end against an intact specimen and recording the deflection and resistive force, see Figure 1.15. The cylindrical indenter is often porous to allow surface efflux and simplify the flow behaviour for modeling. The cartilage is kept hydrated by either repeated administration of physiological saline to the surface, or submersion of the whole sample. Although this is an attractive method from the perspective of being able to investigate small samples, as well as cartilage *in vivo*, it is very difficult to obtain accurate quantitative data due to the complex deformation behaviour of the cartilage in the vicinity of the indenter.

Indentation tests can be used to quickly compare the relative stiffnesses of different regions of a joint, assuming the cartilage thickness in each location is either the same, or larger than a specific value specific to the indenter. Garcia-Seco et al. [50] used indentation tests to determine the relative stiffnesses of cartilage in the equine femoropatellar, tarsocrural and metatarsophalangeal joints. A flat ended indenter 1.3 mm in diameter was used to perform a stress-relaxation experiment at a fixed deformation of 300 μm. The peak

stress was used as a relative measure of the cartilage stiffness, and it was found that the tarsocrural cartilage had the highest relative stiffness. A drawback of this technique is the lack of consideration of variable thickness. If the indenter diameter is roughly the same size as, or larger than the thickness of the sample then the cartilage will undergo significant compressive strain along the central axis throughout the entire depth, making the stress response thickness dependent. Toyras et al. [117] investigated the contribution of cartilage thickness to indentation stiffness by performing experiments using indenters of two different sizes, and measuring the thickness using high frequency ultrasound. Values for the instantaneous Young's modulus can be found using the formulation derived in [118] which states:

$$E = \frac{F(1-\nu^2)}{2a\omega\kappa} \tag{1.4}$$

where F is the applied force, ν is the Poisson's ratio, a is the indenter contact radius, ω is the indentation depth and κ is a scaling factor which depends in part on the sample thickness. It was concluded that although selection of a suitable indenter negates the thickness contribution, selection of such an indenter requires knowledge of sample thickness in itself. As cartilage thickness is easily found using ultrasound, it was recommended that any *in vivo* arthroscopic testing be accompanied by ultrasonic determination of cartilage thickness.

The ease of the indentation test makes it an attractive means of measuring changes in cartilage stiffness when the cartilage environment is perturbed. It has been shown [119] that the indentation test clearly demonstrates the effect of changing the ionic concentration of the bathing solution on the mechanical stiffness and can be quantified using Equation 1.4. More recently, the indentation test has been used [120] to show a lack of correlation between the mechanical stiffness of AC and the presence of dermatan sulfate, a GAG that has been visualised connected to collagen fibres. Indentation is also used for the assessment of degeneration of cartilage, Appleyard et al. [121] performed meniscectomies of ovine stifle joints and investigated the onset of OA 6 months later. Dynamic indentation testing using a non-porous cylindrical probe was used to find the dynamic stiffness and phase lag (see Section 1.2.2.2) of the cartilage as part of a larger analysis of the effect of the change in force transmission on the composition and physical properties of the AC.

Despite its ease of execution, the indentation test is significantly more difficult than other methods to analyse for equilibrium material parameters. Equation 1.4 can only be used for prescribed values of ν, which is itself an unknown after initial application of load. Mak et al. [122] proposed a method for finding the equilibrium aggregate modulus and

Poisson's ratio using a single indentation experiment. This method is based around the assumption that upon initial application of a load, the load is supported entirely by the shear modulus of the solid phase. When the stress and strain has reached equilibrium, the load is being supported solely by the solid phase, and thus there are two sets of data and two elastic unknowns which can be solved for. Biphasic theory (Section 1.2.2.4) is used to find the elastic parameters. This method was taken further by Lu et al. [51] by performing two indentation experiments of the same sample in bathing solutions of different ionic concentration. By assuming negligible contribution from the Donnan osmotic pressure at high ionic concentration, it was possible to calculate the FCD of the sample using triphasic theory. The results compared favourably with biochemical analysis.

The indentation test thus far has only yielded bulk mechanical parameters. AC is highly heterogeneous and anisotropic, so making these assumptions potentially ignores vital information about the mechanical behaviour. The indentation experiment was investigated by Julkunen et al. [56] using the fibril reinforced poroelastic model (see Section 1.2.2.3) to quantify the load supporting contributions of the fibrillar and non-fibrillar components of AC. It was found that the experimentally measured initial Young's modulus correlated with the fibril network modulus, and the equilibrium Young's modulus correlated with the nonfibrillar modulus. This suggests that the indentation test can provide information about the tensile stiffness of the collagen fibrils, as well as the compressive stiffness of the PG matrix. Lastly, simulated indentation tests can be used to investigate the material parameters which are otherwise impossible to measure. Li et al. [110] used an anisotropic fibril reinforced model to investigate anistropies in the permeability caused by collagen orientation. Simulated indentation tests demonstrated larger fluid pressures in directions perpendicular to the split line pattern than in any other direction.

1.2.1.4 Tensile Loading

The tensile test involves applying a stretching force to a sample as opposed to a compressive force, as is the case in the previous three tests. Homogeneous, isotropic materials behave similarly in compression as in tension, however cartilage exhibits very different mechanical behaviour due to its inhomogeneous composition. In compression, the swelling pressure associated with PGs provides the primary resistance to deformation, and the collagen fibres provide secondary resistance by limiting the degree of swelling. In tension the reverse is the case, with the collagen fibres primarily resisting extension by reorientating towards the direction of load and thus narrowing the sample, and the PGs providing secondary resistance by restricting the degree of reorientation and narrowing. The equilibrium tensile behaviour of a sample of AC is thus governed by the tensile stiffness of collagen, the connectivity of collagen fibres, and the osmotic swelling pressure.

The sample used in a standard tensile test can take two different shapes, a uniform strip (Figure 1.16a) or a dumbell (Figure 1.16b). The choice of sample geometry is influenced by the mechanical behaviour of interest. Investigations which include the failure behaviour of AC [123, 124, 125, 92, 126, 127] require the use of dumbell geometries to control the location at which failure occurs. The drawback of the dumbell geometry is the nonlinear distribution of stress, and therefore strain, across the length of the sample, preventing the accurate calculation of mechanical properties from stress-strain measurements. Instead, to determine the mechanical properties of a dumbell sample, an optical method is employed such as that used by Woo et al. [126, 127] in which displacements between marks on the thin section are measured using a microscope. If failure behaviour is not of interest then it is significantly easier and more accurate to calculate the mechanical properties using the strip sample and standard stress-strain measurements, as the tensile stress is uniform across the length (assuming no clamp anomalies). The geometries for tensile test of fibrous samples are defined by the American Society for Testing and Materials (ASTM) AST [128]. The minimum ratio of the length of the thin section of the dumbell, or the full length of the strip to the width of the sample is specified as 2:1, below this value plane stresses become dominant and the sample is not in the tensile regime. Recommended values are 5:1 or greater to ensure stresses propagate close to the direction of applied load.

Tensile tests have been frequently used to investigate the mechanical anisotropy in the tangential plane of articular cartilage. It is generally accepted that the split line (see Section 1.1.2.1) infers the preferential direction of collagen orientation, and this is supported by the work of Kempson et al. [124, 125] which involved performing tensile tests parallel and perpendicular to the split line direction, and found that at the surface there was a stiffness ratio of between 2:1 and 3:1 between the parallel and perpendicular data sets. The tensile experiments were performed at varying depth and it was found that the directionality of mechanical properties reduced with depth, supporting the view that collagen tension bears most of the tensile load. This view is further supported by work comparing the collagen content at the surface zone with the tensile modulus, which showed a significant positive correlation. More recent work by Sasazaki et al. [129] investigated the microstructural response of AC to tensile load using phase contrast microscopy, confocal laser scanning microscopy, SEM and TEM. It was found that collagen reorientates in the direction of applied load. The large degree of reorientation required when applying tensile forces perpendicular to the split line allowed samples to reach higher ultimate strains than parallel samples. It was revealed using SEM that upon application of load small ridges appear, and become accentuated at higher strains. It is believed due to the geometry of the ridges that these are collagen fibres protruding from the surface.

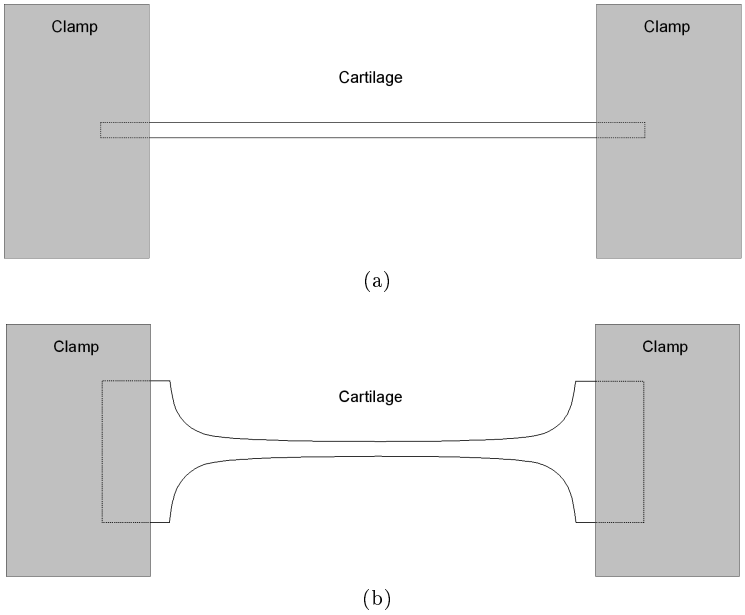

Figure 1.16: Schematics for uniaxial tensile tests. A pure tension test depicted in (a) results in an equal tensile stress throughout the length of the sample, thus allowing direct assessment of the material parameters using force-displacement readings from apparatus connected to the clamps. Dumbell shaped samples such as that depicted in (b) result in higher stresses, and therefore ultimate tensile failure at the mid point. This type of sample is used for assessment of the failure mechanisms of cartilage, but requires the use of markers and optical measurement to determine material parameters.

The mechanical response of AC to load has been shown to be linear up to strains of approximately 15% [92], however at strains above this, nonlinear effects become significant and Hooke's law (Equation 1.19) no longer applies. Fung [130] proposed an exponential stress-strain relationship of the form:

$$\sigma = A \exp(B\varepsilon - 1) \tag{1.5}$$

where A and B are material constants. This form was adopted by many subsequent authors. AC continues to extend without failure up to strains sometimes exceeding 100% [123, 126], however at the level of nonlinear strain there is also considerable width and depth contraction, making the ratio of applied force to tensile stress nonlinear as well. To account for this, Woo et al. [127] measured the lateral contraction as well as the tensile strain and adopted the Eulerian approach [130] to calculate the applied stress. This involves considering the deformed area as opposed to the initial area when converting from force to stress. This technique is valid and more accurate than the Lagrangian (standard) approach for homogeneous materials, although its accuracy for AC is debatable due to the surface fraction normal to load becoming more concentrated with parallel collagen fibres.

Several investigations have been made into the electrochemical influences on the tensile behaviour of cartilage. Kempson et al. [125] related the tensile stiffness with the GAG content, but found no correlation. Akizuki et al. [92] compared the tensile stiffness to the ratio of the collagen and proteoglycan content with a strong positive correlation. It was suggested that the quantity of collagen is not the main parameter in determining the tensile stiffness, rather the ratio of collagen to proteoglycan, suggesting that PG-collagen interactions responsible for the cohesion of the solid matrix are responsible for the tensile stiffness of AC. This has not yet been confirmed experimentally, and recent investigations into the effect of removal of decorin [120] (a protein speculated to contribute to adhesion between collagen fibrils) has shown no correlation with the tensile stiffness of AC. Investigations into the effect of bathing solution concentration, and thus the effect of FCD on the tensile stiffness [42, 92], clearly demonstrated the impact of swelling pressure on the tensile behaviour of AC. A chemically induced increase in the osmotic swelling of the PGs leads to an increase in tensile stiffness of the sample.

The effect of disease on the connectivity and arrangement of the collagen network discussed in Section 1.1.4 has a significant effect on the tensile properties of AC. Kempson et al. [125] compared the tensile stiffness of two age-matched AC samples, one healthy and one adjacent to an area of visibly degenerate AC. The values at the surface for the degenerate sample were significantly less (less than one fifth) than those of the normal sample. Values in the deeper zone varied less, again supporting the view that collagen supports tensile loads. This view is shared by Akizuki et al. [92], and enhanced by the findings that age by itself does not correlate with degenerate mechanical properties.

1.2.1.5 Tribology

The tribology of articular cartilage is the study of the effects of friction and lubrication between two adjacent articulating surfaces. Healthy synovial joints are very efficient pivots with exceptionally low friction coefficients, so potentially damaging shear associated with joint articulation is minimised. There has been considerable work in the field of articular cartilage tribology, which has been reviewed recently [131, 132]. The goal of tribological experiments is to measure the coefficient of friction between articular surface and another surface (either a man-made material or an opposing cartilage surface), often in the presence of lubrication. The tribological properties of a synovial joint are quite complicated, and it is likely that in normal physiological loading conditions there are a number of lubricating phenomena occuring simultaneously.

The first AC-specific tribological theory was proposed by McCutchen [133] entitled 'weeping lubrication', which introduced the concept of a 'weeping bearing'. The idea underpinning the theory is that cartilage exudes interstitial fluid when loaded, or 'weeps' thus

providing means of lubrication. In an article directly following this, Lewis and McCutchen [134] showed that this was the case by drying the surface of a piece of cartilage and pressing it against a glass slide, demonstrating the weep. In a subsequent article, McCutchen [55] measured the compressive stiffness, porosity, permeability and time-dependent frictional properties of AC and deduced that it was ideally suited as a weeping bearing as it exuded sufficient fluid under physiological load, but maintained fluid pressurisation sufficiently long that it does not lose its lubricating properties. In a later article, McCutchen [135] stated that the weeping lubrication mechanism requires that the load is supported in the most part by the fluid phase, and related this concept to the tension-compression nonlinearity of AC (explained in the previous section). The fact that cartilage is stiffer in tension means that the PG network supports only a small fraction of normal loads over short timescales, and therefore the fluid load support is high. A friction experiment analagous to those performed on AC was documented involving the use of a microporous polyhydroxylalkylacrylic ester resin which has similar mechanical properties in tension and compression, and it was shown that its coefficient of friction was higher than that of AC.

There are several different types of tribological experiments. Direct measurement of friction can be performed by pressing a sample of cartilage against a surface which either translates relative to the sample [136, 137, 138] or rotates [139, 140, 141]. The 'pin on disc' approach involves rotating a sample of AC and pressing a hemispherically ended pin against it [142]. Experiments have also been performed which involve articulating entire intact joints for the purpose of either measuring resistance of the whole joint to articulation [143], or to accelerate physiological wear [144]. High magnification imaging of the articular surface has been performed using atomic force microscopy (AFM) [141] as well as scanning electron microscopy (SEM) and environmental SEM [144].

There are several properties of synovial joints that minimise friction associated with articulation, the most important possibly being the natural joint lubricant, synovial fluid. Several of the aforementioned tribology experiments were performed with a variety of lubricants, and it was consistently found that synovial fluid acted as a much better lubricant than physiological saline, especially when the surface was smooth and free from anomalies [136]. The lubricating properties of synovial fluid are a topic of current research [139, 140]. The uppermost surface layer of cartilage has been referred to as the 'laminar splendens', and has been measured to be 800 nm-2 μm thick and resistant to treatment with hyaluronidase and chondroitinase ABC [141]. Environmental SEM has shown this surface layer to be extremely smooth in healthy AC [144], but when worn the collagen network becomes visible and the surface becomes rippled. It is likely that in this state the lubrication properties of synovial fluid are limited, leading to an increase in the rate

of wear of the joint.

1.2.2 Mechanical Modelling of Articular Cartilage

The complex mechanical response of AC to applied load has been extensively investigated using continuum models that make varying assumptions about the consistency of cartilage. The simplest model is the linear elastic model, which assumes cartilage to be a homogeneous Hookean material and does not consider the transient response to load. The viscoelastic model extends the elastic model by including transient effects that can be described in terms of configurations of springs and dashpots, whilst maintaining the assumption that cartilage is homogeneous. The poroelastic model assumes cartilage to consist of a porous solid matrix saturated by fluid, whereas biphasic theory treats cartilage as a binary mixture of solid and fluid. The ultimate goal of mechanical modeling is to add molecular level complexity to models, but that point is still far from being reached.

The focus of the work detailed in this thesis is the steady-state mechanics of AC. This is governed entirely by the solid phase of the cartilage and is thus completely described using elasticity. The findings of the work can be readily included in transient models, which are summarised in this section.

1.2.2.1 Linear Elasticity

Linear elasticity is the most basic continuum mechanical model. The hypothesis behind linear elasticity is that under the assumption of infinitessimal strain, there is a linear relationship between stress and strain.

Stresses are produced when a body is subjected to an external force. Stresses within a body are defined as a force per unit area. By defining a planar differential element ΔA with unit normal n_i normal to the direction of force, we can express the *stress vector* as:

$$\sigma_n = \lim_{\Delta A \to 0} \frac{\Delta F_n}{\Delta A} \tag{1.6}$$

likewise, a *shear stress* is defined by considering forces tangential to the plane:

$$\tau_n = \lim_{\Delta A \to 0} \frac{\Delta F_t}{\Delta A} \tag{1.7}$$

In a 3D Cartesian co-ordinate system it is convenient to consider planes with normals parallel with the x, y, and z axes. Each plane will experience normal stresses parallel to its normal vector, and two shear stresses parallel to the tangent directions of the plane. Thus the stress on each plane can be represented by *stress vectors*:

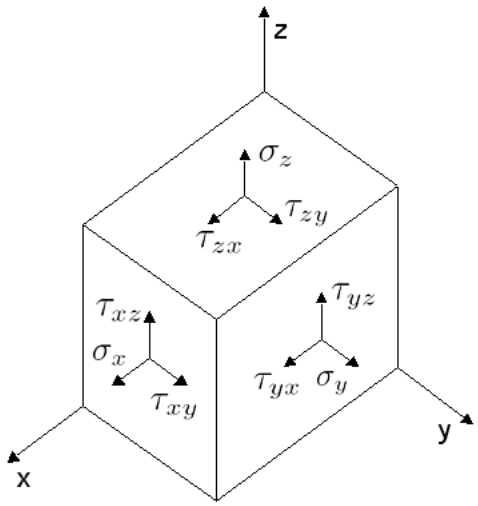

Figure 1.17: The 9 Cartesian stress components acting on a cuboid.

$$T_x = (\sigma_x, \tau_{xy}, \tau_{xz}) \tag{1.8}$$

$$T_y = (\tau_{yx}, \sigma_y, \tau_{yz}) \tag{1.9}$$

$$T_z = (\tau_{zx}, \tau_{zy}, \sigma_z) \tag{1.10}$$

The subscripts on the shear forces refer to the normal to the plane on which the shear is acting, followed by the direction of the shear. Normal forces commonly have only one subscript as the force acts in the same direction as the plane normal. Figure 1.17 shows each of the 9 individual stresses acting on a cuboid.

These three equations can be written in matrix notation to describe the *stress tensor*:

$$\sigma_{ij} = \begin{pmatrix} \sigma_x & \tau_{xy} & \tau_{xz} \\ \tau_{yx} & \sigma_y & \tau_{yz} \\ \tau_{zx} & \tau_{zy} & \sigma_z \end{pmatrix} \tag{1.11}$$

This matrix is *symmetric* i.e. it is equal to its transpose. So there are in fact only 6 linearly independent values. It is convenient to write the stress tensor as a column vector and from this point numerical subscripts will be used, where 1, 2 and 3 represent x, y, and z axes, respectively:

$$\sigma_{ij} = \begin{pmatrix} \sigma_{11} \\ \sigma_{22} \\ \sigma_{33} \\ \tau_{12} \\ \tau_{13} \\ \tau_{23} \end{pmatrix} \tag{1.12}$$

This is the form of the stress tensor that is used to describe the constitutive equations for linear elasticity.

It is useful now to define the von Mises failure criterion as well as the von Mises stress. The von Mises criterion is used as a measure of how close a material is to yielding, and defines a value for the *octahedral* shear stress at which failure is expected to occur. The octahedral shear stress satisfies the condition that two stress states with equal distortion energy have equal octahedral shear stress, which is useful for comparing how close two materials under different stress states (for instance, compression and torsion) are to yielding. The octahedral shear stress is defined as:

$$\tau^{oct} = \frac{1}{3}\sqrt{(\sigma_{11} - \sigma_{22})^2 + (\sigma_{22} - \sigma_{33})^2 + (\sigma_{33} - \sigma_{11})^2 + 6(\tau_{12}^2 + \tau_{23}^2 + \tau_{31}^2)} \tag{1.13}$$

Using this formula, the octahedral shear stress at failure, σ_f for a uniaxial tensile test is:

$$\tau^{oct} = \frac{1}{3}\sqrt{2\sigma_f^2} \tag{1.14}$$

Thus the von Mises stress σ_v is defined as the octahedral stress normalized against the failure stress described above:

$$\sigma_v = \sqrt{\frac{(\sigma_{11} - \sigma_{22})^2 + (\sigma_{11} - \sigma_{33})^2 + (\sigma_{22} - \sigma_{33})^2 + 6(\tau_{12}^2 + \tau_{23}^2 + \tau_{31}^2)}{2}} \tag{1.15}$$

and predicts that a material will fail when $\sigma_v = \sigma_f$.

When a body experiences a stress it deforms. Strain is a dimensionless quantity defined as the ratio of the change in size of an element and its original size. Depending upon whether the size refers to a length, area or volume, the resulting strain is referred to as being linear, planar or volumetric, respectively.

The strain in a body being deformed by an amount u_1 in the x_1-direction is defined as:

$$\varepsilon_1 = \frac{\partial u_1}{\partial x_1} \tag{1.16}$$

and likewise for the 2 and 3 directions. A body being deformed in *shear* by an amount u_2 in the x_2-direction on a plane with normal parallel to x_1 is:

$$\gamma_{xy} = \frac{\partial u_2}{\partial x_1} + \frac{\partial u_1}{\partial x_2} \tag{1.17}$$

It follows that $\gamma_{ij} = \gamma_{ji}$ and therefore a strain tensor can be set up in the exact same way as for stress, and represented as a column vector:

$$\varepsilon_{ij} = \begin{pmatrix} \varepsilon_{11} \\ \varepsilon_{22} \\ \varepsilon_{33} \\ \gamma_{12} \\ \gamma_{13} \\ \gamma_{23} \end{pmatrix} = \begin{pmatrix} \frac{\partial u_1}{\partial x_1} \\ \frac{\partial u_2}{\partial x_2} \\ \frac{\partial u_3}{\partial x_3} \\ \frac{\partial u_1}{\partial x_2} + \frac{\partial u_2}{\partial x_1} \\ \frac{\partial u_1}{\partial x_3} + \frac{\partial u_3}{\partial x_1} \\ \frac{\partial u_2}{\partial x_3} + \frac{\partial u_3}{\partial x_2} \end{pmatrix} \tag{1.18}$$

With stresses and strains defined, we can now describe the constitutive equations that describe their relation. Linear elasticity is a generalization of Hooke's Law, which assumes stresses are proportional to strains:

$$\sigma_{ij} = D_{ijkl}\varepsilon_{kl} \tag{1.19}$$

$$\varepsilon_{ij} = C_{ijkl}\sigma_{kl} \tag{1.20}$$

where D_{ijkl} is the elastic stiffness tensor, and C_{ijkl} is the elastic compliance tensor. In full form, each of these tensors would contain $3^4 = 81$ terms, however the symmetries in the stress and strain tensors reduce this to 36. These 36 term tensors are themselves symmetric, and so using column vector notation for stress and strain it is possible to represent D_{ijkl} and C_{ijkl} as symmetric matrices. In matrix form Equation 1.19 can be written :

$$\begin{pmatrix} \sigma_{11} \\ \sigma_{22} \\ \sigma_{33} \\ \sigma_{12} \\ \sigma_{13} \\ \sigma_{23} \end{pmatrix} = \begin{pmatrix} D_{1111} & D_{1122} & D_{1133} & D_{1112} & D_{1113} & D_{1123} \\ & D_{2222} & D_{2233} & D_{2212} & D_{2213} & D_{2223} \\ & & D_{3333} & D_{3312} & D_{3313} & D_{3323} \\ & & & D_{1212} & D_{1213} & D_{1223} \\ & sym & & & D_{1313} & D_{1323} \\ & & & & & D_{2323} \end{pmatrix} \begin{pmatrix} \varepsilon_{11} \\ \varepsilon_{22} \\ \varepsilon_{33} \\ \frac{1}{2}\gamma_{12} \\ \frac{1}{2}\gamma_{13} \\ \frac{1}{2}\gamma_{23} \end{pmatrix} \tag{1.21}$$

The elastic stiffness need only be described with all 21 terms if it is fully anisotropic (or *triclinic*). Most materials contain inherent symmetry about the three coordinate planes which reduces the number of terms needed to fully describe the elastic behaviour. If this is the case, the material is referred to as *orthotropic*, see Section 3.1.1 for details on defining the orthotropic D-matrix. If the material properties are symmetric about every possible plane, then the material is said to be *isotropic* and the material can be described in terms of two well-known independent constants, the Young's modulus E and the Poisson's ratio ν.

The Young's modulus is a measure of the resistance of a material to deformation in a uniaxial tensile test. The Poisson's ratio is the ratio of lateral expansion/contraction to an applied strain. The D-matrix of an isotropic material can be written in terms of E and ν:

$$\begin{pmatrix} \frac{1}{E} & \frac{-\nu}{E} & \frac{-\nu}{E} & 0 & 0 & 0 \\ & \frac{1}{E} & \frac{-\nu}{E} & 0 & 0 & 0 \\ & & \frac{1}{E} & 0 & 0 & 0 \\ & & & \frac{1}{G} & 0 & 0 \\ & & & & \frac{1}{G} & 0 \\ & & & & & \frac{1}{G} \end{pmatrix} \tag{1.22}$$

where G is the *shear modulus* and is related to E and ν by the equation:

$$G = \frac{E}{2(1+\nu)} \tag{1.23}$$

and defines the resistance of a material to shear strain. The bulk modulus K is the resistance to volumetric strain, and for an isotropic material is defined as:

$$K = \frac{E}{3(1-2\nu)} \tag{1.24}$$

For an orthotropic material the Young's modulus and Poisson's ratio have directional analogues, E_i and ν_{ij} where ν_{ij} is the expansion in the j-direction given a deformation in i. Due to symmetry of the D-matrix, the following relations hold:

$$\begin{aligned} \frac{\nu_{12}}{E_2} &= \frac{\nu_{21}}{E_1} \\ \frac{\nu_{23}}{E_3} &= \frac{\nu_{32}}{E_2} \\ \frac{\nu_{31}}{E_1} &= \frac{\nu_{13}}{E_3} \end{aligned} \tag{1.25}$$

Lastly, it is useful to describe the effective bulk modulus of an orthotropic material:

$$\frac{1}{K^{eff}} = \frac{1}{E_1} + \frac{1}{E_2} + \frac{1}{E_3} + \frac{\nu_{23}}{E_1} + \frac{\nu_{31}}{E_2} + \frac{\nu_{12}}{E_3} \tag{1.26}$$

The governing differential equations and the method for solving linear elastic problems using finite element analysis is explained in Section 1.3.

Elasticity is used to describe the solid phase of transient models, and fully describes the deformation of biological materials in equilibrium. Careful consideration needs to be made as to the timescale of loading before employing complex transient models. Higginson et al. [145] conducted an experiment whereby a sample of cartilage was dynamically loaded at a frequency similar to that of a human walking pace, and found that the transient response during individual steps was negligible compared to the long term time-averaged steady-state loading. A full set of orthotropic elasticity parameters for AC was found by Wang et al. [113] using unconfined compression of cubes of cartilage compressed along the three Cartesian axes.

1.2.2.2 Viscoelasticity

When the stress state of a body is changed, the laws of elasticity predict an instantaneous deformation with no time dependence. In practise, the body undergoes a phenomenon referred to as *creep* whereby the deformation continues with time and tends towards an equilibrium. Similarly, if a body undergoes a sudden and fixed change in strain, the corresponding internal stresses decrease with time. This phenomenon is referred to as *stress relaxation*. These time dependent effects are collectively referred to as viscoelasticity.

Mechanical models of viscoelasticity can be explained in terms of springs and dashpots. Springs represent elastic behaviour of a material, which in one dimension can be summarized with a spring constant μ. A dashpot induces a velocity-dependent drag η when loaded. The effect of loading a one dimensional viscoelastic material can thus be expressed as a combination of the elastic component:

$$F = \mu u \tag{1.27}$$

and the viscous component:

$$F = \eta \dot{u} \tag{1.28}$$

where u and $\dot{u}$ denote the displacement and velocity of the material, respectively.

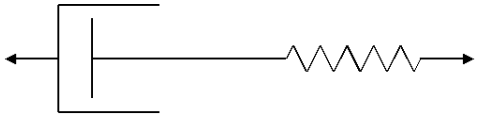

(a) Maxwell body.

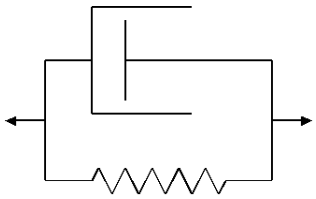

(b) Kelvin-Voigt body.

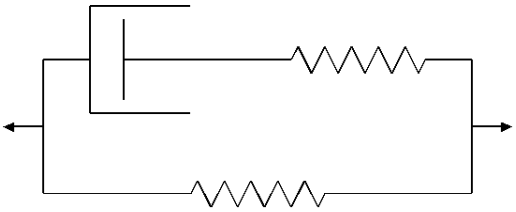

(c) Standard linear body.

Figure 1.18: The three mechanical models of a viscoelastic material. Adapted from [14].

There are three types of constitutive model for viscoelasticity, the Maxwell model, the Kelvin-Voigt model, and the standard linear solid model. Each model differs in the way by which it distributes external force between viscous and elastic components. See Figure 1.20.

In a Maxwell body, any applied force is transmitted through both the spring and the dashpot. This results in a displacement F/μ in the spring and a velocity F/η in the dashpot. The total velocity of deformation can therefore be written as:

$$\dot{u} = \frac{\dot{F}}{\mu} + \frac{F}{\eta} \tag{1.29}$$

The Kelvin-Voigt model assumes a dashpot and spring in parallel, and therefore both components have the same deflection under load. The total force is therefore simply the sum of the viscous and elastic components:

$$F = \mu u + \eta \dot{u} \tag{1.30}$$

The standard linear model (sometimes referred to as the Kelvin model) is a combination of the Maxwell and Kelvin-Voigt models, with a Maxwell element (η_0 and μ_0) in parallel with a second spring, μ_1. It can be shown using force and displacement balance that the constant and time varying components of the force can be written as:

$$F + \frac{\eta_0}{\mu_0}\dot{F} = \mu_1 u + \eta_0 \left(1 + \frac{\mu_1}{\mu_0}\right)\dot{u} \tag{1.31}$$

This can be re-written in the form:

$$F + \tau_\varepsilon \dot{F} = E_R(u + \tau_\sigma \dot{u}) \tag{1.32}$$

where:

$$\begin{aligned} \tau_\varepsilon &= \frac{\eta_0}{\mu_0} \\ \tau_\sigma &= \frac{\eta_0}{\mu_1}\left(1 + \frac{\mu_1}{\mu 0}\right) \\ E_R &= \mu_1 \end{aligned} \tag{1.33}$$

are the relaxation time for constant strain, the relaxation time for constant stress, and the relaxed elastic modulus, respectively. These parameters can be used to describe the creep and stress-relaxation behaviour of viscoelastic materials.

A simple comparison of the creep behaviours of the three viscoelastic models is shown in Figure 1.19. Each graph describes the predicted deformation of a viscoelastic material when a fixed load is instantaneously applied, then later removed. The Maxwell model predicts an instantaneous deformation due to the spring, followed by a linear creep due to the fixed load on the dashpot. On removal of the load, there is no restorative force to reset the dashpot, and thus the material does not return to its original size. The Kelvin-Voigt model shows no instantaneous deformation due to the dashpot being in parallel with the spring, the creep is exponential as the opposing force exerted by the spring is proportional to the deflection. The spring's restorative force causes the deformation to return to zero after removal of load. Behaviour related to both the Maxwell and Kelvin-Voigt models are evident in the standard linear model.

The equivalent comparison of stress-relaxation behaviours is described in Figure 1.20. Instead of a fixed load, an instantaneous fixed deformation is applied instead. The Maxwell model predicts a peak initial force followed by an exponential decrease to zero as the restorative force of the spring is balanced with the viscous resistance of the dashpot. The Voigt model does not support this type of test as the dashpot does not allow an instantaneous deformation, resulting in a delta function at the application of deformation. The standard linear model is similar to the Maxwell model, although the force does not return to zero (due to spring μ_1).

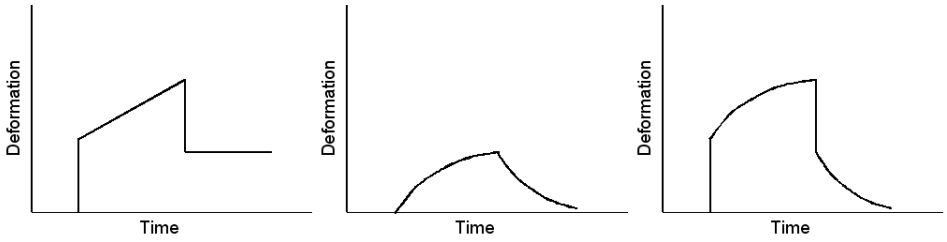

Figure 1.19: The three mechanical models of viscoelastic creep. Each graph represents an applied instantaneous fixed load followed by a period of creep, then the instantaneous removal of the load. From left to right: Maxwell, Kelvin-Voigt, and standard linear solid models.[14]

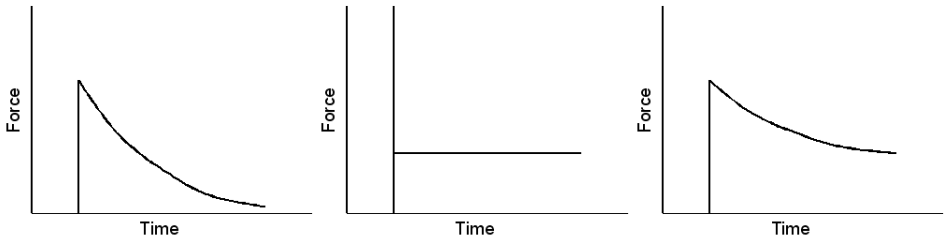

Figure 1.20: The three mechanical models of viscoelastic stress-relaxation. From left to right: Maxwell, Kelvin-Voigt, and standard linear solid models.

More general models involve adding more elements to the standard linear solid model. This takes into account that creep and stress relaxation can occur at a range of times depending upon the microscopic (or molecular) arrangement of the material. The most general case was proposed by Boltzmann in which the force $F(t)$ and deflection $u(t)$ are described as functions of the total history of the loading up to time t. A small change in the deflection du at time t is the result of a change in the applied force F at time T. A single incremental change in loading is $(dF/dT)dT$. The relationship between u and F is a function of the time interval $t - T$, therefore:

$$du(t) = c(t - T)\frac{dF(t)}{dT}dT \tag{1.34}$$

where $c(t - T)$ is a proportionality function referred to as the creep function. Assuming load and deformation commenced at time $T = 0$ then by summing over the history of the deformation we obtain:

$$u(t) = \int_0^t c(t - T)\frac{dF(t)}{dT}dT \tag{1.35}$$

Similarly, exchanging u and F and introducing the stress-relaxation function $k(t - T)$ we also obtain:

$$F(t) = \int_0^t k(t-T)\frac{du(t)}{dT}dT \tag{1.36}$$

The creep and stress-relaxation functions can be obtained by solving the constitutive differential equation of the model of interest for either F or u.

These relations can be extended to describe a viscoelastic solid in terms of the time-dependent stress and strain matrices in 3D assuming infinitessimal strains (linear viscoelasticity). Replacing the stress-relaxation function with its tensorial counterpart $J_{ijkl}(\mathbf{r}, t-T)$ and likewise for the creep function $G_{ijkl}(\mathbf{r}, t-T)$, the stress and strain are related by the following convolution integrals:

$$\sigma_{ij}(r_i, t) = \int_{-\infty}^t G_{ijkl}(r_i, t-T)\frac{\partial \varepsilon_{kl}(r_i, T)}{\partial T}dT \tag{1.37}$$

$$\varepsilon_{ij}(r_i, t) = \int_{-\infty}^t J_{ijkl}(r_i, t-T)\frac{\partial \sigma_{kl}(r_i, T)}{\partial T}dT \tag{1.38}$$

A common method for determining the viscoelastic properties of a material, particularly biological specimens, is to subject it to periodic loads [146, 147]. A purely elastic material will exhibit stress and strain responses in phase with each other, whereas a viscoelastic material will exhibit a phase lag. The strain in a purely viscous material subjected to such dynamic loading will lag the stress by $\pi/2$ radians. This behaviour is *hysteretic* indicating there is thermal energy loss during each cycle. When the stress-strain behaviour has been recorded, the phase difference δ can be used to calculate the elastic and viscous portions of the response which are referred to as the storage (E') and loss (E'') moduli, respectively:

$$E' = \frac{\sigma_0}{\varepsilon_0}\cos\delta \tag{1.39}$$

$$E'' = \frac{\sigma_0}{\varepsilon_0}\sin\delta \tag{1.40}$$

where σ_0 and ε_0 are the amplitude of the cyclic stress and strain, respectively. These two moduli can be lumped together into the dynamic, or complex modulus:

$$E = E' + E'' \tag{1.41}$$

Viscoelastic models are rarely used as complete material models of biological material now that poroelastic and multiphasic models exist, however viscoelastic principles are

still incorporated into many models ([148, 149, 32, 150, 151]. Guilak et al. [79] used viscoelasticity to describe the equilibrium and transient deformation behaviour of chondrocytes, and the variations with osteoarthritis. It was found that although there was no significant change in the equilibrium Young's modulus of the chondrocytes with OA, there was a marked change in the stress-relaxation time constant, as well as the instantaneous stiffness. This suggests that the viscoelastic effects may play a role in defining the mechanical response of chondrocytes under stress.

One of the most comprehensive models of the mechanical properties of AC currently used is the fibril reinforced poroviscoelastic (FRPVE) model [148]. This is essentially a poroelastic model (explained in the next section) which includes a viscoelastic fibrillar component which replicates the contribution of collagen fibres to the mechanical properties. The viscoelastic model chosen to represent this behaviour is similar to the standard linear body described in Figure 1.18c, only with a nonlinear spring $\mu_1 = \mu_\varepsilon \varepsilon$ instead of a linear spring in parallel to the Maxwell element.

1.2.2.3 Poroelasticity

Poroelasticity is a mechanical model which describes the deformation behaviour of fluid saturated porous media. The underlying theory assumes an elastic matrix filled with interconnected pores, with associated stresses and strains that can contain contributions from the hydrostatic pressure of the fluid. Loading of a poroelastic solid results in hydrostatic pressure gradients which causes the fluid to flow. Flow characteristics are governed by the permeability of the matrix, as well as the void ratio (the volume ratio of fluid to solid).

The theoretical treatment of poroelasticity is explained in detail by Cowin [152], Cowin and Mehrabadi [153] and this section is based on these references. The stress-strain-pore pressure constitutive relation relates an induced strain ε_{ij} to both the solid stress σ_{kl} and the hydrostatic pressure p:

$$\varepsilon_{ij} = C_{ijkl}(\sigma_{kl} + A_{kl}p) \tag{1.42}$$

where C_{ijkl} is the elastic compliance tensor defined in Section 1.2.2.1 of the porous matrix, and A_{kl} is the Biot effective stress coefficient vector. Similarly, this can be written in terms of the elastic stiffness tensor D_{ijkl}:

$$\sigma_{ij} + A_{ij}p = D_{ijkl}\varepsilon_{kl} \tag{1.43}$$

These equations can be simplified by introducing an *effective stress* σ_{ij}^{eff}:

$$\sigma_{ij}^{\text{eff}} = \sigma_{ij} + A_{ij}p \tag{1.44}$$

reducing 1.42 to:

$$\varepsilon_{ij} = C_{ijkl}\sigma_{kl}^{\text{eff}} \tag{1.45}$$

A_{ij} can be thought of as defining the force transfer mechanism between the fluid and solid phase. As such, it is dependent not only on the porous matrix elastic compliance C_{ijkl}, but also the elastic compliance of the solid matrix (containing no pores), C_{ijkl}^{m}. It therefore takes two experiments to initially determine the elastic coefficients, corresponding to testing the sample with and without the effect of fluid flow. A no-flow experiment is analagous to an experiment on a drained sample and can be performed by either draining the sample, or performing the experiment slowly enough that there is negligible pressure change. In such an experiment A_{ij} is related to the compliance tensors by the formula:

$$A_{ij} = C_{ijkl}^{-1}A_{kl}^{*} \quad \text{where} \quad A_{ij}^{*} = C_{ijkl}A_{kl} = (C_{ijkl} - C_{ijkl}^{m})I_{kl} \tag{1.46}$$

where I_{kl} is the identity matrix and A_{ij}^{*} is referred to as the compliance difference tensor.

The next step is to introduce notation for the volume fraction, ϕ, density ρ_f and variation in content ζ of fluid. The variation in fluid content requires a reference configuration for which variables are given the subscript 0:

$$\zeta \equiv \frac{\rho^f}{\rho_0^f}\phi - \phi_0 \tag{1.47}$$

This completes the definitions of the field variables used in poroelasticity. The set of variables can be viewed as conjugate pairs of stress measures (σ, p) and strain measures (ε, ζ). The variation in fluid content can be expressed as:

$$\zeta = A_{ij}^{*}\sigma_{ij} + C^{\text{eff}}p \quad \text{where} \quad C^{\text{eff}} = \frac{1}{K^{\text{eff}}} - \frac{1}{K^{m,\text{eff}}} + \phi\left(\frac{1}{K^{f}} - \frac{1}{K^{m,\text{eff}}}\right) \tag{1.48}$$

where K^{eff} is the effective bulk modulus defined in Equation 1.26 and the superscripts m and f refer to the solid matrix and fluid, respectively.

Before the constitutive equations of poroelasticity can be defined, the pressure-induced mass flux, q_i must be defined using Darcy's law:

$$q_i = -\frac{1}{\mu} K_{ij} \nabla_i p \tag{1.49}$$

where K_{ij} is the intrinsic permeability tensor and μ is the fluid viscosity. From these relations we can now derive the equations of poroelasticity.

Conservation of mass states that:

$$\frac{\partial \rho}{\partial t} + \nabla \cdot (\rho v_i) = 0 \tag{1.50}$$

and conservation of momentum states that:

$$\rho \frac{\partial^2 u_i}{\partial t^2} = \nabla_i \sigma_{ji} + \rho b_i \tag{1.51}$$

where b_i signifies a body force. To modify Equation 1.50 so it applies to a pore fluid volume, the density term becomes the fluid density multiplied by the fluid volume fraction $\phi \rho^f$. The addition of a mass source term $\gamma \rho_0^f$ allows for sources or sinks of fluid to exist within the model. The relation is normalized against ρ_0^f:

$$\frac{1}{\rho_0^f} \frac{\partial (\phi \rho^f)}{\partial t} + \frac{1}{\rho_0^f} \nabla_i (\phi \rho^f v_i) = \gamma \tag{1.52}$$

Referring back to Equations 1.47 and 1.49, the form of Equation 1.52 becomes:

$$\frac{\partial \zeta}{\partial t} + \nabla_i \cdot q_i = \gamma \tag{1.53}$$

which states simply that the rate of change of fluid content is due to either fluid flux or internal sources or sinks of fluid. This can now include contributions from the stress and pressure by replacing ζ and q with Equations 1.48 and 1.49:

$$C^{\text{eff}} \frac{\partial p}{\partial t} - \frac{1}{\mu} K_{ij} O_{ji} p = \gamma - \frac{\partial}{\partial t} (A_{ij}^* \sigma_{ji}) \tag{1.54}$$

where O is the double gradient function $O_{ij} = \nabla_i \nabla_j$:

$$\begin{bmatrix} \frac{\partial^2}{\partial x_1^2} & \sqrt{2}\frac{\partial^2}{\partial x_1 \partial x_2} & \sqrt{2}\frac{\partial^2}{\partial x_1 \partial x_3} \\ \sqrt{2}\frac{\partial^2}{\partial x_2 \partial x_1} & \frac{\partial^2}{\partial x_2^2} & \sqrt{2}\frac{\partial^2}{\partial x_2 \partial x_3} \\ \sqrt{2}\frac{\partial^2}{\partial x_3 \partial x_1} & \sqrt{2}\frac{\partial^2}{\partial x_3 \partial x_2} & \frac{\partial^2}{\partial x_3^2} \end{bmatrix} \tag{1.55}$$

This is the last equation needed to solve a poroelasticity problem. Boundary conditions in poroelastic models used when solving this differential equation define either the pressure

p, the pressure gradient $\nabla_i p$ or a linear combination of the two. The resulting problem is that of 17 scalar unknowns and 17 scalar equations. The unknowns are the six components of the stress σ_{ij} and strain ε_{ij} tensors, the fluid pressure p, the variation in fluid content ζ and the three components of the displacement vector u_i. The 17 scalar equations of the theory of poroelastic solids are the six equations of the stress-strain-pressure relation, Equation 1.42, the six strain-displacement relations, Equation 1.18, the three momentum conservation relations, Equation 1.51, the one fluid content-stress-pressure relation, Equation 1.48 and the mass conservation, Equation 1.54. This is all that is required to solve a poroelasticity problem with the displacement u_i set as the independent variable. To solve for other independent variables, the use of compatability equations derived and explained in by Cowin [152] are necessary.

The poroelastic model was employed by Higginson et al. [145] to investigate the load-displacement-time characteristics of articular cartilage by modelling the results of a dynamic confined compression experiment, and found that the contribution of each cycle to the total deformation was negligible. More recently, Wan and Li [97] used a poroelastic model to investigate the effect of variations in the permeability of human ankle AC with depth in the analysis of joint contact problems, and it was found to be significant. To accurately recreate the transient deformation behaviour of AC *in vivo*, the depth-dependent permeability needs to be thoroughly investigated.

1.2.2.4 Multiphasic theory

Multiphasic theory describes cartilage as a mixture of two or more *phases*. In biphasic theory the two phases are the solid and liquid components of cartilage, triphasic theory goes on to include a phase describing the ionic component, and quadriphasic theory splits the ionic component into separate anionic and cationic phases. Multiphasic theory is based on mixture theory developed by Craine et al. [154] and Bowen [155]. This section focuses on biphasic theory and is based on a full derivation in a thesis by Lu [156]. Some comments on more complex models are included at the end.

In a mixture, the theory assumes that every spatial point is co-occupied by a material point belonging to each phase. Hence, for every point x_i in a mixture, each phase α must have a corresponding material point, defined by its original location X_i and time t:

$$x_i^\alpha = x_i^\alpha(X_i^\alpha, t) \tag{1.56}$$

with the velocity and acceleration of each phase calculated in the usual way. An important concept in mixture theory is that of volume fraction, which for a specific phase is defined as the ratio of the constituent volume to the volume of the whole mixture:

$$\phi^\alpha = \frac{dV^\alpha}{dV} \tag{1.57}$$

Before biphasic relations can be defined, the basic equations for the mechanics of mixtures need to be stated. Firstly balance of mass:

$$\frac{\partial \phi^\alpha}{\partial t} + \nabla_i \cdot (\phi^\alpha v_i^\alpha) = 0 \tag{1.58}$$

Balance of linear momentum:

$$\rho \frac{dv_i}{dt} = \nabla_j \cdot \sigma_{ij}^m + \rho b_i \tag{1.59}$$

where ρ is the density of the whole mixture, b_i is the mass-weighted average body force on the system and σ_{ij}^m is the mixture stress tensor, defined by:

$$\sigma_{ij}^m = \sum_\alpha (\sigma_{ij}^\alpha - \rho^\alpha v_i^\alpha v_j^\alpha) \tag{1.60}$$

where σ_{ij}^α is the standard Cauchy stress tensor for the α^{th} phase. Conservation of energy states that:

$$\rho^\alpha \frac{d\varepsilon^\alpha}{dt} = -\nabla_i \cdot q_i^\alpha + \rho^\alpha r^\alpha + \epsilon_s^\alpha + \pi_i \cdot w_i^\alpha + (\sigma_{ij}^\alpha F_{ij}^\alpha)\delta_{ij} \tag{1.61}$$

where ϵ^α is the internal heat supply, q_i^α is the heat flux vector, r^α is the external heat supply density, π_i is the linear momentum transfer caused by interaction with other phases, w_i^α is the diffusional velocity $w_i^\alpha = v_i^\alpha - v_i$ and F_{ijkl} is the rate of deformation tensor given by:

$$F_{ij}^\alpha = \frac{1}{2}\left[(\nabla_i v_j^\alpha) + (\nabla_i v_j^\alpha)^T\right] \tag{1.62}$$

By using the principle of mixtures, Equation 1.61 simplifies to:

$$\sum_\alpha (\epsilon_s^\alpha + \pi_i^\alpha \cdot w_i^\alpha) = 0 \tag{1.63}$$

This is all the kinematic mixture equations necessary to derive biphasic theory. Lastly, the second law of thermodynamics is required to derive the constitutive equation. Mow et al. [104] used the Clausius-Duhem inequality as a statement of the second law, which is assumed to hold both locally and for the entire mixture:

$$\sum_{\alpha} \frac{1}{T} \left[\rho^{\alpha} \left(\frac{d\eta^{\alpha}}{dt} - \frac{d\epsilon^{\alpha}}{dt} \right) + (\sigma_{ij}^{\alpha} F_{ij}^{\alpha}) \delta_{ij} - \pi_i^{\alpha} \cdot w_i^{\alpha} \right] \geq 0 \tag{1.64}$$

where η^{α} is the specific entropy of the α^{th} phase and T is the absolute temperature. The biphasic theory governing equations can now be written. In biphasic theory, the two phases are fluid and solid, hence $\alpha = s$ or f. The theory assumes that the material is always saturated, and so there is no 'empty space' and therefore:

$$\phi_f + \phi_s = 1 \tag{1.65}$$

In the form below it is assumed that there are no external body forces, and deformations are considered small enough to be described adequately using linear elasticity. Inertial and viscous effects are also ignored. The balance of mass (Equation 1.58) for the two phases becomes:

$$\frac{\partial \phi^s}{\partial t} + \nabla \cdot (\phi^s v_i^s) = 0 \tag{1.66}$$

$$\frac{\partial \phi^f}{\partial t} + \nabla \cdot (\phi^f v_i^f) = 0 \tag{1.67}$$

Combining the two and including Equation 1.65 the biphasic continuity equation can be stated as:

$$\nabla_i \cdot (\phi^f v_i^f + \phi^s v_i^s) = 0 \tag{1.68}$$

The balance of linear momentum for the two phases becomes:

$$\begin{aligned} \nabla_i \cdot \sigma_{ij}^s + \pi_j^s &= 0 \\ \nabla_i \cdot \sigma_{ij}^f + \pi_j^f &= 0 \end{aligned} \tag{1.69}$$

where π_i^s and π_i^f are the momentum supplies to the solid and fluid phases, respectively, and therefore:

$$\pi_i^s = -\pi_i^f = \pi_i \tag{1.70}$$

i.e. the momentum supply represents the interaction due to the fluid flowing relative to the deforming solid phase. The constitutive equation can then be derived using the Helmholtz free energy density. This introduces a variable A^{α} which represents the amount

of internal energy within the system available to produce mechanical work at constant temperature:

$$A^\alpha = \epsilon^\alpha - T\eta^\alpha \tag{1.71}$$

For a biphasic mixture, incorporation of the Clausius-Duhem inequality and the incompressibility assumption results in:

$$\left[-\rho^s \frac{dA^s}{dt} + ((\phi^s p I_{ij} + \sigma^s_{ij})D^s_{ij})\delta_{ij}\right] + \left[-\rho^f \frac{dA^f}{dt} + ((\phi^f p I_{ij} + \sigma^f_{ij})D^f_{ij})\delta_{ij}\right] + (\pi_i + p\nabla_i \phi^f)(v^f_i - v^s_i) \geq 0 \tag{1.72}$$

To make this equation useful for biphasic mechanical modeling, the term A^α needs to be expressed in a quantifiable form for the solid and fluid phases. Mow et al. [104] chose to express the strain energy density of the solid phase in terms of A:

$$W^E = \rho^s A^s = \frac{1}{2}\varepsilon_{ij} D_{ijkl} \varepsilon_{lk} \tag{1.73}$$

where ε_{ij} is the infinitessimal strain tensor (Equation 1.18) and D_{ijkl} is the Cauchy stiffness matrix (Equation 1.21). The inequality described in Equation 1.72 is thus satisfied if the solid stress is of the form:

$$\sigma^s_{ij} = -\phi^s p I_{ij} + D_{ijkl}\varepsilon_{kl} \tag{1.74}$$

This effectively splits the stress in the solid matrix into a pressure term and an 'extra stress' term. The fluid phase is a simpler affair as the effect of fluid-fluid viscosity has been found to be several magnitudes lower than that of the extra stress in the solid phase [103] and hence can be ignored:

$$\frac{dA^f}{dt} = 0 \tag{1.75}$$

meaning that the constitutive law for the fluid phase is:

$$\sigma^f_{ij} = -\phi^f p I_{ij} \tag{1.76}$$

The final constitutive law in biphasic theory is that of the momentum supply π_i. From Equation 1.72, the diffusional drag coefficient tensor K_{ij} is introduced and defined as:

$$\pi_i = -p\nabla_i\phi^f + K_{ij}\cdot(v_j^f - v_j^s) \tag{1.77}$$

in which the first term can be described as a buoyant force due to gradient in volume fraction, and the second term representing the diffusive resistance due to relative movement between the two phases.

In summary, the reduced governing equations for a biphasic material at infinitessimal strains can be summarised as follows. Firstly, the continuity equation (1.68) is:

$$\nabla\cdot(\phi^f v_i^f + \phi^s v_i^s) = 0 \tag{1.78}$$

The constitutive equations are inserted into the linear momentum equations to find the other two governing equations:

$$-\phi^s\nabla_i p + \nabla_i\cdot\sigma_{ij} + \frac{(\phi^f)^2}{\kappa}(v_i^f - v_i^s) = 0 \tag{1.79}$$

$$-\phi^f\nabla_i p + \frac{(\phi^f)^2}{\kappa}(v_i^f - v_i^s) = 0 \tag{1.80}$$

where κ is the hydraulic permeability. It is generally a strain-dependent value and has been experimentally measured by Lai and Mow [157] to follow an empirical trend:

$$\kappa = \kappa_0\exp(M\varepsilon) \tag{1.81}$$

where κ_0 and M are material constants. The biphasic model has been used extensively to investigate the effects of numerous properties on the mechanical response of AC. Armstrong and Mow [57] performed confined compression experiments on cartilage explants and used biphasic theory to calculate the aggregate modulus and permeability of samples as they varied with age, degeneration and water content. Mak et al. [122] went on to develop a theoretical analysis of the indentation test in order to determine the biphasic material parameters of AC *in vivo*.

The biphasic theory was expanded by Lai et al. [158] to include electrochemical contributions from the FCD and ion concentrations. A new 'ion phase' was introduced and thus triphasic theory was born. In triphasic theory, the constitutive equations for the total stress σ_{ij}^t, fluid stress σ_{ij}^f, water chemical potential μ^f and salt chemical potential μ^i are given by:

$$\sigma_{ij}^{t} = -pI_{ij} - T^{C}I_{ij} + D_{ijkl}\varepsilon_{kl} \tag{1.82}$$

$$\sigma_{ij}^{f} = -\phi^{f}pI_{ij} = \sigma_{ij}^{w} + \sigma_{ij}^{+} + \sigma_{ij}^{-} \tag{1.83}$$

$$\mu^{f} = \mu_{0}^{f} + \frac{1}{\rho_{T}^{f}}\left[p - RT\pi(2c + c^{F}) + B^{f}\varepsilon\right] \tag{1.84}$$

$$\mu^{i} = \mu_{0}^{i} + \frac{RT}{M^{i}}\ln\left[\gamma_{\pm}^{2}c(c + c^{F})\right] \tag{1.85}$$

where T^C is the chemical expansion stress, σ_{ij}^{w} is the water stress, $\sigma_{ij}^{\pm}$ is the anion/cation stress tensor, ρ_T^f is the density of water, R is the universal gas constant, T is the temperature, c is the neutral salt concentration, c^F is the fixed charged density, B^f is the coupling coefficient of the chemical potentials, M^i is the molar weight of NaCl and $\gamma_\pm$ is the mean activity coefficient of ions. A finite element method was developed for solving triphasic models by Sun et al. [159], and Lu et al. [51] developed an analysis for determining the triphasic material parameters from indentation tests.

1.3 Numerical Methods

The finite element method (FEM) is a numerical method for finding approximate solutions to partial and ordinary differential equations. Many physical principles are governed by differential equations, which can only be solved assuming very simple geometry. Most engineering problems, such as the deformation behaviour of a crashing car, or the convection of heat in a power plant, can not be approximated to a geometry for which a differential equation can be solved analytically. These kinds of problems are approximated using a numerical technique such as FEM. The technique of FEM is explained loosely in this section to provide a general overview. For detailed examples and derivations see Bhatti [160]. Vector notation is used in this section to keep the algebra neat.

FEM involves discretizing the geometry into a number of simpler geometries called *elements*, which consist of interconnected points called *nodes*. The solution over each element is approximated by first calculating the specific solutions at each node. The solutions at each node are referred to as *nodal degrees of freedom* of which there can be more than one at each node (such as the various translations and rotations in the case of 3D elasticity). The application of FEM has 6 steps:

1. Development of element equations
2. Discretization of solution domain into a finite element mesh
3. Assembly of element equations

4. Introduction of boundary conditions
5. Solution for nodal unknowns
6. Computation of solution and related quantities over each element

The choice of element is the first step towards solving a FE model. Choices depend upon the nature of the problem as well as the geometry of the domain. For example, linear elements with straight edges will not approximate curved edges particularly well unless a large number are used. Linear elements are most basic and only contain nodes at their vertices, but solutions over linear elements are faster to find than other more complicated elements. A balance needs to be found between the desired accuracy and the computation time, and sometimes using fewer nonlinear (curved) elements can provide more accurate results quicker than using linear elements.

Element equations essentially define how the physical properties in question vary over an individual element depending upon the nodal values. To set up the element equation for a linear elastic element, a basis (or interpolation) function unique to the chosen element type is used to express the principle strains in terms of displacements for each node. The displacements u, v and w (in the x, y and z direction, respectively) over an element can be described as:

$$\begin{aligned} u(x,y,z) &= N_1u_1 + N_2u_2 + N_3u_3 + ... \\ v(x,y,z) &= N_1v_1 + N_2v_2 + N_3v_3 + ... \\ w(x,y,z) &= N_1w_1 + N_2w_2 + N_3w_3 + ... \end{aligned} \tag{1.86}$$

Where u_i, v_i and w_i represent the displacements at the ith node and N_i represents the basis function for that node. An example [160] of a basis function N for a 2D triangular element is detailed below.:

$$\begin{pmatrix} u(x,y) \\ v(x,y) \end{pmatrix} = \begin{pmatrix} N_1 & 0 & N_2 & 0 & N_3 & 0 \\ 0 & N_1 & 0 & N_2 & 0 & N_3 \end{pmatrix} \begin{pmatrix} u_1 \\ v_1 \\ u_2 \\ v_2 \\ u_3 \\ v_3 \end{pmatrix} \equiv \mathbf{N}^T\mathbf{d} \tag{1.87}$$

where $\mathbf{d}$ is the vector of nodal degrees of freedom, the information we are trying to find. The components N_i for a triangular element are defined as:

$$\begin{pmatrix} N_1 \\ N_2 \\ N_3 \end{pmatrix} = \frac{1}{2A} \begin{pmatrix} xb_1 + yc_1 + f_1 \\ xb_2 + yc_2 + f_2 \\ xb_3 + yc_3 + f_3 \end{pmatrix} \tag{1.88}$$

$$\begin{aligned} b_1 &= y_2 - y_3 & b_2 &= y_3 - y_1 & b_3 &= y_1 - y_2 \\ c_1 &= x_3 - x_2 & c_2 &= x_1 - x_3 & c_3 &= x_2 - x_1 \\ f_1 &= x_2y_3 - x_3y_2 & f_2 &= x_3y_1 - x_1y_3 & f_3 &= x_1y_2 - x_2y_1 \end{aligned}$$

where A is the element area. The basis function in this case essentially linearises the displacement over the element. The element strain can therefore be written as:

$$\boldsymbol{\varepsilon} = \begin{pmatrix} \varepsilon_x \\ \varepsilon_y \\ \gamma_{xy} \end{pmatrix} = \begin{pmatrix} \frac{\partial u}{\partial x} \\ \frac{\partial v}{\partial y} \\ \frac{\partial u}{\partial x} + \frac{\partial v}{\partial y} \end{pmatrix} = \frac{1}{2A} \begin{pmatrix} b_1 & 0 & b_2 & 0 & b_3 & 0 \\ 0 & c_1 & 0 & c_2 & 0 & c_3 \\ c_1 & b_1 & c_1 & b_2 & c_3 & b_3 \end{pmatrix} \begin{pmatrix} u_1 \\ v_1 \\ u_2 \\ v_2 \\ u_3 \\ v_3 \end{pmatrix} = \mathbf{B}^T\mathbf{d} \tag{1.89}$$

$\mathbf{B}$ is the strain-displacement matrix. With the strain now expressed in terms of nodal displacements, substituting Hooke's law gives:

$$\boldsymbol{\sigma} = \mathbf{D}\boldsymbol{\varepsilon} = \mathbf{D}\mathbf{B}^T\mathbf{d} \tag{1.90}$$

where $\mathbf{D}$ is the Cauchy stiffness matrix (Equation 1.21). We now introduce the element stiffness matrix $\mathbf{k}$ which relates $\mathbf{d}$ to the vector of applied stresses, $\mathbf{r}$:

$$\mathbf{k}\mathbf{d} = \mathbf{r} \tag{1.91}$$

This is the *element equation,* where $\mathbf{r}$ contains the model's pre-specified stress values. If a node is not part of an edge where a load is directly applied, its corresponding r values are zero. The element stiffness matrix arises from the formula for strain energy:

$$U = \frac{1}{2} \iiint_V \boldsymbol{\varepsilon}^T \boldsymbol{\sigma} \, \mathrm{d}V \tag{1.92}$$

which, substituting in Equations 1.89 and 1.90, gives:

$$U = \frac{1}{2}\mathbf{d}^T \iiint_V \mathbf{B}\mathbf{C}\mathbf{B}^T \, \mathrm{d}V \, \mathbf{d} = \frac{1}{2}\mathbf{d}^T \mathbf{k} \mathbf{d} \tag{1.93}$$

$$\mathbf{k} = \frac{1}{2} \iiint_V \mathbf{B}\mathbf{C}\mathbf{B}^T \, \mathrm{d}V \tag{1.94}$$

This formula for the element stiffness matrix applies for all elements. In the case of the 2D triangular element there is no dependence on x or y, so the integral is trival and $\mathbf{k}$ can simply be written as:

$$\mathbf{k} = hA\mathbf{B}\mathbf{C}\mathbf{B}^T \tag{1.95}$$

where h is the thickness of the element. Hence, $\mathbf{k}$ is a square matrix with a total number of elements equal to the number of degrees of freedom squared.

With the element equation specified, the geometry can be discretised and the element equations assembled for solving. The discretised geometry is referred to as a *mesh*. The mesh controls the accuracy of a finite element analysis, and a finer mesh (with more elements) generally produces more accurate results at the cost of computation time. Bhatti [160] lists a number of points for creating good finite element meshes:

- *Geometry*: Element formation must follow the geometry as closely as possible. In regions where the mesh can not follow boundaries exactly (such as linear elements over a curved domain) then a finer mesh will provide more geometric accuracy.
- *Desired accuracy*: As stated above, a finer elements provides more accuracy. A coarse mesh is often used to test the validity of a model before committing to a finely meshed model for detailed analysis.
- *Solution characteristics*: If a model solution changes rapidly in a specific region, or the behaviour in such a region is of particular interest, then adjusting the mesh resolution in that area will provide more accurate and valid results.
- *Computational resources*: Finite element analysis can be very computationally intensive. Fine meshes require large amounts of random access memory, and models with multiple computation steps require a very large number of computation cycles, which require a fast processor to process in a reasonable amount of time. Limitations of computer hardware must be considered when creating a FE mesh.
- *Element interfaces*: It is important that elements sharing an edge also share the same nodes.

- *Symmetry*: A method of simplifying geometry is to take advantage of symmetry. A model containing symmetry in the geometry, boundary conditions and load (or other physical variable) can be completely modelled by constructing a mesh of one part of the repeating pattern.

Once the geometry has been discretised, numerical values can be inserted into the element stiffness matrix **k** for each element. With these values specified, they can be assembled into a global equation for the entire model. This equation is of the same form as the element equation:

$$\begin{pmatrix} k_{11} & k_{12} & \dots & k_{1n} \\ k_{21} & k_{22} & \dots & k_{2n} \\ \vdots & \vdots & \ddots & \vdots \\ k_{n1} & k_{n2} & \dots & k_{nn} \end{pmatrix} \begin{pmatrix} d_1 \\ d_2 \\ \vdots \\ d_n \end{pmatrix} = \begin{pmatrix} r_1 \\ r_2 \\ \vdots \\ r_n \end{pmatrix} \tag{1.96}$$

where n signifies the number of nodal degrees of freedom (in the case of the 2D elastic triangular mesh this would be the number of nodes times two, i.e. the x and y strain at each node). Where more than one element contributes to a term in the **k** or **r** matrices, the contributions are added together. Once the assembly equation is written, any boundary conditions or point loads can be directly introduced into the **d** or **r** vectors, respectively.

The model is now written in terms of n linear equations, and to solve the model two different techniques can be used, Choleski decomposition and conjugate gradient method. These techniques are described in books such as [160] and are included in most mathematical packages. Once the nodal solution for **d** has been found, the basis functions for each element are used to describe the behaviour of the results across the entire geometry.

1.4 Imaging of Cartilage

Cartilage has been imaged in numerous ways to determine its structure and composition. Techniques such as polarised light microscopy and differential interference/Nomarski microscopy are optical techniques which involve using optical effects of anisotropies and heterogeneities in samples to reveal detail that would otherwise be invisible via stereomicroscopy. These techniques have been used extensively for imaging collagen fibre arrangement [31, 32, 29, 30, 129].

Confocal laser scanning microscopy is a fluorescence technique which involves raster scanning a fluorescently stained sample and collecting the emitted fluorescence. The advantage of this technique is the high resolution and depth selectivity, attributed to the use of a

pinhole when focussing the collected fluorescence. Confocal microscopy has been used to image the morphology of cells [129], but the requirement of fluorophores, which are potentially damaging to introduce to AC for imaging means label-free nonlinear optical techniques are generally preferred, especially when performing mechanical testing, which requires untreated samples.

Magnetic resonance imaging (MRI) is an imaging technique which is useful for its high contrast and depth penetration, allowing the imaging of intact joints *in vivo* without the use of stains or ionising radiation. MRI involves applying a powerful magnetic field across the region of interest, which has the effect of causing the protons in the hydrogen atoms in water to align with the magnetic field. After the magnetic field is removed the protons return to their original alignment, and this realignment provides a signal which can be detected. MRI has been used for determining the topology of entire joints such as the ankle [97] for physiological modeling.

Infrared spectroscopy is a method of chemical analysis that involves determining the amount of electromagnetic absorption a material exhibits under an incident monochromatic source. Fourier transform IR spectroscopy (FTIR) works in a different way, whereby a broadband source with a varying spectrum is incident upon the sample, and a fourier transform is used to calculate a spectrum from either the absorbed or emitted light. FTIR has been used to determine the collagen density of cartilage samples for creating anatomically accurate fibril-reinforced models [32].

Multiphoton optical techniques such as two photon fluorescence (TPF), second harmonic generation (SHG) and coherent anti-stokes Raman scattering (CARS) are nonlinear and are used in preference to other imaging modalities due to their submicron resolution, depth penetration and the ability to image intact samples without staining. These techniques originate from the behaviour of the electric polarisation P_i at high electric fields. For a material irradiated by light of the intensity used in standard optical microscopy, this relationship can be written as: [161]

$$P_i = \varepsilon_0 \chi_{ij} E_j \tag{1.97}$$

where $\varepsilon_0 = 8.85 \times 10^{-12}\mathrm{Fm}^{-1}$ is the permittivity of free space and χ is the electric susceptibility tensor (a constant in the case of linear isotropic materials). At high electric fields, nonlinear terms become significant and the electric polarization is written in terms of a power series in E:

$$P_i = \varepsilon_0 \left(\chi^{(1)}_{ij} E_j + \chi^{(2)}_{ijk} E_j E_k + \chi^{(3)}_{ijkl} E_j E_k E_l + ... \right) \tag{1.98}$$

Each subscripted E corresponds to the electric field of individual interacting photons. The values of $\chi_{ij}^{(1)}$ are much greater than those of the higher order susceptibility tensors, hence the nonlinear terms only contribute at high-amplitude fields.

TPF is used in Chapter 5 to investigate the microscopic effects of externally applied strain on the microstructure of AC. TPF visualises the elastin network in the surface of cartilage, making it a useful tool for investigating the role of elastin in the mechanical response to load. The imaging techniques described in this section are designed to investigate the following:

- The contributions of the various components of AC to the stress and strain propagation under load.
- The effect of stress and strain on the microstructure of AC.

Such techniques are required to be non-invasive and to be performed whilst simultaneously loading the cartilage sample. In order to do so a loading rig was designed so as to allow both epi and forward imaging on the multiphoton microscope (Section 2.3).

1.4.1 Theory of Two Photon Fluorescence

Standard fluorescence excitation involves the absorption of a single photon by a fluorophore. A small amount of the absorbed energy is dissipated before the fluorophore is de-excited by the emission of a redshifted photon. Two-photon fluorescence involves the simultaneous absorption of two photons in a single quantum event, which is described as a temporal window of 10^{-16}s (0.1fs) [162], followed by a similar dissipation of energy and the emission of a single photon of wavelength slightly greater than half that of the original two photons (Figure 1.21).

For two-photon excitation (TPE) to take place, a high photon flux density is required. In order to achieve this, sharp spatial focussing and temporal confinement of the excitation beam are required. Diaspro and Sheppard [162] provide a clear and accessible discussion of the requirements to make TPE a viable imaging modality, and forms a basis for the rest of this subsection.

Most treatments of TPE assume that the probability of a molecule undergoing two-photon absorption is proportional to the likelihood of finding two photons within the volume occupied by the molecule simultaneously. Diaspro and Sheppard [162] show that the intensity, I, of a laser beam passing through a cubic molecular volume of side length s containing a mean of m photons at any specific time can be expressed as follows:

$$I = \frac{mhc^2}{\lambda s^3} \tag{1.99}$$

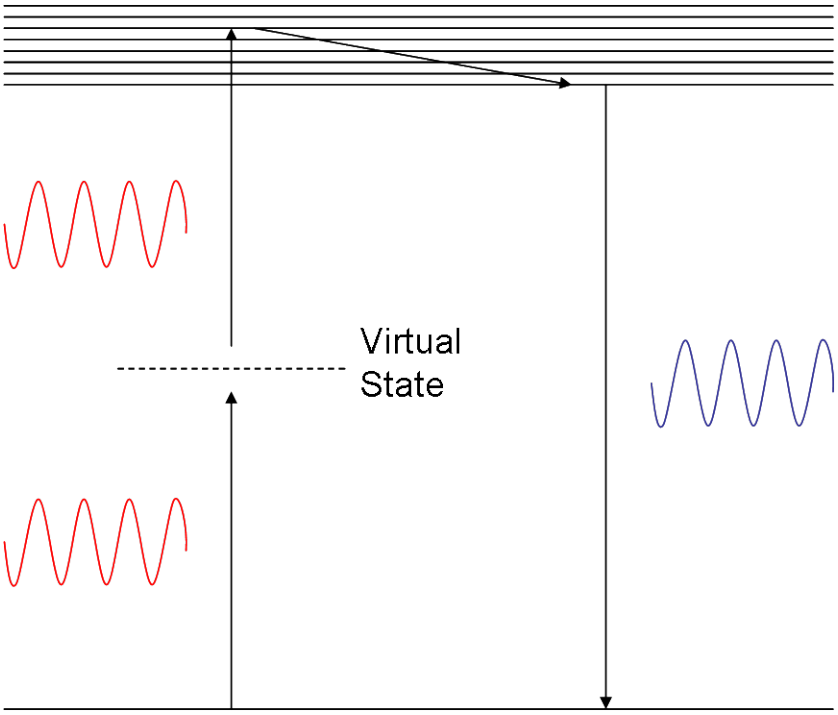

Figure 1.21: Energy diagram describing two-photon fluorescence. Two infra red photons excite an electron into a real energy state, which then thermally relaxes before de-exciting and emitting a visible wavelength photon.

where $h = 6.6 \times 10^{-34}$ Js is Planck's constant and $c = 3 \times 10^{8}$ ms^{-1} is the speed of light. The Poisson distribution defines the probability p_2 of two photons being present within the molecular volume is related to m by the following relation:

$$p_2 = \frac{1}{2} m^2 e^{-m} \tag{1.100}$$

and as m is typically small, the exponential can be expanded and approximated by the first term, 1, resulting in the simple relation:

$$p_2 = \frac{1}{2} m^2 \propto \Upsilon I^2 \tag{1.101}$$

where Υ is a scaling factor based on Equation 1.99. The fact that the probability of TPE scales with the square of signal intensity is a key result, and one which is vital for using it as a viable imaging modality, as standard single photon imaging scales linearly with intensity.

The input power required to observe sufficient amounts of TPE to construct an image are of the order of gigawatts (10^9 W) which, from a conventional continuous wave (CW) laser, is impractical due to sample damage. Instead, pulsed lasers are used that deliver high peak power whilst maintaining significantly lower average power, which is the cause

of sample damage. The excitation efficiency of a pulsed laser compared to a CW laser of the same average power will be greater by a factor of:

$$(\tau_p f_p)^{-\frac{1}{2}} \tag{1.102}$$

where τ_p is the pulse width (s) and f_p is the pulse repetition rate. For a 10 fs pulsed laser with a repetition rate of 100 MHz, the TPE excitation will be 1000 times greater than that of a CW laser. A pulsed laser needs a pulse repetition time significantly longer than the relaxation time of the fluorophore being excited (typically nanoseconds), so typically the time between pulses is around 10^{-8} s. The probability n_a that a fluorophore will undergo TPE during a single pulse is commonly approximated as being:

$$n_a \propto \frac{\delta_2 P_{avg}^2}{\tau_p f_p^2} \left(\frac{NA^2}{2\hbar c\lambda}\right)^2 \tag{1.103}$$

where δ_2 is the two-photon interaction cross-section, P_{avg} is the time-averaged laser power, NA is the numerical aperture of the objective, and λ is the laser light wavelength. The interaction cross-section is a measure of the inherent tendency of a fluorophore to undergo TPE and is independent of the single photon cross section, δ_1. The numerical aperture is a measure of the range of angles over which the objective can accept and emit light and is related to the focal volume of the laser.

Because of the high intensities required for TPE, the excitation region is restricted to a very small volume (less than 1 fl) around the focal point, Figure 1.22. This is due to the excitation power decreasing quadratically with distance from the focal point, inferring from Equation 1.101 that TPE will decrease with the fourth power. This means that photobleaching and photodamage are limited to the focal region leaving the surrounding areas unaffected. The small excitation volume also results in a significant reduction in background over standard flurorescence imaging and provides resolution close to that of confocal microscopy without the need for a pinhole.

Infra-red (IR) excitation light is used as it provides increased depth penetration into a sample due to reduced scattering. It does, however, also have the effect of reducing the spatial resolution. The use of IR wavelength light also reduces damage to the sample.

1.4.2 Two Photon Fluorescence Microscopy in Biomaterials

When light enters a material, it can interact with molecules. These molecules are referred to as chromophores, and are given the name as they are chemical compounds which interact with light and contribute to the material's colour. Chromophores can be categorised

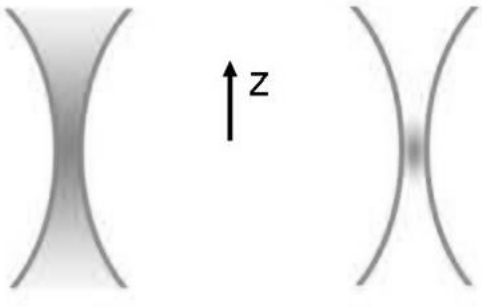

Figure 1.22: The TPE excitation volume (right) is significantly smaller than that of linear excitation (left) due to the fourth order drop in TPE with distance from the focal point.

into three types: absorbers, scatterers and fluorophores [163]. An absorber absorbs light but does not fluoresce, a scatterer will change the incident light direction but conserve its energy, and a fluorophore absorbs light and subsequently fluorescences. Chromophores act over a specific range of frequencies dictated by their energy level structure.

Biological materials contain a wealth of different chromophores. Typically in biological materials it is possible to resolve fluorescence from flurophores excited by visible light to a depth of $0.5\,\mathrm{mm} - 1\,\mathrm{mm}$. Detail can not be resolved beyond this depth due to scattering, which occurs at interfaces between materials of different refractive index and is particularly abundant in biological tissue due to its heterogeneity. Absorption bands for most proteins are found mainly at UV wavelengths and need to be avoided when selecting a frequency to perform fluorescence microscopy, as absorption can lead to heating and denaturation. The endogenous fluorophores are relatively weak in comparison with their exogenous counterparts, however confocal and multiphoton microscopy are powerful enough now to provide micrometer scale contrast at depths of hundreds of microns without the use of exogenous fluorophores [164]. The interaction cross-sections of individual fluorophores are measured in units of Göppert-Mayers, $1\mathrm{GM} = 10^{-58}\,\mathrm{m}^4\mathrm{s}$. As an example, fluorescin, a typical exogenous fluorophore, has a TPF cross-section of 34 GM at its excitation peak of 760 nm [162] whereas nicotinamide adenide dinucleotide (NAD(P)H - an endogenous fluorophore present within mitochondria) has a TPF cross-section peak of 0.01 GM at 700 nm. Many endogenous fluorophores are well characterised *in vitro* but their relative abundance and microscopic distribution are not well understood *in vivo*. The ability to isolate spectroscopic signal from femtolitre volumes allows for better categorization of, and differentiation between, the various fluorophores in a sample.

The most commonly studied endogenous fluorophores are tryptophan, NAD(P)H, flavoproteins, collagen and elastin. The first three have TPE maxima under 700 nm [164], and the last two are components of the ECM. Most endogenous TPF cross sections peak at wavelengths of between 700 nm and 750 nm and thus multiphoton imaging is more dam-

aging at these wavelengths. At the wavelength of 800 nm used in the work in Chapter 5, NAD(P)H, flavoproteins and elastin will undergo TPE. Of particular interest in this project is the behaviour of the elastin network in AC, which was first imaged using TPF by Yeh et al. [68], and then extensively investigated by Mansfield et al. [66].

1.5 Overview of Thesis

The work described in the chapters that follow combines theoretical work with experimental measurements. Chapter 2 describes the experimental preparation and methods used in the results chapters. Chapter 3 is the first results chapter and focuses on determining the mechanical properties of the individual layers in cartilage defined by the collagen orientation. To achieve this, previous experimental data [28] that related applied unconfined load to the deflection of layer boundaries was modelled using different assumptions about cartilage heterogeneity (homogeneous isotropy, layered isotropy and layered transverse isotropy). It was found that the layered transverse isotropic model could match the data from the experiment whilst preventing peaks due to interfacial shear at boundaries. An insufficient number of degrees of freedom in the experiment meant that a definite set of layered transverse isotropic mechanical parameters could not be defined for the sample, and so a set of experiments were devised to determine them.

Chapter 4 describes the results of a series of tensile tests of cartilage slices designed to determine the tensile mechanical properties of each layer. Mechanical stiffnesses were compared to images taken using polarised light microscopy as well as the split line direction, to determine the degree of anisotropy in-plane with the articular surface. It was found that the tensile modulus decreased as expected with depth, however there was considerable spread in the calculated stiffnesses, as well as variation in the stress-strain behaviour, which could not be fully interpreted using polarised light microscopy. In order to investigate further the effect of microstructure on the mechanical behaviour of articular cartilage in tension, the experiments detailed in Chapter 5 involved loading samples whilst simultaneously imaging using two photon fluorescence. The results showed that the strain observed at the level of individual elastin fibres varied considerably when compared with the larger scale strain averaged across 250 μm image stacks. The elastin fibre network was investigated both in its own right, and as a means of determining strains. Finally Chapter 6 summarises the findings of the thesis and presents them as a set of conclusions, with potential avenues for future research.

Chapter 2

Materials and Methods

This chapter aims to describe the methods by which the theoetiecal and experimental results in Chapters 3, 4 and 5 were obtained. Chapters 4 and 5 involve experimentation with samples of articular cartilage (AC), and so this chapter begins by explaining the method by which samples are collected and prepared. It then introduces the tensile loading rig, which is used in Chapter 4 to find the tensile modulus of strips of AC, and in Chapter 5 to apply strain whilst simultaneously imaging the AC using two photon fluorescence (TPF). TPF images are obtained using the multiphoton microscope which is described in the following section. The last section of this chapter briefly describes the equipment and software used to create the layered FE model used in Chapter 3.

2.1 Preparation of Cartilage Samples

All AC samples used in experiments in this thesis were obtained from the equine metacarpophalangeal (MCP) joint. Legs were collected from Stillman's abattoir (Taunton, UK) from horses aged 2 and under for imaging and 10 and under for tensile testing. Legs were removed from the carpometacarpal (knee) joint and stored in a sealed bag in a cool box during transport back to the laboratory. Dissections were performed within two hours of death, and samples were taken from legs which exhibited minimal lesions.

The goal of dissection is to expose the three articular surfaces of the MCP joint without causing damage. To achieve this the leg is skinned and portions of the various ligaments supporting the joint are removed using a scalpel. The resultingly weakened joint can then be opened by delicately cutting along the palmar side of the metacarpal. Once opened, unloading the joint brings the metacarpal away from the sessamoids and proximal phalanx, allowing it to be cut free. Dissection of the rest of the joint can then be simply

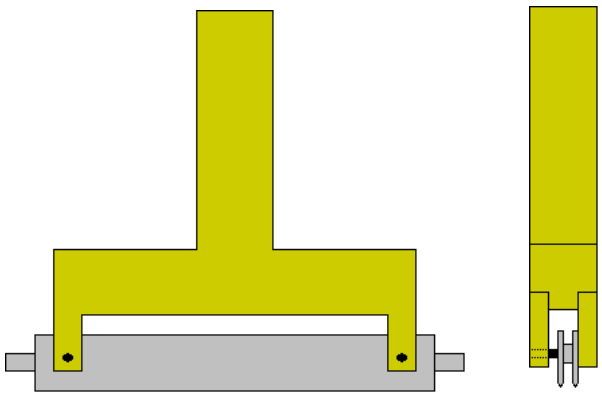

Figure 2.1: Vertical cutter viewed from the front (left) and side (right). The brass housing contains two razor blades separated with a steel spacer, resulting in a gap of approximately 700 μm between the sharp edges of the two blades. The blades and spacer are held tightly together using grub screws. The sample to be cut is rested upon a block of silicone rubber which is stiff enough to provide adequate support, whilst being compliant enough to cut through without blunting the razor blades.

performed by eye. Once the joint has been opened, the articular surfaces are regularly doused or submerged in 0.15 M NaCl at pH 7.2 to prevent dehydration.

Samples of AC are removed from the underlying bone using a scalpel blade carefully inserted at the interface. In regions where effective removal is hindered by the topology of the joint (such as the saggital groove of the proximal phalanx), a saggital section of the AC and underlying bone is removed using a hacksaw. The explanted AC is then cut into thin strips using a vertical cutter described in Figure 2.1. This method of cutting provides clean, parallel edges which are essential for obtaining accurate tensile test results. The strips are then observed saggitally using a light microscope to check for uniform thickness. At this stage the strips are ready to be mounted in the loading rig for multiphoton imaging.

Preparation of samples for the tensile testing work requires that slices be taken from the three different layers of the AC described in the previous chapter. The tangential (Ta) layer of AC is only 50 μm thick in some regions, so obtaining slices from this region is a challenging task. To obtain thin slices of AC, a freezing microtome (Cryocut E, Leica) fitted with a tungsten carbide blade (D6907 Nussloch, Leica) is used. The sample is mounted in a ball jointed chuck (see Figure 2.2) allowing adjustment of the cutting plane relative to the sample after embedding.

AC has a tendency to curl when explanted. This, coupled with other small variations in the articular surface makes obtaining samples from the Ta layer impossible without first manually flattening the surface. The common method of removing AC until a flat surface remains is clearly not applicable here, so a technique was developed which involved part freezing the embedding compound (Cryo-M-Bed, Bright) on the chuck before placing the sample and a microscope slide on top. The weight of the microscope slide causes the

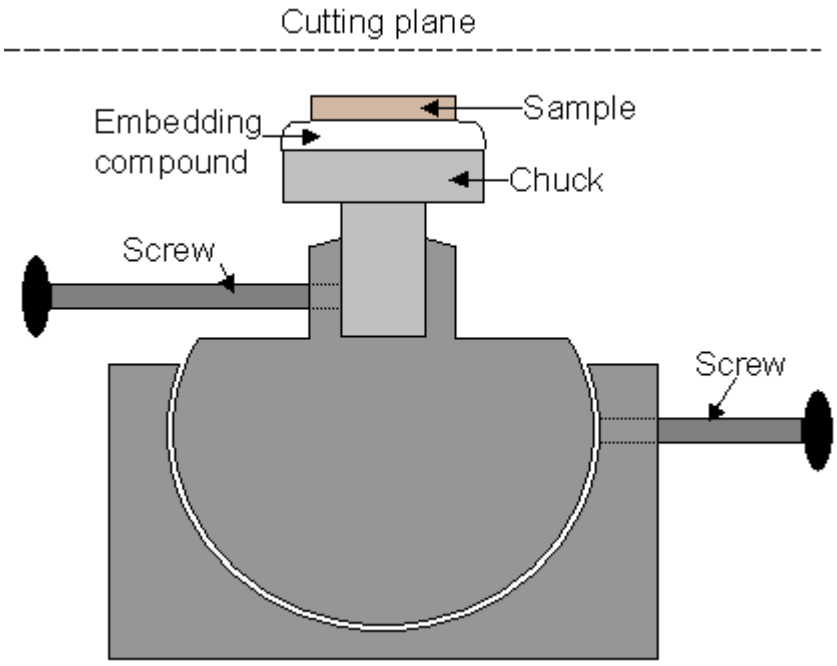

Figure 2.2: The ball and socket joint of the microtome chuck housing.

surface of the sample to flatten, and the stiffness of the part-frozen embedding compound prevents the sample from being engulfed. A cylindrical support slightly taller than the chuck prevents the microscope slide from tipping or falling off as the sample freezes in place. Once the sample has frozen, the microscope slide is removed and the sample exposed with a perfectly flat surface. The sample is then inserted into the socket of the sliding ratchet mechanism and brought close to the cutting blade, and fine adjustments in the angle of the chuck, combined with observations in the alignment using a dentists mirror are used to ensure the surface is in line with the cutting plane (Figure 2.2).

Once satisfied that the articular surface is in line with the cutting plane, the chuck is ratcheted towards the blade in 20 μm increments until a surface slice is obtained. The first slice is discarded as it is of unknown and irregular thickness, and the second slice, and any subsequent slices, are placed on a microscope slide with a droplet of saline and imaged using a polarised light microscope. The purpose of this imaging is firstly to determine the integrity and suitability of the sample for tensile testing, and secondly to determine the arrangement of collagen. Transitional (Tr) and radial (R) slices are then obtained by cutting off a number of waste slices before using the manual adjuster to take a thicker slice. Thicker slices can be used as the Tr and R layers are considerably thicker than the Ta layer, and thicker samples are preferable to work with as they are less susceptible to surface tension and require larger forces to deform. More precise stress data can therefore be obtained.

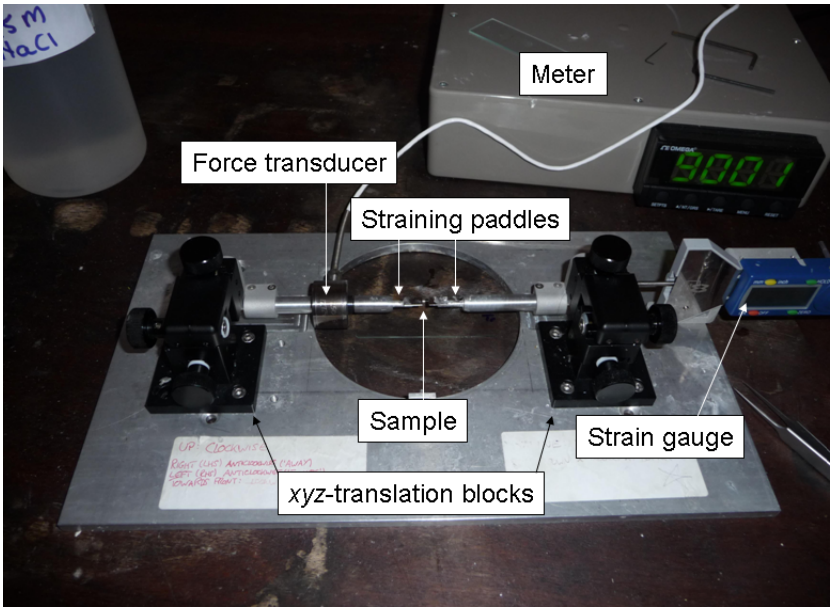

Figure 2.3: Tensile loading rig in the tensile test configuration with the digital control box showing a reading of over 9000 as an illustration.

2.2 Tensile Loading Rig

The tensile loading rig was custom built for the purpose of quantitative tensile testing of explanted soft tissue whilst imaging on the multiphoton microscope. In both sets of experiments, samples of AC are attached using glue (cyanoacrylate super glue, Henkel Loctite Ltd.) to specially designed steel paddles which are then moved apart to induce a tensile strain. The basic unit comprises a base plate with xyz-translation blocks.

2.2.1 Tensile Test Configuration

The components used in the tensile test configuration (Figure 2.3) are all arranged linearly to prevent moments. The arm on the left side is attached to a force transducer (RDP Electronics Ltd. Model 31) which has a full scale range of 2.5 N and is sensitive to changes of 10^{-4} N when connected to the DP25-S Strain Meter (Omega). The transducer is directly connected to an arm which holds the left paddle. The right arm connects directly to the right paddle, and a strain gauge (Moore & Wright) sensitive to 10 μm is attached to the base plate which measures the displacement of the right arm in the direction of strain.

Hydration is a major issue when performing experiments with thin strips of cartilage. At room temperature, a 20 μm slice of AC suspended from a pair of forceps dries and shrivels noticeably in seconds. This presents a problem when attempting to stick a sample to the two paddles, as the presence of saline on the sample causes the glue to creep, resulting in

deposits on the sample between the two paddles, and thus inaccurate tensile test results. This problem is resolved by conducting the entire experiment in a cold room which is maintained at 3 °C and high humidity, where samples do not dehydrate significantly over the timescales required for superglue to harden.

The method by which thin samples are stuck to the paddles is complicated by the internal forces causing some samples to roll up on themselves. To prevent this, the paddles are coated in glue and the sample transfered to a dry coverslip. One end of the sample is then slid from the edge of the coverslip onto a paddle where it is held in place with the forceps, while the coverslip is pulled over to the other paddle, which causes the sample to slide from the coverslip onto the paddle. The sample is then left for 10 minutes after which a second coating of glue is administered. After a further 20 minutes the glue is checked and if fully dry a droplet of saline is placed across the paddles and sample for hydration during the experiment. If the paddles are too far apart for a droplet to rest between, an end of a cocktail stick is rested across to act as an extra surface for the droplet to cling to. Experiments show that the presence of the cocktail stick does not contribute significantly to the measured force.

2.2.2 Multiphoton Imaging Configuration

The multiphoton configuration (Figure 2.4a) was designed to allow high resolution imaging of the microstructure of AC with the intention of investigating the distribution of strain at a microscopic level. It includes a PTFE dish for preventing saline from coming into contact with delicate optical equipment. The centre of the dish is raised and has a hole for housing the microscope objective and to allow laser illumination of the AC. The arms of the rig are designed to reach down into the dish to allow samples to be as close to the objective as possible. The paddles face downwards and so the sample must be stuck down prior to the dish being inserted.

The objective (UPlanS Apo, Olympus UK) has a 60× magnification and a numerical aperture of 1.2 and is designed for pure water immersion. As samples contain saline, a coverslip is therefore required between the objective and sample. Round coverslips (13 mm round glass, Fisher Scientific) are used which have radii slightly greater than the hole, and a thickness of approximately 50 μm. The coverslip is sealed over the hole using high vacuum grease (Dow Corning). The objective has a working distance of 210 μm leaving a gap of 160 μm, which includes the sample-coverslip distance, the coverslip-objective distance and the depth into the sample at which the image is being taken. Care must therefore be taken to avoid damage to the objective.

In order to achieve these precise alignments without causing damaging contact between

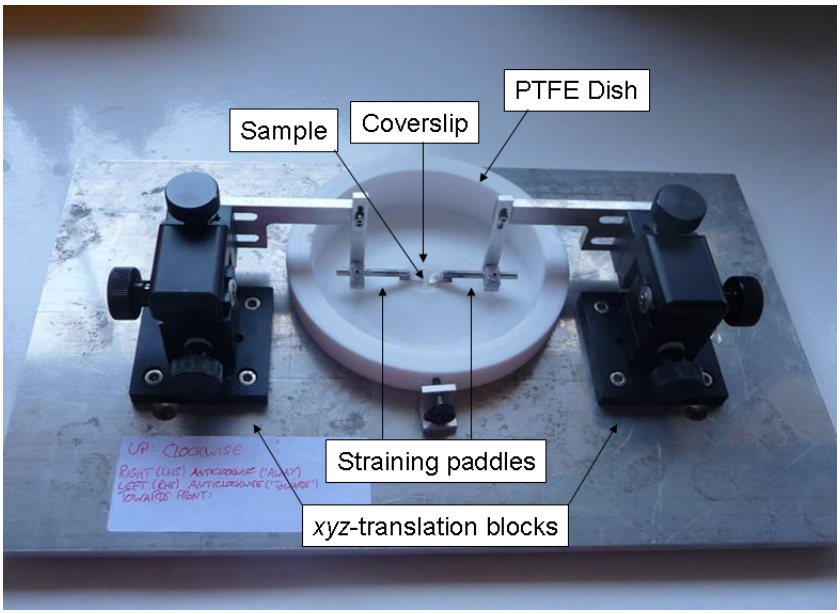

(a) The tensile loading rig separate from the multiphoton microscope.

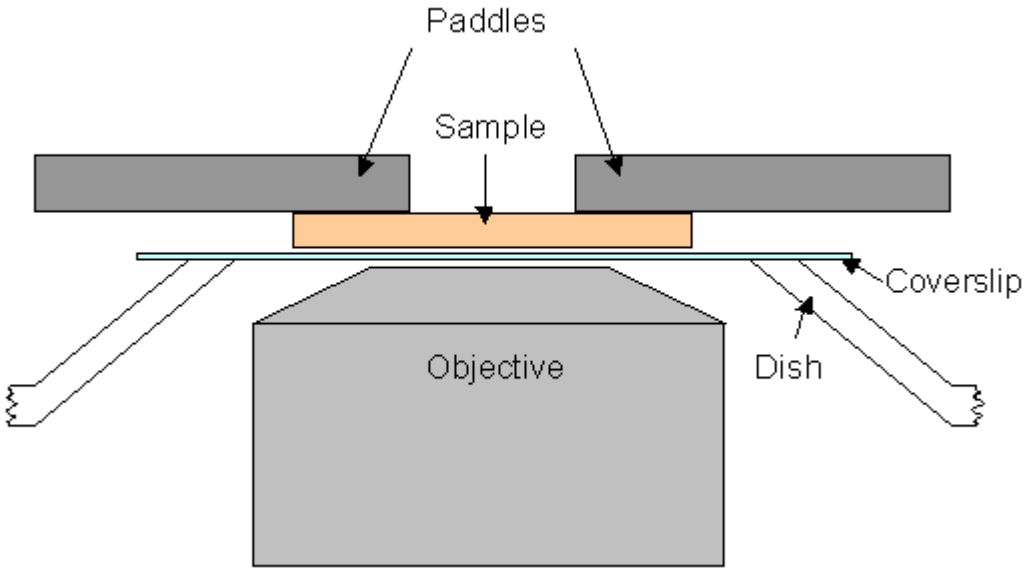

(b) Schematic of the method of imaging whilst simultaneously applying strain.

Figure 2.4: Tensile loading rig in the multiphoton imaging configuration.

the objective and coverslip, the sample is lowered towards the coverslip prior to the rig being placed on the optical table. The outer lip of the dish prevents viewing of the sample from the plane of the coverslip, so instead the sample is lowered until deflection is seen in the reflection of the coverslip (when the sample makes contact). The rig is then placed on the optical table and aligned by eye with the objective. Fortunately the excitation wavelength for elastin TPF is visible, so the laser can be used to accurately align the rig in the plane of the objective. Once aligned, the objective is raised in 50 μm increments towards the coverslip until a signal is obtained from the sample.

2.3 Multiphoton Microscope

The multiphoton microscope is a modified confocal microscope (FluoView IX71 and FV300, Olympus) and which has been modified for multiphoton microscopy. The microscope is set up to perform two photon fluorescence (TPF), second harmonic generation (SHG), coherent anti-stokes Raman scattering (CARS), spontaneous Raman spectroscopy (SRS), and other multiphoton imaging modalities in both the forward and back scattered directions. Figure 2.5 describes the system for TPF imaging in the epi direction which is used for imaging the microstructure of AC under load in Chapter 5. All optical equipment, unless otherwise stated, is a product of Thorlabs Ltd.

TPF is excited using the 800 nm output of a Ti:sapphire laser (Mira 900-D, Coherent Inc.) pumped by a 532 nm solid state laser (Verdi V10, Coherent inc.). The laser pulses with a repetition rate of 76 MHz and pulse width of 100 fs in the microscope. The signal is separated from the laser fundamental using a long pass dichroic mirror (670dcxr, Chroma Technologies, part 7 in 2.5b) and then passes through two band pass filters (F70-500-3-PFU and CG-BG-39, CVI Melles Griot) centred at 500 nm with a full width half maximum value of 70 nm. This separates TPF from SHG light and matches closely to the wavelength corresponding to the peak TPF cross section for elastin [165]. The signal is then focussed into a photomultiplier tube (Hamamatsu R3896).

Images are constructed by raster scanning the focal spot of the laser and building a 2D intensity plot from the signal received at the photomultiplier tube (PMT). Scanning is performed by a set of galvanometer mirrors in the scan unit. The shutter, galvanometer and PMT is controlled by computer via the FluoView version 5 software.

In order to quantify the microscopic distribution of strain using an imaging based technique, a series of images are taken of the same region at different states of strain. Stacks of xy images separated by a distance of 1 μm in z are used to find the positions of cells and elastin fibres, and their relative movement under strain. It is not possible to continuously image a sample using TPF due to photobleaching, and the small field of view coupled

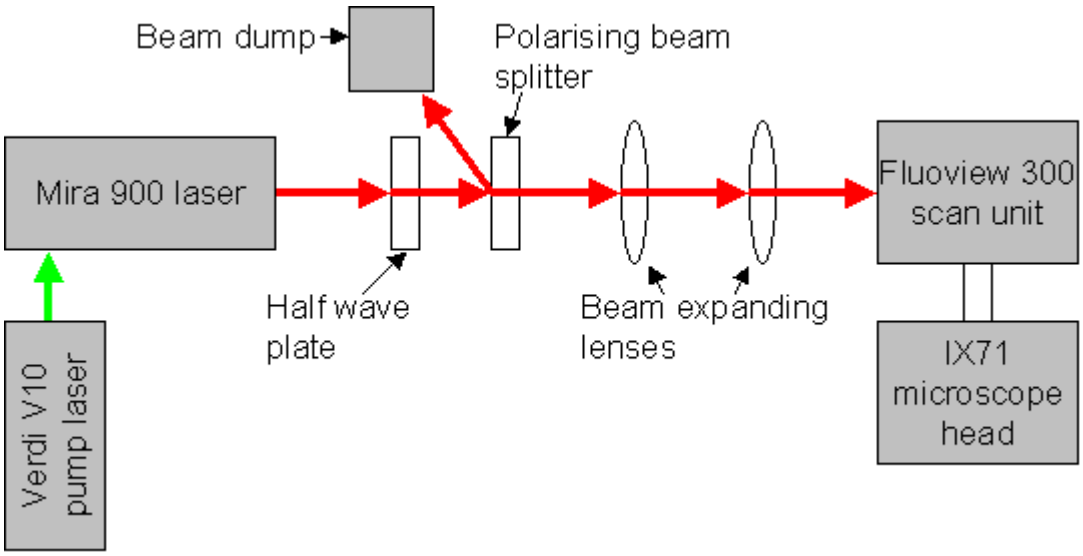

(a) Schematic of the equipment used for TPF imaging. The true optical path includes several mirrors for switching between imaging modalities which are not included in this diagram.

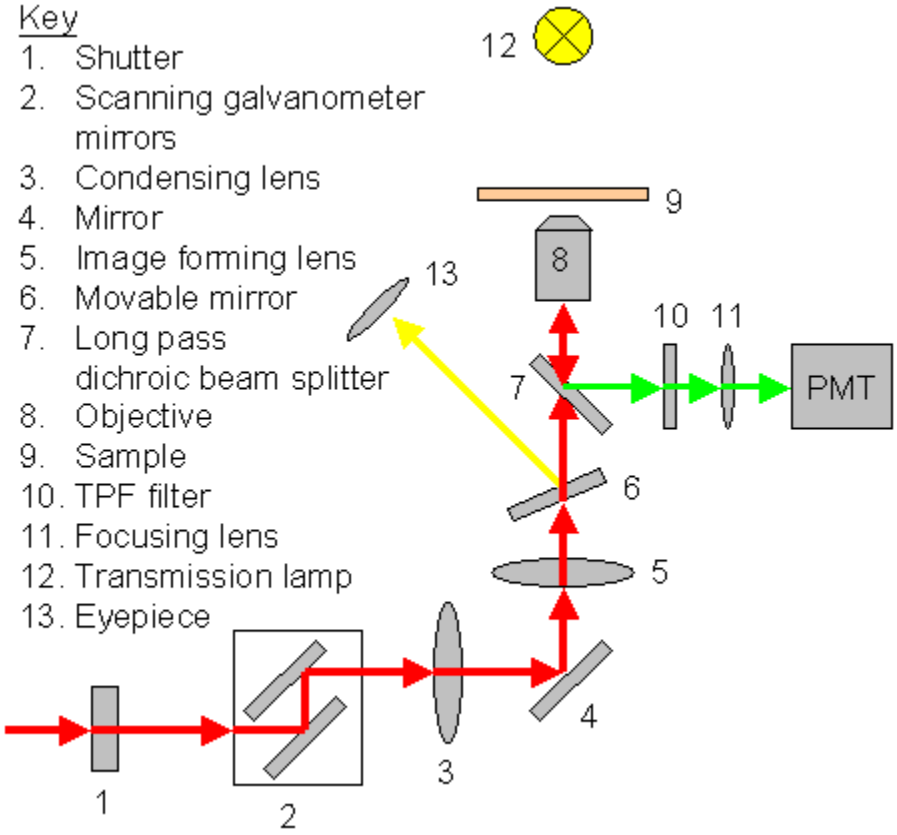

(b) Schematic of the optical equipment inside the scan unit and microscope head. Only equipment needed for TPF is shown.

Figure 2.5: Multiphoton microscopy equipment used for TPF imaging.

with comparatively large deformations associated with applying strain makes returning to a region previously imaged difficult. A solution to this problem involves focussing the beam into a narrow region to bleach a marker (Figure 2.6) which can be found more easily after a sample has been strained. The amount of bleaching during normal TPF imaging is proportional to the square of the intensity of the incident beam, so a balance was found between the clarity of images and the amount of bleaching. This allowed the imaging of the brighter elastin fibres to a depth of around 70 μm whilst minimising bleaching sufficiently to allow stacks of images to be taken from the same region at three different states of strain. The optimum laser power at the objective was found to be between 20 mW and 30 mW, samples were imaged at strains of 0 %, 10 % and 20 % using the Kalman $\times 3$ noise filter, which repeats the scan three times at each depth to reduce noise.

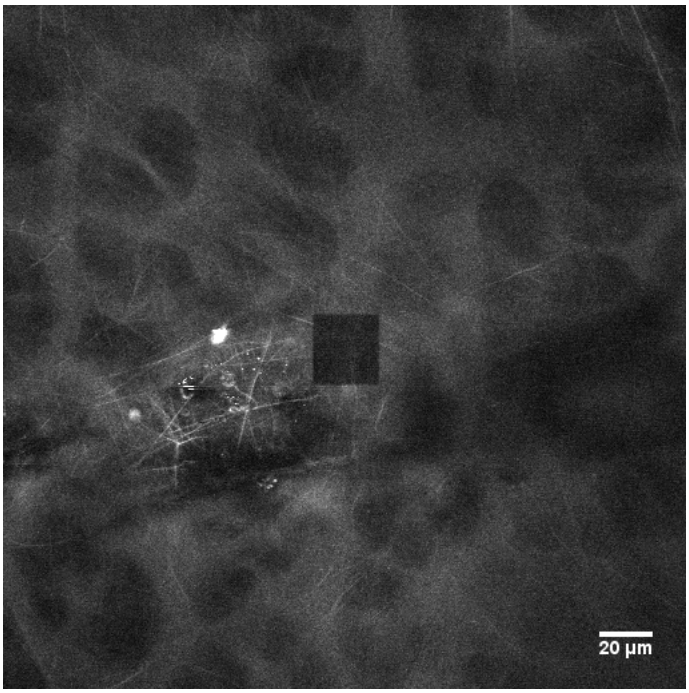

Figure 2.6: TPF image illustrating a photobleached square used as a marker when applying tensile strains.

2.4 Finite Element Analysis

Finite element analysis is used in Chapter 3 to create material models of AC under load based on experimental data [28]. This work considers the anisotropy of AC by introducing material properties reflecting the contribution from the orientation of collagen. The model solves a backwards problem with the input variables of applied force and the resulting displacement of the layer boundaries, from which it calculates iteratively the material properties given predefined assumptions of mechanical anisotropy.

2.4.1 Software and Hardware

Abaqus v6.7-1 was used to perform all the modeling work, as it has a well-developed elastic modeling module and in-house expertise was readily available. The Abaqus GUI used in this investigation is Abaqus/CAE which provides integrated preprocessing and postprocessing environment for FE analyses.

The computer used to run the models was a Dell OptiPlex 755 box with an Intel Core2 Duo CPU E6850 @ 3.00 GHz processor, and 8 GB of RAM running Windows Vista 64bit edition. The linear elastic model contained 140,880 linear brick elements (this number is dictated by the geometry and desired resolution, detailed in the next chapter) and 1 calculation step and took approximately 3 hours to complete on this system. MATLAB v7.5.0 (R2007b) was used for postprocessing and data analysis.

Chapter 3

Layered FE Model of the Steady-State Mechanical Response to Load

The transient response of articular cartilage (AC) to compressive loads has been described by complex multicomponent models (see Section 1.2.2). However, the steady-state behaviour is determined by the collagen network which is heterogeneous through the depth of the tissue, a characteristic which is omitted from most theoretical models. Experimental data are now available on the local responses of the network to compressive loads and the aim of this study was to develop minimal models capable of simulating this behaviour. A series of finite element models (FEMs) of AC under load were developed of increasing complexity, assuming the AC was i) completely homogeneous, ii) layered and isotropic and iii) layered and anisotropic. The geometry of the layered cartilage model was based on the recent experimental data. It is shown that a layered transversely isotropic elastic model is at least required to accurately recreate the experimental data. Stress distributions within the models are also determined.

3.1 Introduction and Preliminary Work

The work presented in this chapter employs FE modeling techniques, described in Section 1.3, to investigate the mechanical complexity of articular cartilage.

3.1.1 *D*-Matrix Calculation

The theory of linear elasticity, described in Section 1.2.2.1 is used to calculate the *D*-matrix which is used by Abaqus for solving problems involving elastic force and deformation. Although linear elasticity is an approximation of the deformation behaviour of continuum solids, it is generally accepted in the literature that up to strains of 20%, the relationship between stress and strain is linear [112]. In the orthotropic case, this matrix, Equation 3.1, has nine linearly independent material parameters, summarised in Equation 3.2.

$$D_{ijkl} = \begin{pmatrix} D_{1111} & D_{1122} & D_{1133} & 0 & 0 & 0 \\ & D_{2222} & D_{2233} & 0 & 0 & 0 \\ & & D_{3333} & 0 & 0 & 0 \\ & & & D_{1212} & 0 & 0 \\ & sym & & & D_{1313} & 0 \\ & & & & & D_{2323} \end{pmatrix} \tag{3.1}$$

$$\begin{aligned} D_{1111} &= E_1(1-\nu_{23}\nu_{32})/\Upsilon \\ D_{1122} &= E_2(\nu_{12}-\nu_{13}\nu_{32})/\Upsilon \\ D_{1133} &= E_3(\nu_{13}-\nu_{23}\nu_{12})/\Upsilon \\ D_{2222} &= E_2(1-\nu_{13}\nu_{31})/\Upsilon \\ D_{2233} &= E_3(\nu_{23}-\nu_{21}\nu_{13})/\Upsilon \\ D_{3333} &= E_3(1-\nu_{21}\nu_{12})/\Upsilon \\ D_{1212} &= \frac{\sqrt{E_1E_2}}{2(1+\sqrt{\nu_{12}\nu_{21}}} \\ D_{1313} &= \frac{\sqrt{E_1E_3}}{2(1+\sqrt{\nu_{13}\nu_{31}}} \\ D_{2323} &= \frac{\sqrt{E_2E_3}}{2(1+\sqrt{\nu_{23}\nu_{32}}} \end{aligned} \tag{3.2}$$

Where Υ is a function of Poisson's ratios:

$$\Upsilon = 1 - (\nu_{12}\nu_{21} + \nu_{23}\nu_{32} + \nu_{13}\nu_{31}) - (\nu_{12}\nu_{23}\nu_{31} + \nu_{21}\nu_{32}\nu_{13}) \tag{3.3}$$

These material coefficients are calculated with a macro for each set of material parameters used in this work (Table 3.2). Simple homogeneous isotropic models were run using parameters from the orthotropic material macro as a means of verification. The macro also checks that strain-energy density is positive, which has to be the case for a material

to viably exist. Homogeneous, isotropic materials always obey this constraint, but the more complex transverse isotropic materials used later in this chapter do not. Transverse isotropy is a special case of orthotropy in which a material is isotropic within a given plane. If the plane of isotropy lies on two predefined orthonormal material axes, the axes in question are denoted p and the transverse axis is denoted t. The criteria for verifying positivity of the strain-energy density are as follows:

$$\begin{aligned} E_p &> 0 \\ E_t &> 0 \\ G_p &> 0 \\ G_t &> 0 \\ |\nu_{pp}| &< 1 \\ |\nu_{pt}| &< \sqrt{\frac{E_p}{E_t}} \\ |\nu_{tp}| &< \sqrt{\frac{E_t}{E_p}} \\ \Upsilon &> 0 \end{aligned}$$

If the inputted elastic parameters fulfill the above criteria then the D-matrix is outputted in a form which is readily entered into Abaqus.

3.2 Experimental Data

The geometry and mechanical properties of the model are based on small angle X-ray scattering (SAXS) data gathered by Moger et al. [7, 28]. In this work, saggital sections of cartilage and underlying bone were excised from the condyles from the equine metacarpophalangeal joint (Figure 4.5 shows such a section) and normally loaded using a stepper motor and force transducer. Collagen fibre orientation was determined at different states of stress using SAXS. The samples were on average 1.8 mm thick, and the load was applied to the articular surface using a flat indenter 6 mm in the plane of the section, and 2 mm wide. The curvature of the surface of the AC was measured and accounted for when calculating the stress applied to the surface.

SAXS is a technique for measuring structural detail in materials at the nanometer scale. It involves measuring the scattering angles of incident monochromatic X-rays. In cartilage, the regular D-spacing of $\sim 670\,\mathring{\text{A}}$ in collagen fibrils (see Figure 1.1) gives rise to diffraction maxima in the shape of a ring, which can be observed using a charge coupled device (CCD)

based detector. In this experiment, the peak at 223 Å was used as it provided the clearest data. Collagen orientation was extrapolated from the intensity at different angles on the diffraction ring, and data sets were taken at intervals of increasing depth underneath the centre of the loading platen.

The application of load in this geometry has some notable limitations. Firstly, the amount of friction between the loading platen articular surface is unknown, and although the SAXS data is taken from the saggital midpoint of the indenter there will be contributions from the full thickness of the sample, which may be experiencing interfacial shear. Secondly, the depth resolution (approximately 25 μm) means only 2-4 points are recorded from the tangential zone, meaning calculation of layer thickness is heavily reliant upon interpolation. Lastly, the variation in the curvature across samples makes stress calculation difficult and inaccurate.

3.2.1 Results

Figure 3.1 shows the measured fibre orientation data derived from SAXS for cartilage which is unloaded, and at two states of strain. The internal strain data from the different layers in the unloaded case (top) and the 59 kPa loaded case (bottom) are used as a basis for this work.

In order to create a layered FE model, the locations of the interfaces between layers must be known. The collagen fibre scattering intensity data is a measure of the concentration of fibres at a given orientation with respect to the articular surface. This was quantified for a particular sample using an algorithm that compared the spread of intensity at specific depth intervals with prescribed orientation conditions defining the boundaries between the three cartilaginous layers. These cartilaginous layers, described in Figures 1.2 and 3.1, are defined as tangential (Ta), transitional (Tr) and radial (R) and correspond to layers where the fibres are either parallel, randomly orientated, or radially aligned, respectively, to the articular surface. Boundaries B1, B2 and B3 mark the edges of these layers, and were calculated by sweeping through the orientation data starting at the articular surface, and prescribing tolerances to the ranges of collagen orientations as they vary with depth. The surface of the cartilage is B1, the deep boundary of the tangential layer is B2, and was defined as being the depth at which greater than 5 % of the total intensity lies outside the range of 0-40°, B3 marks the boundary between the Tr and R layers and was defined as the depth at which greater than 90% of the total intensity lies within the range of $70 - 110°$, and B4 marks the tidemark. With these conditions prescribed, the cartilage layer boundary locations were calculated, as shown by the white lines on Figure 3.1. Using the same conditions, the thicknesses of each layer were then calculated in the two

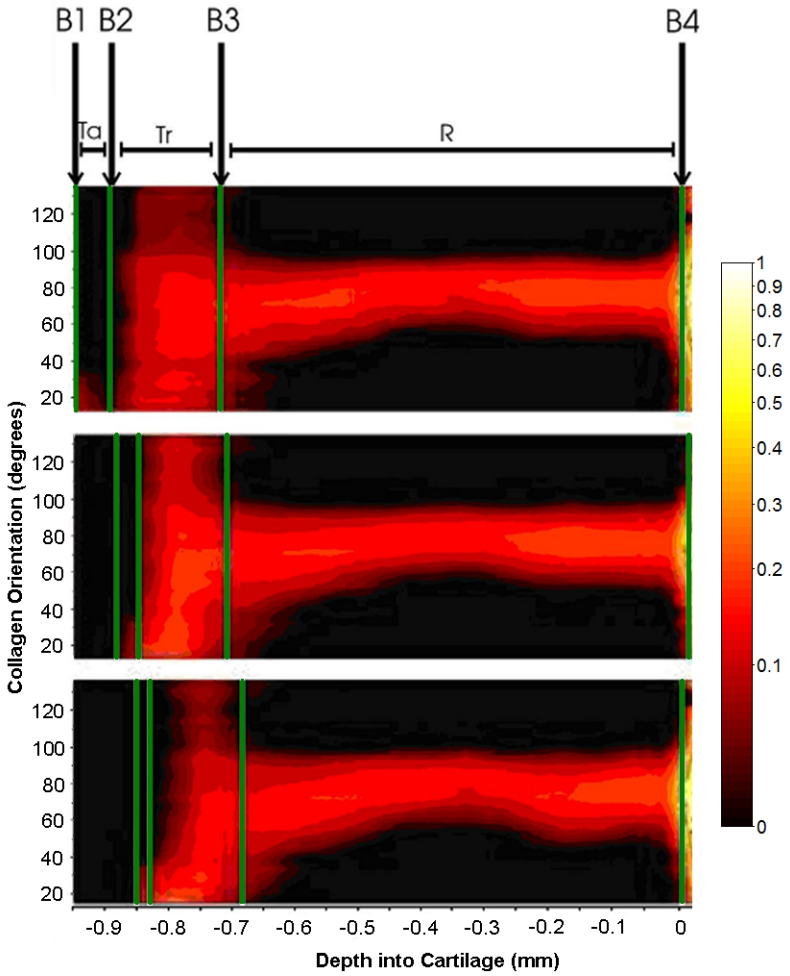

Figure 3.1: Two dimensional representation of collagen fibre orientation based on SAXS data from Moger et al. [28]. The x-axis represents the depth into the cartilage and the y-axis represents the measured fibre orientation relative to the articular surface. The boundaries between each layer are shown by the solid green line for applied stresses of 0 kPa (top), 26 kPa (middle) and 59 kPa (bottom). Each data set was taken after the stress had equilibrated. The scale is logarithmic and normalised to the highest measured signal (dark - low signal, light - high signal).

loaded cases, and hence the deformation and strain in each layer was determined. It is acknowledged that by defining a layer boundary arbitrarily in this way, changes in fibre orientation due to loading will result in these boundaries not remaining fixed to the same points in the material. To find the magnitude of this discrepancy, further work involving the comparison of collagen reorientation with direct measurements of normal strain under load is needed. This could be achieved by simultaneously comparing orientation change with movement of fiducial points on the ECM, using techniques such as chondrocyte nuclei labelling [107].

3.3 Model Design

3.3.1 Geometry

The layer boundaries calculated in the previous section are used as a basis for the geometry of the model. The thickness of each unloaded layer is detailed in Table 3.1. A 140,880 linear brick element model is used, incorporating 5 layers in a 3 D geometry.

The undeformed model is essentially a cuboid of size 5.95 mm by 4 mm by 3 mm in the x, y and z directions, respectively. The model incorporates a 0.95 mm thick cartilage layer upon 5 mm of bone. The model is designed to replicate the geometry described in the data in Figure 3.1, with the cartilage depth chosen to be the x-axis, and the tidemark chosen to be the plane $x = 0$ (see Figure 3.2). The surface of the model is the region of lowest x-value, with the region $x < 0$ representing the AC. The y and z directions are referred to as 'in plane' as they are parallel with the articular surface.

The model is sufficiently large in y and z that boundary effects such as edge sagging have negligible effect in the centre of the model where data is taken. This is shown in an investigation into the indenter size analysis in Section 3.3.5. The model has a large subchondral bone section which is much stiffer than the AC and is split into upper and lower sections. Two bone sections are used for meshing reasons, minimizing computation time without compromising accuracy. The upper bone section is meshed in such a way as to share nodes with the radial AC layer at boundary B3, and the lower bone section has a very coarse mesh. The bone sections together are necessarily by far the largest part of the model, this is to allow an encastre ('clamped') boundary condition (discussed in Section 3.3.2) to be used without affecting stress data in the cartilaginous region. Two bone sections are used so as to restrict resolution gradient-induced errors to the upper-lower bone interface, which is not of interest.

The cartilaginous layers in the model are meshed at a much finer resolution than the bone. Elements of size $5\,\mu$m $\times$ $100\,\mu$m $\times$ $100\,\mu$m are used in the Ta layer, and of size

Layer	Thickness (μm)
Tangential (Ta)	54
Transitional (Tr)	172
Radial (R)	724
Upper bone	500
Lower bone	4500

Table 3.1: Thickness of each layer in the 3D finite element model. The upper and lower bone thicknesses were chosen to mimic the experimental setup.

$10\,\mu$m $\times$ $100\,\mu$m $\times$ $100\,\mu$m in the Tr and R layers, respectively. Nodes are arranged much more closely together in the x-direction, as strain data in this direction is of the greatest interest, and of direct relevance to the experimental data. The Ta layer has a finer mesh than the rest of the model due to its thin nature, the greater strain it experiences, and its significance in pathology.

It should be noted that the geometry of the model is not intended to mimic that of a joint or of cartilage *in vivo*. The geometry has been designed to output accurate stress and strain data along the central x-axis, which can be compared directly with strain data calculated from experiment. Accuracy of stress and strain data will fall with distance from the central x-axis due to boundary effects at the y and z limits of the geometry.

3.3.2 Boundary Conditions

The boundary condition (BC) terminology used in this section is chosen to reflect that used in Abaqus. Three types of BC are used in this model. These include

- Encastre, or 'clamped'.
- Hard, rough surface-surface contact which disallows separation.
- Translational deformation, which involves moving sets of nodes through fixed distances.

The encastre boundary condition prevents any translational or rotational movement on the nodes it is applied to. The condition is applied to the bottom half of the lower bone section on the $y = 0$ and $y = 3$ planes to reflect the act of clamping the metacarpal in a vice, as was the case in the experiment [28]. The BC is only applied to the lower section of the bone. This is in part due to the fact that the actual bone used in the experiment was not clamped all the way to the cartilage, but more importantly this minimizes the effects of the encastre BC on the stress and strain data in the region of interest.

Surface-surface contact conditions control how two abutting parts interact and move relative to each other. As elastic deformation is the only phenomenon being modelled in

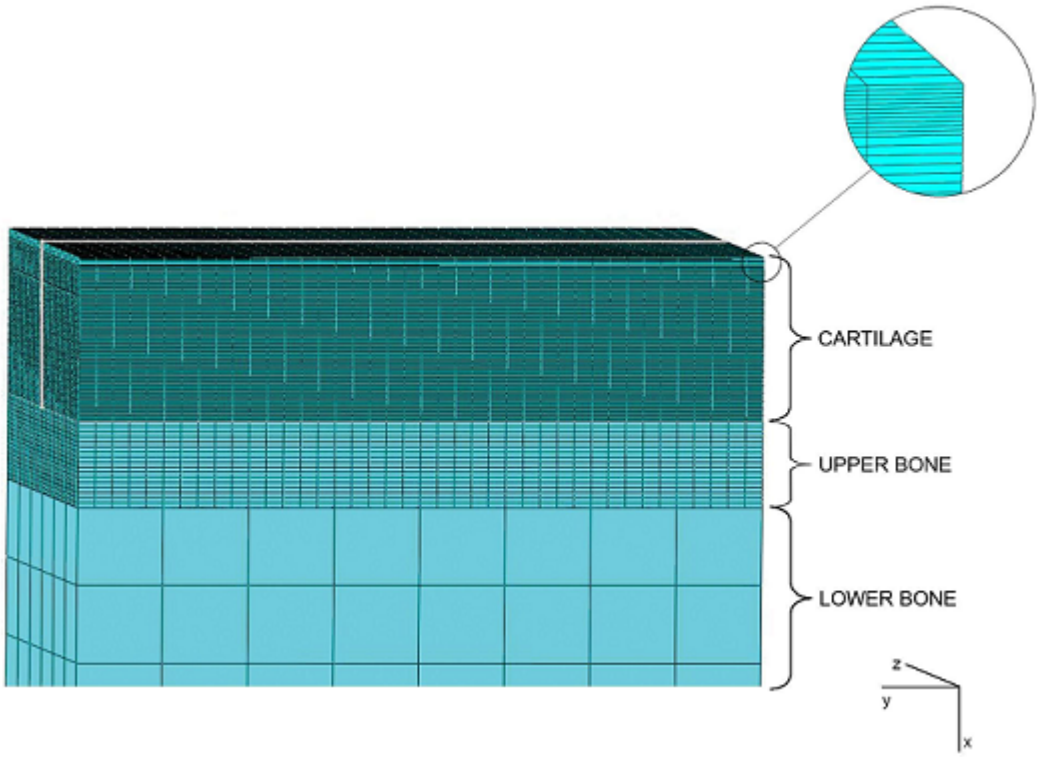

Figure 3.2: Finite element model of articular cartilage containing 154,484 nodes corresponding to 140,880 linear brick elements. The model consists of 5 layers defined in Table 3.1. The white line bisecting the top surface marks the plane on which stress data is collected (Figure 3.7). The model is 4 mm across in y.

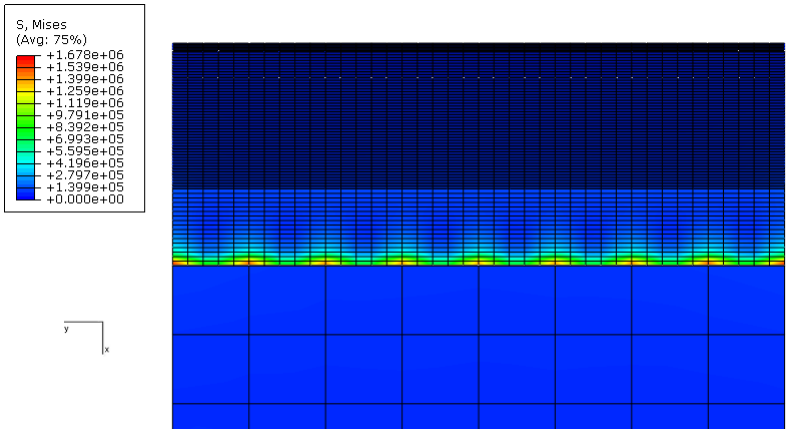

Figure 3.3: Anomalously high stress due to the mesh resolution step between the upper and lower bone layers. The colours plot von Mises stress (Equation 1.15) and the model is 4 mm across in y.

this case, the BC needs only to define how the nodes from the two parts sharing the same plane move under load. All surface-surface boundary conditions used in this model are defined as having 'hard' normal properties, and 'rough' transverse properties. The hard condition stipulates that no region of space can be occupied by both parts simultaneously (i.e. the parts can not move into each other). The rough condition stipulates that two abutting surfaces can not slide across each other. All surface-surface contact BCs lie on planes of constant x, so when two parts of identical y and z mesh resolution are connected with this type of BC, their nodes overlap exactly in space, and overlapping nodes are not allowed to part from each other. When parts of different mesh resolutions are adjoined with this type of BC, interpolation occurs between nodes, and their relative positions becomes fixed. In the case of the lower-upper bone interface, the very coarse nature of the lower bone part will lead to anomalous stress peaks around its associated nodes at the boundary, see Figure 3.3.

The surface-surface contact BC was verified by comparing a three layer model with a homogeneous model of identical geometry. When the three layers were meshed continuously, the two models deformed in exactly the same way under normal load. This verifies continuity of the stress and strain fields across the boundary.

The translational deformation BC is applied to the entire surface of the model ($x = -0.95$) and essentially involves translating the surface nodes in the negative x-direction. The translation can be performed in one step, due to the absence of transient factors in the model. A detailed description of the modelled deformation is included in the next subsection.

3.3.3 Deformation

The act of applying the load in experiment is replicated in the model by applying an instantaneous deformation equal to the x-translation of boundary B1 over the entire articular surface of the model. This will result in a normal stress at the articular surface which can be analyzed and compared with experiment. The modelling was a 'reverse engineering' type problem, i.e. where input and output are known from the experiments (in this case deformation and load), and the internal model parameters (in this case the material properties of the layers) are adjusted until they produce the known input and output. Material parameters are fitted which result in a normal force close to 59 kPa, the force applied in experiment. This method of deformation is not equivalent to applying a load with a flat, nylon indenter, but should yield similar results in the region of interest under the following assumptions:

1. The indenter is sufficiently large in y and z in comparison to x that there is no depth-related stress or strain focussing.
2. The traction between the indenter and cartilage at the articular surface does not significantly affect the distribution of stress and strain throughout the cartilage.

Assumption 1 is investigated in Section 3.3.5 where it is found that the indenter is sufficiently large that further increase in contact area has negligible effect on the strain distribution in the region of interest. Tractional forces were not measured in the experiment and thus can not be compared, however any tractional force will be cancelled out at the centre of the indenter, which is aligned with the axis over which data is taken. In light of this, tractional forces can be ignored for the sake of comparison of boundary movement along the central x-axis, but need to be considered when investigating the propagation of stress through the rest of the cartilage.

3.3.4 Material Properties

Material models were created for three different levels of complexity:

1. Homogeneity
2. Layered isotropy
3. Layered transverse isotropy

In the first model the AC was assumed homogeneous and isotropic, so the equilibrium mechanical properties could be described by a single elastic modulus and Poisson's ratio

as shown in Table 3.2. A typical value of 1 MPa for the equilibrium modulus of cartilage was used as an initial value, and was refined after each iteration involving comparison of the calculated normal stress at the surface of the model with the actual load applied in the original experiment.

In the second model the AC is assumed to be isotropic, and consisted of three layers each having different mechanical properties. The directional effects of collagen orientation were neglected. A single elastic modulus and Poisson's ratio therefore completely described each layer, which are given in Table 3.2. Layer thicknesses, calculated in Section 3.2 are defined in Table 3.1. The x-strain of each layer in the experimental results were used to determine the initial material parameters. The layer strains were calculated to have a 12:4:1 ratio (with increasing depth), so the elastic moduli for each layer were scaled with the inverse of this ratio. An investigation was carried out into the effects of varying the compressibility of the material, by adjusting the Poisson's ratio of each layer.

The third model assumed AC to consist of three anisotropic layers, each with different anisotropic properties. This allowed the effects of collagen orientation to be investigated via the introduction of anistropic stiffness parameters. Each layer required five parameters to define its equilibrium mechanical properties, given in Table 3.2. The same 1:4:12 strain ratio as the layered isotropic model was used to scale the transverse (x-axis) elastic modulus, and the in-plane (yz-plane) elastic moduli employed a 12:4:1 ratio. The tangential and radial layers thus have a 12-fold difference between the in plane and out of plane elastic moduli, with the transitional layer remaining isotropic. This is a simplification made to shorten the iterative process used to calculate the applied load, and assumes the only heterogeneity affecting the cartilage directional elastic moduli is the collagen orientation. It also assumes that this effect is constant throughout the depth of AC. The transitional layer is deemed isotropic, due to the presence of a dense matrix of randomly orientated interlinking collagen fibrils [23]. A further investigation into the effect of varying compressibility was conducted, this time by varying the directional Poisson's ratios in each layer.

The iterative process used to find the elastic parameters involved first setting the Poisson's ratio(s) to values consistent with the literature (between 0.06 and 0.18 according to Mow and Guo [112]) before adjusting the elastic moduli to match the normal force with the load applied in the experiment. The elastic moduli were selected to fit the criteria explained above. Once the elastic moduli in Table 3.2 were found, the investigations into the effect of Poisson's ratio and compressibility were carried out by incrementing the values m and n.

Model	Tangential		Transitional		Radial	
	E (Pa)	ν	E (Pa)	ν	E (Pa)	ν
1	5×10^5	0.25	5×10^5	0.25	5×10^5	0.25
2	8.33×10^4	$0.05m$	2.67×10^5	$0.05m$	1×10^6	$0.05m$
3	$E_p = 1.2 \times 10^6$ $E_t = 1 \times 10^5$	$\nu_{pp} = \frac{n}{130}$ $\nu_{pt} = \frac{12n}{130}$ $\nu_{tp} = \frac{n}{130}$	4×10^5	$0.05\,n$	$E_p = 1 \times 10^5$ $E_t = 1.2 \times 10^6$	$\nu_{pp} = \frac{12n}{130}$ $\nu_{pt} = \frac{n}{130}$ $\nu_{tp} = \frac{12n}{130}$

Table 3.2: Final elastic parameters prescribed to each layer in the models. Model numbers: 1. Homogeneous, 2. Layered isotropic, 3. Layered transverse isotropic.

Iteration	Arrangement of Squares	Indenter Area (mm^2)
1	2×1	0.02
2	4×3	0.12
3	6×5	0.30
4	8×7	0.56
5	10×9	0.90
6	12×11	1.32
7	14×13	1.82
8	16×15	2.40
9	18×15	2.70
10	20×15	3.00

Table 3.3: Regions on the articular surface over which deformation was applied for investigation into the indenter size.

3.3.5 Indenter Size Analysis

The model relies on a key assumption that a deformation in x of the entire $x = -0.95\,\text{mm}$ surface is sufficiently similar to the act of pressing a flat nylon indenter into the surface as performed in the experiment described in Section 3.2. In order to verify this, the FE model was run with x-deformations applied to regions of varying surface area described in Figure 3.4. The articular surface of the model was partitioned in such a way that the mesh was not affected. Squares of size $200\,\mu\text{m}$ were chosen as their boundaries match those of surface elements (of size $5\,\mu\text{m} \times 100\,\mu\text{m} \times 100\,\mu\text{m}$) and provide adequate resolution for the investigation.

The purpose of this preliminary investigation was to determine the effect of indenter size, and to find if there was a critical size at which depth dependent strain data is no longer accurate. The indenter size used in the experiment was 6 mm by 2 mm and covered the full thickness of the cartilage. The model was repeated with deformation areas spread about this size. The material properties used were the layered isotropic model with Poisson's ratio $\nu = 0.3$.

The results of this investigation (Figure 3.5) show a marked difference in the boundary deformations when the indenter size is small, with the most pronounced differences seen

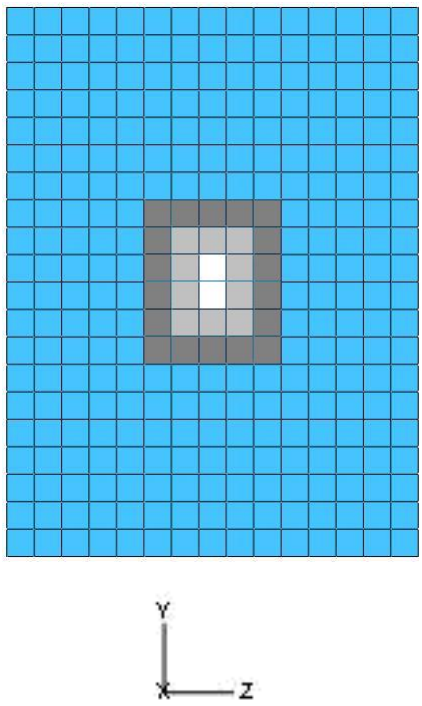

Figure 3.4: yz plane view of the top surface of the model, displaying partition squares used for varying the indenter size. Each square has side 200 μm, the model is 4 mm wide in the y-axis, and 3 mm wide in the z-axis. The three marked regions indicate the areas over which the deformation was applied in the first three models.

in the deformation of B3. Significantly smaller boundary deformations indicate that the regions above the boundaries in question are undergoing larger compressive strains than when the indenter is larger. The results reach a plateau at an indenter size of 1.6 mm $\times$ 1.4 mm after which the deformation change with increased indenter size is small. There is a slight reduction in total deformation as the indenter tends towards the size of the entire surface, but the data remains within 5% of that found in experiment.

It is clear from the results that a larger indenter leads to a deeper propagation of stress and deformation. As the value of 1.6 mm $\times$ 1.4 mm is less than the size of the indenter in the experiment, it can be assumed that the use of a deformation area equal to or larger than this will recreate the stress and strain conditions in the experiment with sufficient accuracy. It should be noted that this set of results only reflects the behaviour for one set of material parameters, but as the trend in the data is flat for indenters significantly smaller than those used in experiment, it is likely that the indenter size does not significantly affect the results for any material models.

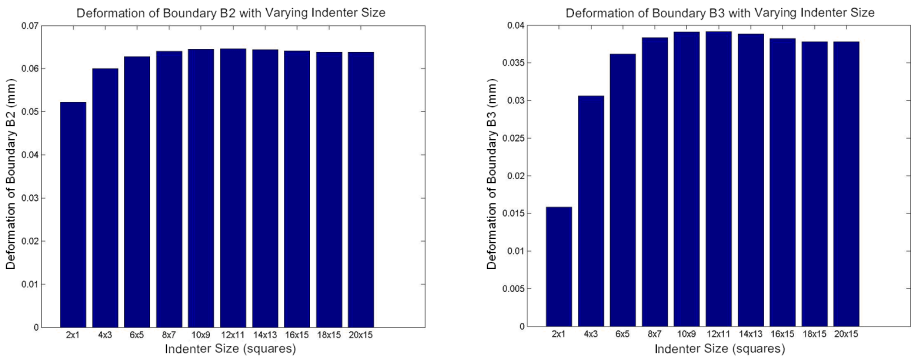

Figure 3.5: Calculated deformation of boundaries B2 (left) and B3 (right) using the layered isotropic model.

3.4 Results

The deformation data throughout the model, and within each layer, were recorded from the centre 1-2 plane, as shown in Figure 3.2, and compared with data from experiment. The variables measured were the three directional stresses and strains, the von Mises stress, and the deformation magnitude. The von Mises stress, Equation 1.15, is a measure of the total distortional energy and how close a material is to yielding under multiaxial stress. Plots of the von Mises stress can be found in Figure 3.7.

3.4.1 Homogeneous Model

It was found that a value of 0.5 MPa for the elastic modulus of the entire cartilage gave rise to a normal stress approximately equal to that applied in the experiment (59 kPa), assuming the cartilage was near-incompressible (with a Poisson's ratio of 0.45). This value increased to 0.6 MPa when a more physiological value of 0.15 was assumed for the Poisson's ratio. This result is in line with results quoted in the literature [103].

It was not possible to match the deformation of each layer to the results obtained from experiment using a homogeneous model, regardless of the chosen homogeneous mechanical properties. Obviously, changing the stiffness of all three layers simultaneously has no effect on the relative deformation of the layers, and changing the Poisson's ratio had little effect. The deformation of each layer in the homogeneous model was 92 μm and 73 μm for boundaries B2 and B3 respectively. Compared with the experimental deformation (Figure 3.1), these figures constitute a 42% and 97% over-estimation and the modelled change in thickness of the Ta layer is underestimated by a factor of 5.5. This means that the homogeneous material model wildly miscalculates the distribution of strain within the AC.

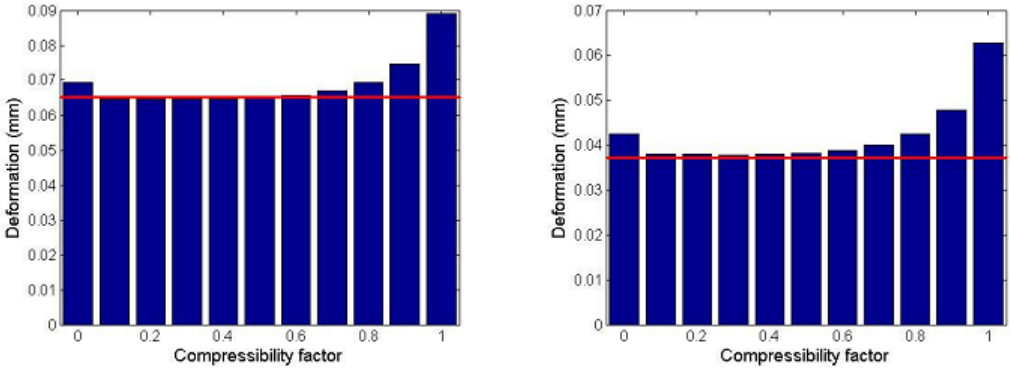

(a) Layered isotropic model

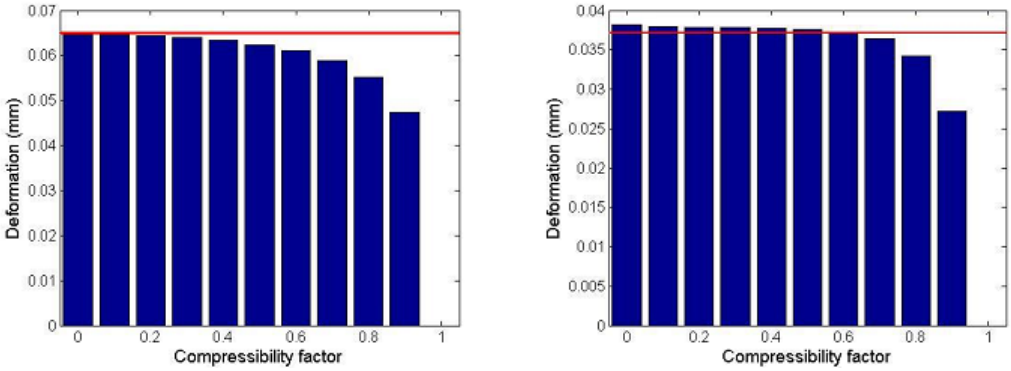

(b) Layered transverse isotropic model

Figure 3.6: Calculated deformation of boundaries B2 (left) and B3 (right) using the layered isotropic model (a) and the layered transverse isotropic model (b). The solid red line represents the experimental deformation, (Figure 3.1).

3.4.2 Layered Isotropic Model

Whilst maintaining a 1:4:12 ratio in elastic moduli between layers (Ta, Tr and R respectively), it was found that layer stiffnesses of 0.083 MPa, 0.33 MPa and 1 MPa produced a normal force equal to the applied load in the experiment. An investigation into the effect of varying compressibility, β on the relative deformation of layers was conducted. The Poisson's ratio was varied between 0 and 0.5 with increments of 0.05, meaning the bulk modulus K bounds varied between $3.3 \times 10^4\,\mathrm{Nm}^{-2}$ and infinity in the Ta layer, and $4 \times 10^5\,\mathrm{Nm}^{-2}$ and infinity in the R layer. The modelled deformation for the Ta and Tr layers are shown in Figure 3.6a.

A Poisson's ratio of between 0.05 and 0.25 resulted in layer deformations matching experiment to within 2 %. However, there is a marked divergence from the experimental data as the material tends towards incompressibility, and at a Poisson's ratio of 0. The material parameters in Table 3.2 result in a normal force of approximately 59 kPa when the compressibility factor 2ν is 0.3 ($\nu = 0.15$). The deviation from the experimental results at high and low Poisson's ratios suggests that the accepted physiological value of 0.06 to 0.18 is optimal for maximum surface deflection in the direction of load.

3.4.3 Layered Transverse Isotropic Model

The transverse isotropic material parameters were determined by setting E_p and E_t in the Ta layer to 1.2 MPa and 0.1 MPa respectively, and by incrementing the sum of ν_{pt} and ν_{tp} (referred to as the compressibility factor in this case) between 0 and 0.9. These values were reversed in the R layer. The effect of this incremental change on the effective bulk modulus was calculated. For a compressibility factor of 0.6 or lower, the tangential layer has higher K values than the radial layer, and at compressibility factor values of 0.8 and 0.9 the bulk modulus bounds for the radial layer increase rapidly. Note that apart from a compressibility factor of 0.9, the bulk moduli of the Ta and R layers are no more than a factor of two different. The calculated boundary deformation results are shown in Figure 3.6b. The trend indicates that the Ta layer deforms more as its bulk modulus reduces in comparison to the radial layer. Using the stated values for E_p and E_t, it was found that Poisson's ratios of $\nu_{pt} = 3.6/13$ and $\nu_{tp} = 0.3/13$ in the tangential layer, and $\nu_{pt} = 0.3/13$ and $\nu_{tp} = 3.6/13$ in the radial layer resulted in a normal force at the articular surface closest to the experimental value of 59 kPa.

3.4.4 Stress Distributions

The stress distribution diagrams (Figure 3.7) display von Mises stress through the $z = 1.5$ mm plane (the middle of the z-component of the model) for each of the above models.

For the homogeneous model, it is evident that the Ta layer experiences much larger surface stress compared with the layered isotropic or layered transverse isotropic model. The stress distribution for the layered transverse isotropic model is more uniform within each layer than in other models, especially in the vicinity of the tidemark, however whether this is realistic for AC is a topic for further investigation. Peaks at the deep edges are anomalous due to boundary effects.

3.5 Discussion and Conclusions

In this work, a layered finite element model was created in order to determine the material properties of loaded AC. Homogeneous, layered isotropic and layered transverse isotropic material models were fitted to the experimental deformation data, and the resulting stress distributions were calculated. The method by which the layer boundaries were calculated involved prescribing tolerances on the angular distribution of collagen, and the boundary locations shifted depending upon the tolerance. The semi-arbitrary nature of the boundary calculations coupled with the fact that they do not correspond with the same material locations in each loading case means that the strains in each layer will have an associated error. This error will affect the calculated elastic parameters, and is difficult to calculate without access to other sets of SAXS results, however the fact that the layered isotropic model stiffnesses closely match those in the literature [107, 113, 108] suggests that this is a viable technique for calculating layer thicknesses.

The homogeneous model could adequately predict the aggregate strain distribution of the AC. However, it was not possible to match the experimentally measured layered deformation data, regardless of the bulk properties used in the model. The lack of consideration of the layered nature of AC, shown in Figure 1.2 yields inaccurate deformation, and therefore inaccurate stress propagation data (Figure 3.7). Therefore a homogeneous model is not useful for predicting or investigating micromechanochemical changes in the solid phase.

The layered isotropic model was able to match the experimental deformation data, and the normal force was comparable to the compressive pressure applied in the experiment. It was found that assuming a compressibility factor of 0.3 throughout the model, the Young's modulus of the radial layer would have to be 12 times that of the tangential layer. To match the deformation data for compressibility factors greater than 0.3, the ratio of Young's moduli between the layers would require further increase. This seems a large difference, however confined compression tests of cartilage explants have shown that there is a very large difference between the aggregate modulus of the surface layer

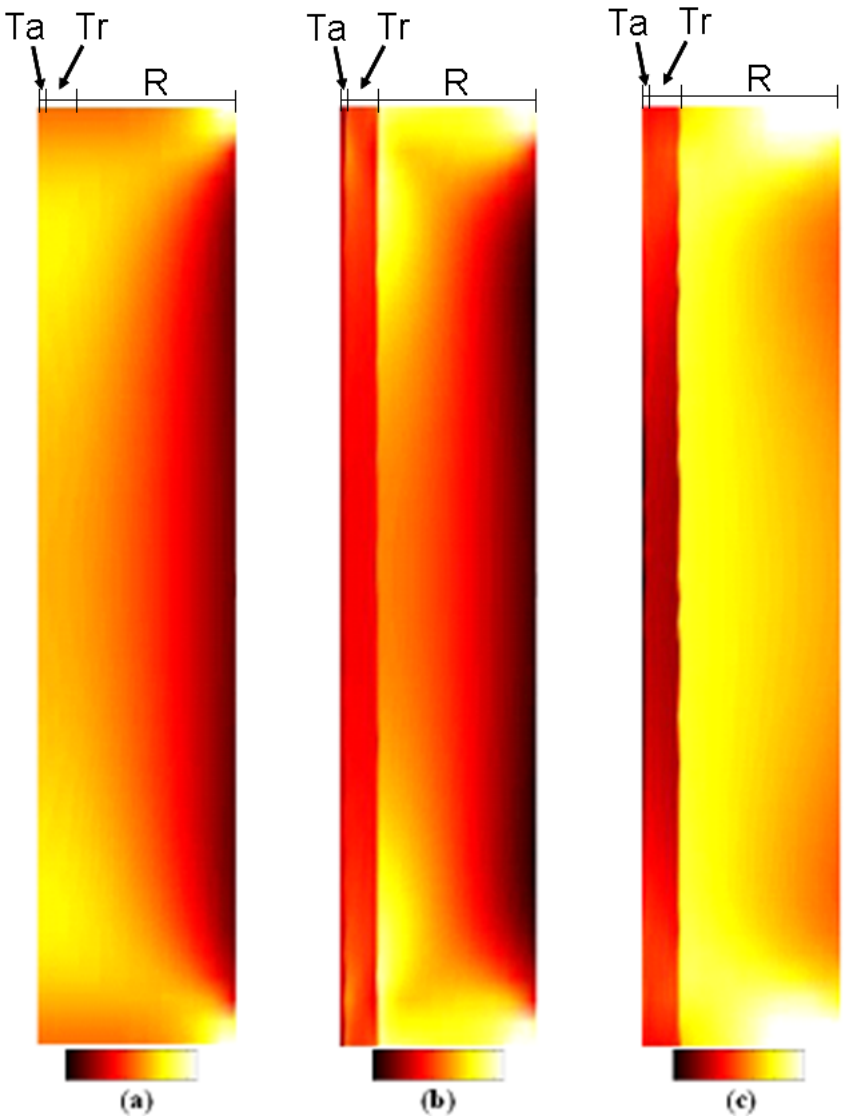

Figure 3.7: Cross sections of the cartilaginous region ($z = 1.5$), shown in Figure 3.2) showing calculated von Mises stress propagation for the (a) homogeneous model, (b) layered isotropic model, (c) layered transverse isotropic model. The articular surface is the left edge and the model depicts the unstrained geometry which is 0.95 mm deep (horizontal) and 4 mm across (vertical). The colour bars are linear with stress ranging between 38 kPa and 60 kPa.

(0.079 ± 0.039 MPa) and regions near the tidemark (1.14 ± 0.44 MPa) [107]. The exact compositional reason for these large differences is still unclear, and is likely due to a combination of factors, such as the variation in water content, GAG content and type, collagen content and structure. It is clear from the layered isotropic stress data that the von Mises stress reaches a peak (0.46 MPa) just below the boundary B3, demonstrating a transfer of potentially damaging stress away from the superficial layers.

When there are two abutting layers with very large differences in stiffness, such as between the R and Tr layers, here, under compressive load there will be relative shear deformation between the two (unless there are similarly large differences in Poisson's ratio). The layered model has a step change in properties which is not the case in the real tissue. Nevertheless away from the step change boundary the overall pattern and magnitudes of shear strain between the abutting layers will be reflective of the real situation. Interfacial shear is of course minimal on the central axis underneath the applied deformation, and increases as a function of distance along the interface away from the central axis. This interlayer shearing may be physiologically or pathologically important, and is captured by the layered FE models. There is significant physiological interest in the transfer of stress across the tidemark, a feature which was omitted from the results due to the high stresses. The boundary between the normal and calcified cartilages represents a step change in stiffness of an order of magnitude, leading to large shear forces under load. This is demonstrated by the initial failure of AC under abnormally high loads along the tidemark [28].

The introduction of anisotropy removes the direct link between the 'apparent' stiffness (related to the strain observed) and the bulk modulus of the AC (incorporating elastic moduli and Poisson's ratios in all directions). The results in Figure 3.6b show that when the bulk modulus of the radial layer was similar to or less than that of the tangential, the deformations were similar to those observed in experiment. This contradicts isotropic models of AC, in which the bulk modulus scales to the Young's modulus (assuming the Poisson's ratio remains constant with depth). The extent to which the bulk moduli differ is dependent upon the compressibility factor of the model, as well as the ratio of directional elastic moduli in each layer. In order to pin down these variables, the directional stiffness of each layer of the AC would need to be found experimentally, this is the topic of investigation in Chapter 4. Also evident in this model was the stress-transfer mechanism evident in the layered isotropic model, with stress peaks (0.61 MPa) at the top of the radial layer. The distribution of stress is less homogeneous in this model, with comparatively lower stresses in the Ta and Tr layers, and lower boundary stresses due to the differences in ν_{tp} between layers.

The calculated stress propagation for each of the models has shown the importance of con-

sidering AC as a layered, heterogeneous and anisotropic media. It is well established that one of the major functions of AC is to act as a 'cushion', distributing externally applied loads and thereby reducing stress concentration on the articulating bones and the bone-AC interface, while still distributing stress appropriately within the AC so as to minimize the internal damage. The stress pattern for the homogeneous model clearly shows that the stress propagation (Figure 3.7) is inappropriate since the calculated stress peak appears at the top surface of the AC and is therefore likely to be damaging. Introducing layers moves the peak stress to move further down into the AC, therefore minimizing potential damage to the Ta layer. The more complex transverse isotropic model showed similar stresses and deformations as the layered isotropic model, with the additional feature of a more uniformly distributed stress propagation within each layer.

McCutchen [55] stated that the mechanical anisotropy conferred to the articular surface by the collagen is essential for the weeping lubrication mechanism. The surface layer of cartilage is clearly of fundamental physiological importance, and it is therefore vital to minimise damage to it. The work in this chapter has shown that the transverse isotropic nature of cartilage minimises potentially damaging stress at the surface, instead transmitting it to deeper regions. The compaction of the surface layers under low loads has been shown to have an implication on the permeability of the articular surface, and therefore the timescale over which cartilage efficiently lubricates [34]. The small equilibrium Poisson's ratios associated with AC have been shown to be ideally suited for maximum compaction of the surface layer, allowing efficient lubrication and congruence between joint surfaces

In summary, it was found that a transverse isotropic model is needed to accurately describe the elastic behaviour of the solid phase of AC in the absence of large compositional differences between tangential and radial regions. It is important for research into chondrocyte mechanotransduction that the local distribution of physiological stress and strain are well understood, and introduction of the transverse isotropic model presented here takes a step towards this. This model of the solid phase of AC could be readily transferred into a poroelastic or multiphasic model to address the transient deformation of AC.

Chapter 4

Mechanical Testing

The model described in the previous chapter showed that the layered nature of articular cartilage (AC) endows it with material properties that can not be described with a single set of material parameters. The layered isotropic model can recreate the deformations observed in experiments by scaling the Young's modulus of each layer linearly with the observed strain. There is, however, insufficient experimental data on the model parameters to give exact values for the transverse isotropic elastic moduli. The aim of this chapter is to determine experimentally the degree of mechanical anisotropy in cartilage to strengthen the conclusions of the previous chapter, and gain mechanical stiffness data from each layer that can be used in future models.

Mechanical properties of tissue are examined using the tensile loading rig described in Section 2.2. It has been established in Section 1.2.1.4 that cartilage mechanics differ considerably in tension and compression and samples are tested in tension for two reasons. Firstly, the thickness of the individual layers (particularly the tangential layer) makes compression testing prohibitively difficult and inaccurate, and secondly, the application of a normal load to the articular surface gives rise to a tensile lateral force. Measurements of the tensile elastic moduli of samples in plane with the underlying bone will therefore provide data more applicable for modelling of experiments like those in Chapter 3 than measurement of their compressive counterparts.

There have been several investigations into the tensile properties of articular cartilage which have been summarised in Section 1.2.1.4. The motivation behind performing further tensile tests is the lack of information about the tangential layer. The tangential layer of a sample of AC tested by Moger et al. [28] was shown in the previous chapter to be approximately 50 μm thick. Most published data on the depth varying tensile modulus of AC has involved testing 200 μm thick slices, often with some of the surface removed to ensure a regular thickness. Although trends with depth are obtained, the behaviour of

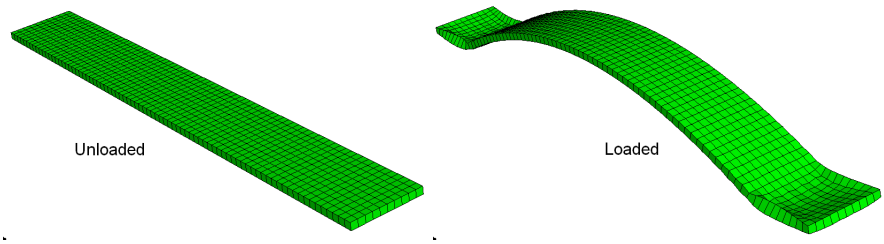

Figure 4.1: Geometry of FE model describing a strained cartilage sample. The sample is fixed at the ends on the top surface shown in the images. Note that the deflection is exaggerated in the right (loaded) image for the sake of clarity.

the tangential zone is blurred with that of deeper AC, losing valuable information. The primary contribution this work makes is obtaining 20 μm slices from the tangential zone and finding their tensile mechanical properties.

This chapter begins with a finite element analysis of the experiment, in which the method of gluing a sample on one side and straining it from that edge is compared with the traditional method of using a clamp. The following section describes an investigation of split line orientation performed across the articular surface of the metacarpal in the metacarpophalangeal joint for comparison with polarised light microscopy (PLM) images and tensile test results. The third section details the use of PLM on the samples used for tensile testing, which is used to find accurately preferential orientation of collagen. The fourth section documents the results of the tensile test and trends in the tensile stiffness with depth, orientation of split line and orientation of collagen. The final section discusses the findings of the chapter and their relevance to the mechanics of AC.

4.1 Numerical Model of Strain Method

Most tensile testing experiments involve clamping a sample between two rigid metal blocks. This provides a near-perfect boundary at which the sample strain is zero. The method of sticking a sample along one edge provides a rigid boundary on the stuck side of the sample but not on the opposite side. The samples are thin, and therefore the associated shear deformation in the vicinity of the paddles will be small, however the effect of the asymmetric force distribution on the rest of the sample is not clear.

The model geometry replicated that used experimentally: a cuboid of length 4 mm, width 500 μm and thicknesses of 50 μm, 100 μm, 250 μm and 500 μm respectively. Encastre boundary conditions were applied to a 500 μm $\times$ 500 μm square at each end of the sample on one side, leaving a 3 mm length over which tensile strain is applied. Figure 4.1 describes the geometry of the sample before and after applying a tensile load. A linear elastic material model was used with a Young's modulus of 10 MPa and Poisson's ratio of 0.45.

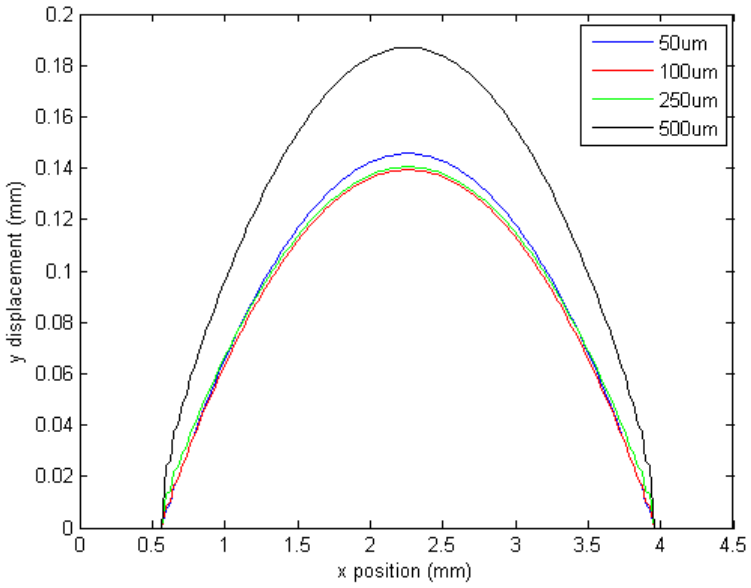

Figure 4.2: Calculated y-deflection caused when straining a sample by 13 % in x. The legend corresponds to the sample thickness.

The effect of the fixed condition being applied to only one side of the sample is to cause it to bend towards the fixed side. The point of maximum deflection was at the mid point of the sample (see Figure 4.2) and was greatest in the thickest model with a value of 187 μm. The sample exhibits a maximum angle from horizontal in the xy-plane of 24° also in the thickest model. The von Mises stress propagation was calculated (Figure 4.3) to determine whether the stress can be assumed uniform across the sample. In the illustrated example (100 μm thickness), the stress varies by up to 10 % when considering individual points, however the average stress over a cross section $x = const$ does not vary by more than 1 %. This trend is repeated in the other three models.

No slice used in this investigation was greater than 250 μm thick. The 50 μm, 100 μm and 250 μm thick models have a maximum y-deflection of 146 μm which corresponds to a sample *length* of 3.404 mm, an increase of 0.4 % over the length of 3.39 mm had the sample not been deflected. The variation in maximum y-deflection of the three thinnest samples was 6 μm which corresponds to a variation in sample length, and hence a variation in applied deformation of less than 0.01 %.

In summary, although the use of glue as opposed to clamps leads to a y-deflection, and hence increased length strains, it does not result in a significant error for comparison between samples. The effect of the y-deflection on the final calculated tensile moduli will be an overestimation of approximately 3 %, assuming it to be calculated at 13 % strain, and assuming linear elastic behaviour at this level of strain.

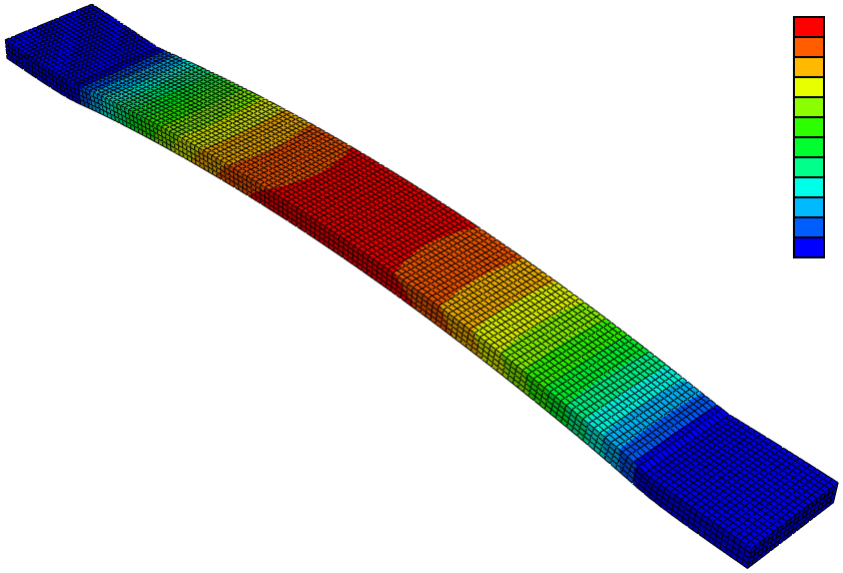

(a) Vertical displacement. Linear colour gradient with minimum value 0 μm and maximum value 139 μm.

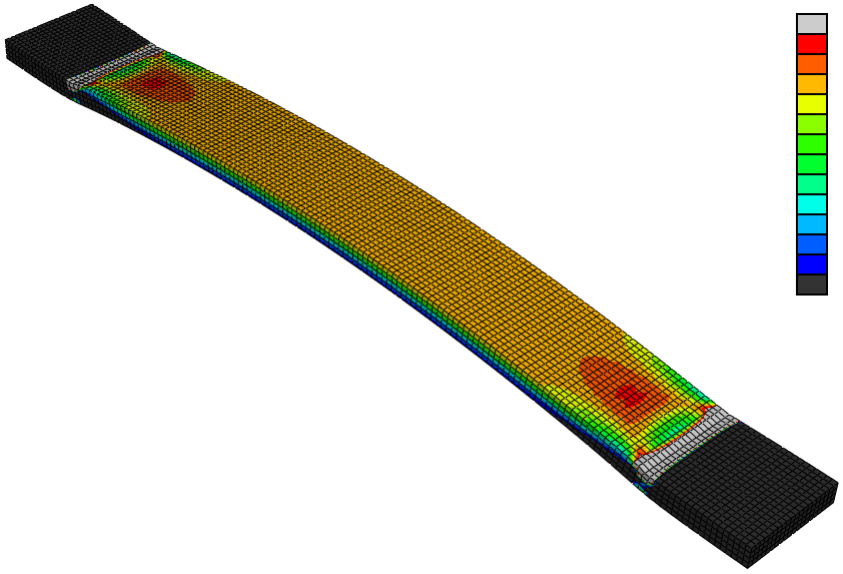

(b) Von Mises stress. Linear colour gradient with minimum value 1.2 MPa and maximum value 1.32 MPa. The grey areas represent regions with large erroneous stresses associated with the fixed boundary conditions.

Figure 4.3: y-deflection and von Mises stress in strained sample. Model dimensions 4 mm $\times$ 500 μm $\times$ 100 μm.

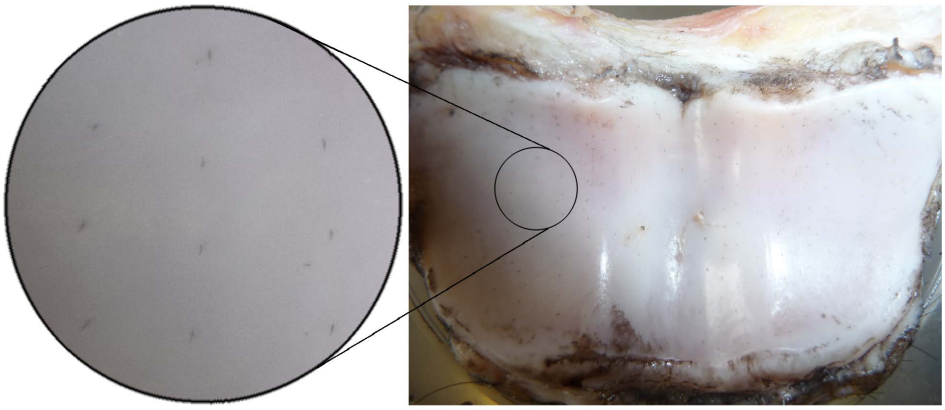

Figure 4.4: Split lines on the equine proximal phalanx. The articular surface is approximately 5 cm in width.

4.2 Split-Line Investigation

The split line method, described in Section 1.1.2.1 was used to visualise collagen orientation over the three articular surfaces of the MCP joint. The clarity of the split lines varied considerably and was clearest in the proximal phalanx (see Figure 4.6).

Regions around the condylar plateaus of the metacarpal were unclear, suggesting there may not be a strongly preferential orientation of collagen in these regions. Despite the lack of clear split line data, these regions were used in mechanical testing as there exists SAXS data [7] from this region obtained in the same manner as that which is used in the model in Chapter 3.

4.2.1 Cartilage Samples

Three fresh equine left forelimbs were obtained from the local abattoir and dissected on the same day. The horses were aged 7, 7 and 10 years and each exhibited faint butterfly lesions - early signs of OA. Saggital sections were made on the lateral side of the joint to aid in sample explantation.

Full thickness explants approximately 9 mm $\times$ 9 mm in surface area and between 300 μm and 700 μm thick were excised from the three regions of the metacarpal used for SAXS by Moger et al. [7]. These regions lie on the saggital plane approximately midway between the saggital ridge and the edge of the bone, see Figure 4.5.

Samples were punctured and covered in Indian ink which was left to dry for approximately an hour before being wiped off. The sample was then viewed under a microscope at

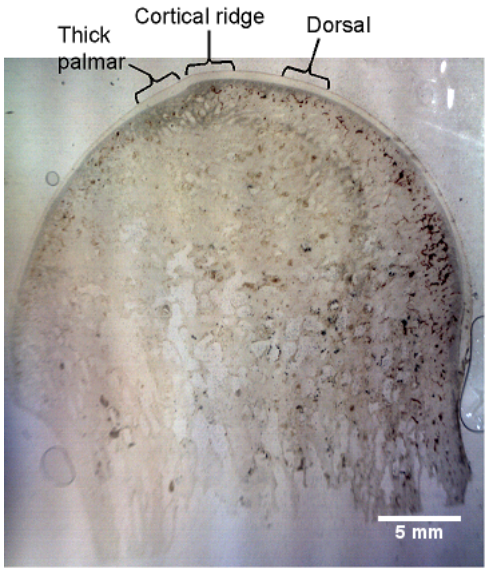

Figure 4.5: Thin saggital section of the metacarpal obtained by polishing a thick microtome section on a diamond wheel. Section provided by Don Attenburrow. The three regions from which cartilage samples were taken are labelled as thick palmar, cortical ridge and dorsal and correspond to the thick, apex and medium locations in [7].

4× magnification to determine the split line direction. The microscope used also has insertable polarising filters for PLM which was used as a verification that the split lines follow the preferential orientation of collagen, see Figure 4.6.

The split lines varied considerably in clarity. The thick palmar region always showed clear split lines in consistently the same direction, whereas split lines in the dorsal region showed little or no trend and estimates had to be made from surface patterns using PLM on full thickness samples *en face*. The split lines in the cortical ridge were clear but not as well-defined as those of the thick palmar region.

Using this information, strips both parallel and perpendicular to the split line were taken for each sample. From these strips, slices from the Ta, Tr and R layers were obtained using a microtome. There are therefore 18 sets of data obtained from each of the three horses.

4.3 Polarised Light Microscopy

Polarised light microscopy is used for three purposes in this work, these are:

- Measurement of the layer thicknesses in strips of AC prior to slicing on the microtome (Figure 4.7).
- Assessing the viability of a sample for tensile testing by checking for uniform width and thickness, as well as checking for damage to the collagen network.

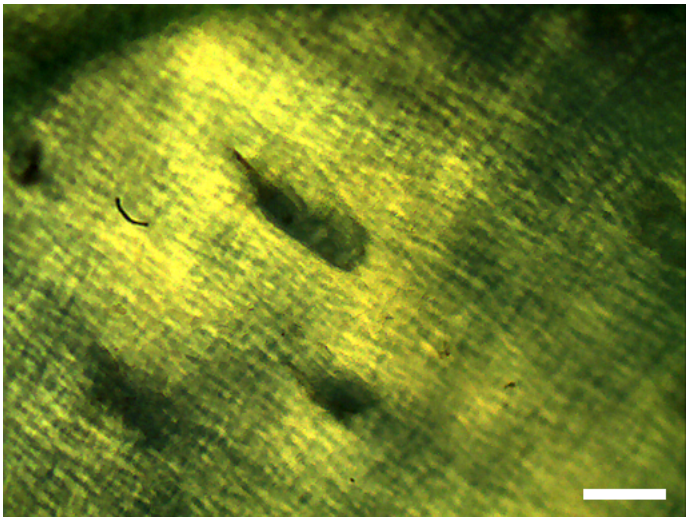

Figure 4.6: Split lines on a full thickness cartilage explant viewed under PLM. Bar 200 μm

- Imaging of the collagen arrangement for the purposes of determining the preferential collagen orientation. An image is taken with the polarising filters at the angle at which maximum signal is observed.

Although layers can be seen in Figure 4.7, rotation of the polarising filters can cause layer boundaries to appear to shift, and so this technique is only used as a rough guide when taking slices with the microtome. Typically, the topmost intact 20 μm slice is used for the Ta sample, and the saggital cross section is used to determine the most superficial point at which the Tr layer begins. In serial slices approaching this point, PLM shows an arrangement change from Ta to Tr (described later). Once the images confirm that the Ta layer has been completely removed, the microtome is adjusted to take a thicker slice which will be completely contained within the Tr layer. The same process is used for taking radial slices, and samples are continually taken until the bottom is reached. The deepest intact slice is used as the R sample.

A sample is viable for tensile testing if it contains a sufficiently long region (in the direction of strain) where the two pairs of edges are parallel. Most samples are parallel along their whole length but occasionally samples can snap in the microtome leaving irregularities in their geometry.

4.3.1 Collagen Structure

There were very marked differences in the organisation, preferential orientation and signal intensity of the collagen network both with depth and across the surface of the joint. Tangential slices displayed thin fibres arranged in a woven pattern with very clear preferential orientations. Transitional slices varied considerably, with most demonstrating patches of

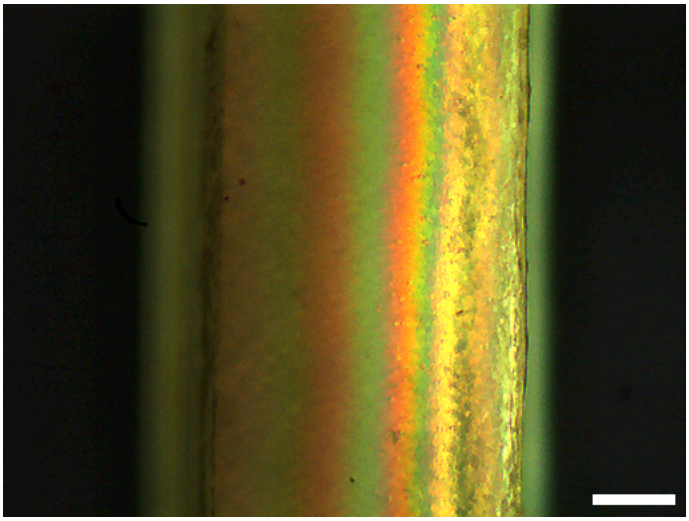

Figure 4.7: An image of the cross-section of a full thickness cartilage sample after vertical cutting obtained using PLM. This sample was taken from the thick palmar region of sample 3, parallel to the split line. Bar 200 μm.

different intensities and preferential orientations, with either a very weak or no overall preferential orientation. Radial slices exhibited the most unusual behaviour of the three layers, as despite containing radial fibres, the images show a fibre-like structure in the plane of the section, with 'fibres' much thicker than those near the surface. Figure 4.8 shows examples of samples from the three regions.

The following sections describe the trends observed from the three layers of AC. Images were taken when the sample was orientated at an angle between the crossed polarisers which resulted in the maximum signal being received from the sample. The arrangement of collagen in these images may be the most abundant orientation, but it should be noted there exist fibres within the samples at different orientations in less abundance.

4.3.1.1 Tangential Zone

The orientation of fibres in the tangential images is within 20° of the split line direction in 17 of the 18 samples, with one clear exception. The perpendicular slice from the thick region of sample 2 exhibited near-parallel fibres, suggesting that fibres from this region are close to 90° different in orientation to the region around the split line. The size of the samples from which strips are taken represent a significant fraction of the articular surface and if fibre orientation reflects loading pattern, it is possible that physiological loading conditions could vary from one side of the sample to the other.

Signal from the very surface of the tangential zone of all samples was considerably brighter than anywhere else. This region (less than 10 μm thick) appeared otherwise exactly the same as the rest of the Ta layer. The cartilage from this region was discarded in order to

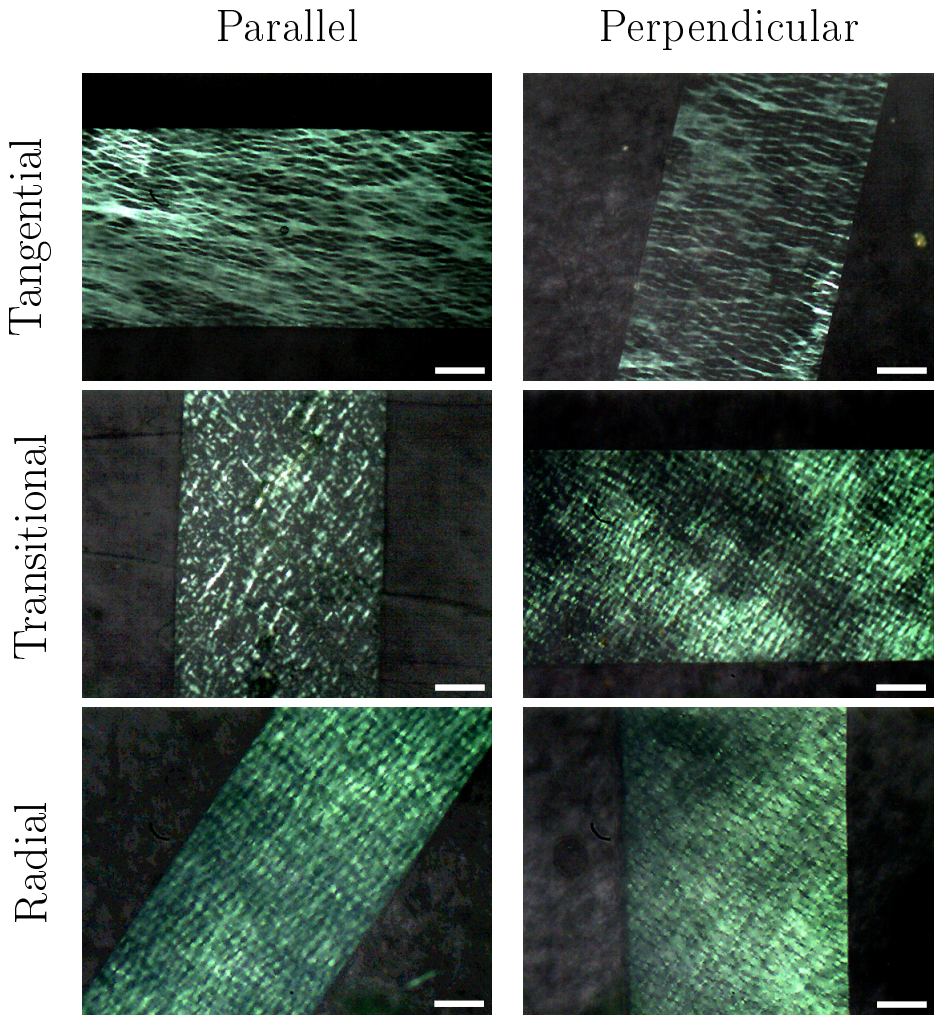

Figure 4.8: Polarised light microscopy of cartilage slices prior to tensile testing. Images on the left are taken parallel to the split line, and samples to the right are perpendicular. The top images are taken from tangential slices, the middle images are taken from transitional slices, and the bottom images are taken from radial slices. Bars 200 μm.

obtain uniform thickness slices from the rest of the Ta layer, however the tensile properties of this layer may be of interest for future work. The perpendicular Ta sample in Figure 4.8 contains a small amount of the bright surface fibres on the right edge.

The thin Ta fibres shown in Figure 4.8 are from samples from the thick palmar region. The fibres visible at the resolution of the camera appear to vary considerably in thickness. The thinnest resolved fibres are approximately 5 μm thick, while the thickest are around 15 μm. Fibres appear to regularly branch into thinner fibres, and there is considerable patchy blurring which presumably indicates regions of more fibrillar collagen.

Tangential samples from the cortical ridge and dorsal regions exhibit the branching behaviour described above, but with less defined variations in thickness and less patchy blurring. Some cortical ridge Ta samples exhibited patches of varied orientation and signal akin to the transitional zone, and this is likely due to the fact that the tangential zone is so thin in this region [7]. Collagen fibre thickness in both the cortical ridge and dorsal regions remains mostly consistent between 7 μm and 10 μm. Samples from the dorsal region have a more isotropic distribution of fibres than other regions, with only a slight bias in the split line direction.

4.3.1.2 Transitional Zone

The transitional zone exhibits the most variation between samples. The only repeatable trend is the patchy nature of the signal intensity. Patches appear to be between 200 μm and 400 μm across and roughly square. Patches also correspond in some cases to regions of different preferential orientation, although all samples exhibit a clear preferential arrangement.

Collagen is arranged in a much broader spread of angles in the tangential zone, even within individual patches. In most images the collagen orientations are around $\pm 45^\circ$ to the split line. However, the birefringent rotation of the polarisation of light is maximal when fibres are orientated at $\pm 45^\circ$ to the incident polarisation [166], and hence the signal intensity is related to the number of fibres orientated close to these two orthogonal directions. If there was a small increase in the number of fibres as the orientation varied from $\pm 45^\circ$ to 0°, but a large decrease from $\pm 45^\circ$ to $\pm 90^\circ$, then a larger signal would result when the $\pm 45^\circ$ fibres are viewed.

The spread in collagen orientation varied between samples. The dorsal and cortical ridge samples exhibited very clear patchy behaviour, and weak preferences in the orientation. The thick palmar region however, showed clear fibres in the direction of articulation, little spread in fibre angle and less patchy behaviour. The fibres are thicker than in the Ta layer, and similar to those in the R layer. Sequential thin sections between the Ta and

Tr slices showed a gradual increase in fibre thickness and no randomly orientated, patchy zone like those seen in the dorsal and cortical ridge samples.

4.3.1.3 Radial Zone

The most apparent difference between the radial zone and the others is the background intensity. The background intensity refers to the signal from spaces between fibres, and in the other two zones it is negligible. This suggests that there is a component of the AC outside of the fibre-like architecture which is causing birefringence.

Perhaps the most surprising result from all the PLM images is the lateral fibrous architecture seen in some samples. Every radial sample was taken from sufficiently deep into the tissue (according to Moger et al. [7] and saggital images) to ensure radial alignment of collagen fibres, so the presence of this tangential, fibre-like texture was not expected. The thick palmar region exhibited the clearest fibres, all aligned with the split line and maintaining a similar morphology to the transitional zone. The cortical ridge also demonstrated some directionality, although the fibres appeared shorter and thicker and in many places appeared just as dots, suggesting a radial structure which has been cut through. The dorsal region exhibited virtually no lateral directionality, with most regions of higher intensity appearing as just dots.

4.4 Tensile Testing

Tensile testing was performed using the tensile loading rig (Figure 2.3) using the method described in Section 2.2.1. Although samples were dry during attachment to the paddles, the glue did still creep a small way along the sample. Imaging of a glued sample after tensile testing revealed that the extent of creep was around 100 μm to 200 μm, which constitutes between 3 % and 7 % of the length of the samples. The magnitude of the effect on the stress-strain behaviour of the sample is dependent upon the geometry of the crept glue and the relative stiffness of the glue and sample in tension. Care was taken to minimise the extent of glue creep in order for it to be regarded as a systematic error.

Samples were strained incrementally up to a final strain of around 20 %. A final strain of 20 % was not reached for all samples due to failure of the sample or glue. Samples were allowed to reach mechanical equilibrium before a reading was taken, and this took between a minute at low strain and over an hour at high strain.

Layer	Parallel tensile modulus (MPa)	Perpendicular tensile modulus (MPa)
Tangential	43.4 ± 3.5	18.3 ± 1.5
Transitional	16.4 ± 1.3	18.6 ± 1.5
Radial	8.7 ± 0.7	10.2 ± 0.8

(a) Comparison between strips aligned parallel and perpendicular to the split line.

Layer	Mean tensile modulus (MPa)
Tangential	31.3 ± 2.5
Transitional	17.4 ± 1.4
Radial	9.4 ± 0.8

(b) Average tensile moduli.

Table 4.1: Tensile moduli of each layer.

4.4.1 Variations with Depth

Figure 4.9 describes the quasi-static stress-strain behaviour of all the samples used in this investigation. The lines correspond to the linear elastic stiffness calculated from the 5 %-15 % strain data. This range was chosen in order to avoid the toe region characteristic of most biological materials [130] and the limit at which the stress-strain behaves nonlinearly [123, 92]. The intercepts of the lines with the y-axis provide information about the nonlinear behaviour at low strains. Larger versions of the stress-strain graphs without the overlaid lines can be found in Appendix A.

The graphs show a clear difference in the stress-strain behaviour between the tangential and radial AC. The majority of the tangential layer data exhibit a characteristic stress-strain curve with a clear toe region, linear region and nonlinear region when sufficiently high strains were reached. The radial data however exhibits S-shape stress-strain curves in many cases, and in consequence many of the linear elastic fits have positive y-intercepts. The transitional layer in most cases follows the trend of one of the adjacent layers.

The average tensile moduli of each layer (Table 4.1) show that the tangential zone is the most stiff, and the radial zone the least. Comparison between parallel and perpendicular regions shows that in the tangential zone the parallel slices are on average considerably stiffer than the perpendicular ones, although there is no statistically significant trend in the other two zones. There is, however, considerable variation between samples.

The strain at which the toe region ends and the sample begins to behave linearly is equal to the intercept divided by the stiffness. This value provides information about the ability of collagen to reorientate, although performing this analysis on the data did not yield any statistically significant results. It should be noted, however, that the toe region end point did not vary significantly between parallel and perpendicular samples, even in the tangential zone.

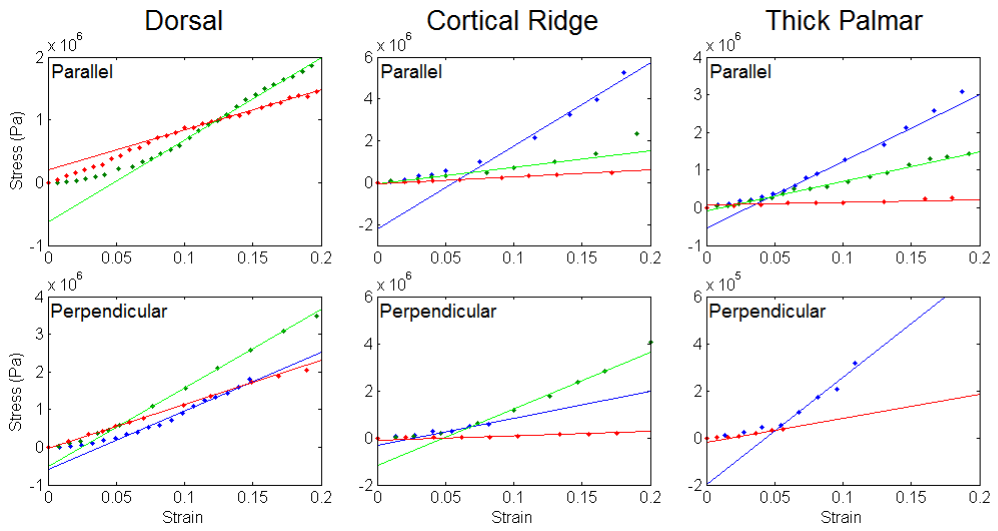

(a) Sample 1

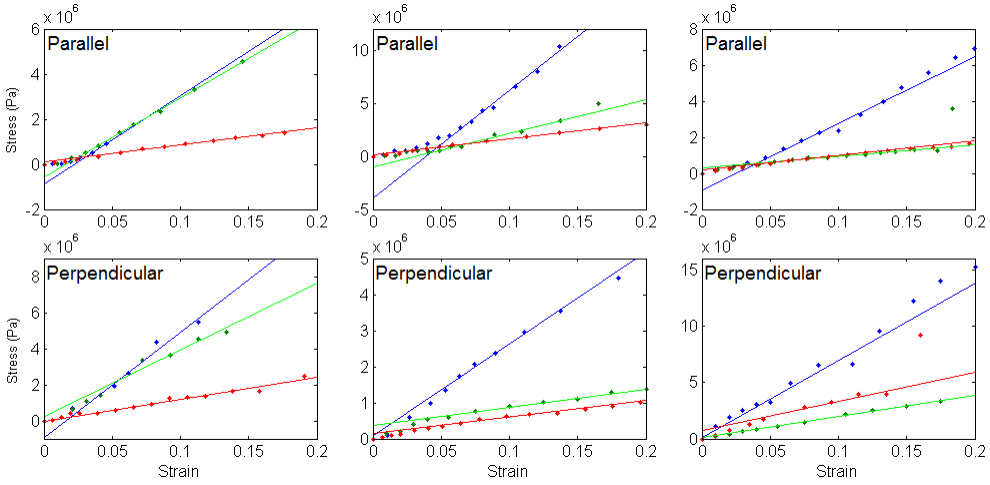

(b) Sample 2

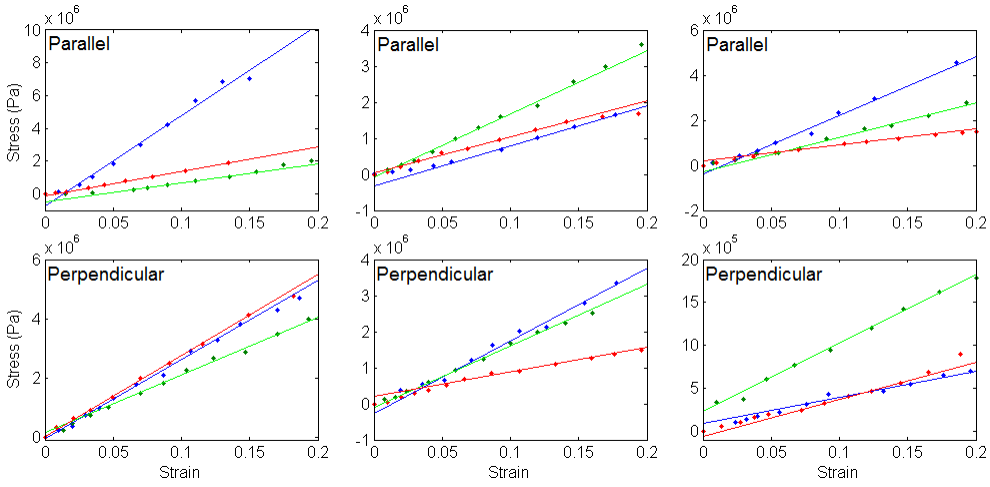

(c) Sample 3

Figure 4.9: Uniaxial tensile stress-strain responses of the three tested samples. Blue corresponds to the Ta layer, green to the Tr layer, and red to the R layer. Each sample was tested parallel (top) and perpendicular (bottom) to the split line. Samples were taken from the thick palmar (left), cortical ridge (middle) and dorsal (right) regions of the metacarpal, see Figure 4.5.

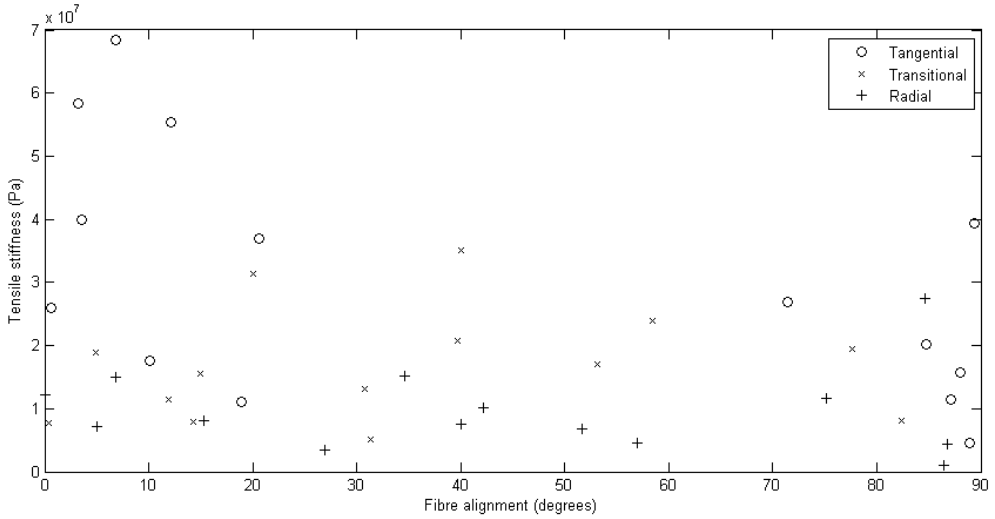

Figure 4.10: Relationship between fibre angle and tensile stiffness. 0° corresponds to the direction of applied strain.

4.4.2 Comparison with Fibre Orientation

The directionality plugin for the ImageJ distribution Fiji was used to determine the most abundant fibre orientation in each PLM image. Figure 4.10 plots the preferential orientation angle against the tensile stiffness of the slice, and shows a weak downward trend away from the direction of the split line (0°). The graph also shows the distribution of orientation, which clearly shows that the split line only corresponds to fibre orientation in the tangential region. The trend in tensile stiffness is made more clear in Figure 4.11, which displays the tensile stiffness data from the tangential zone in pairs, for which all but one of the perpendicular slices are more compliant than the respective parallel slices. Similar graphs for the transitional and radial zones do not demonstrate any significant trends and are omitted.

4.5 Discussion

The primary aim of the work in this chapter was to determine the tensile mechanical properties of each layer of AC, particularly those of the tangential layer, which had not previously been isolated and examined. The assumption was made that AC behaves as an orthotropic linear elastic material at equilibrium under tensile strains of up to 15 %, with the stiffer axis parallel to the split line. Samples of AC were collected from regions of the equine metacarpophalangeal joint which have previously been investigated using SAXS, and split lines were analysed. Strips were taken parallel and perpendicular to the split line for each sample, and slices from each of the three layers within the strips were imaged under PLM and then mechanically tested.

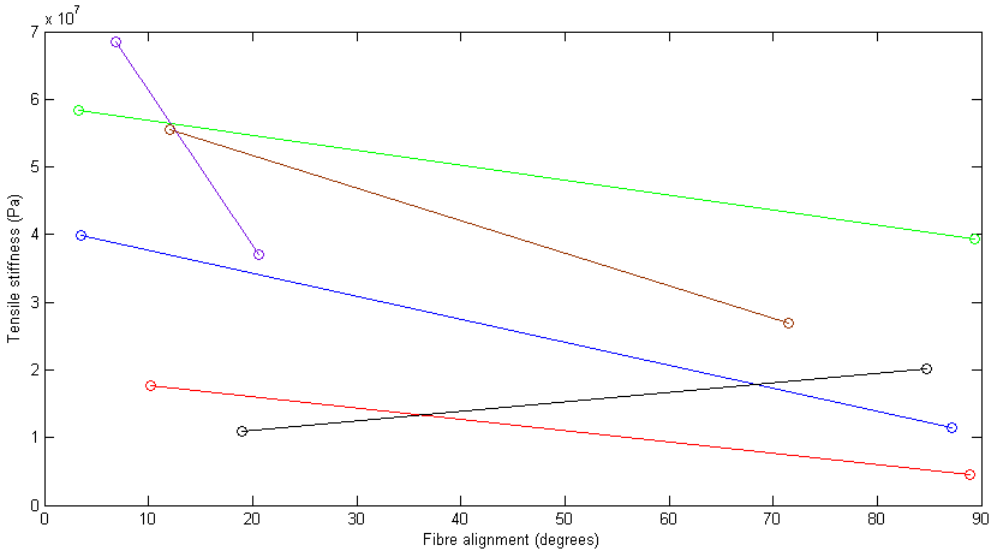

Figure 4.11: Relationship between fibre angle and tensile stiffness for tangential slices. Paired data points came from the same original sample.

To fully characterise the tensile properties of an orthotropic material in a plane, three strips from the same sample at 0°, 45° and 90° to a reference direction need to be tested. However, if the direction of maximum tensile stiffness is known then only two tests are needed, parallel and perpendicular to this direction. Limitations due to the size of the samples made performing three tensile experiments too difficult, and hence the split line method was employed to provide information about the directionality of stiffness. The variation in clarity of the split lines is possibly due to different degrees in bias of collagen orientation. The punctures on the dorsal region were almost perfectly circular, and deviations were not in a repeatable direction, making determination of the split line direction difficult. Split lines on the thick palmar region (Figure 4.6), however, were all very clear. The trends in split line clarity match those of the degree of anisotropy in the collagen orientation determined using PLM. The dorsal region revealed only a weak preferential orientation in the surface layer, which was not repeated in the deeper layers, while the palmar region exhibited a clear preference in fibre orientation throughout all depths. The fact that the cortical ridge region also produced clear split lines suggests that the split line direction is governed by the orientation of the surface layer. As such, although the split line generally infers the direction of greatest tensile stiffness, this only applies to the tangential zone and will not provide information about variations in the deeper zones. These findings correspond with those of Kamalanathan and Broom [13].

PLM was used to determine the preferential orientation of collagen in each sample. The images show a large range in the organisation and morphology of collagen with both depth and location across the joint. The lines of signal at the surface are likely to be bundles of collagen fibres, as they are of the right thickness ($< 12\,\mu$m, [14]). The surface ridges on

stretched AC recorded by Sasazaki et al. [129] using SEM are slightly smaller than those seen under PLM in this work, but resolution limitations of the camera may have caused the fibres to appear wider. Transitional slices revealed a more isotropic network of fibres, but one which appears in patches of different orientation and intensity. The leaf structure of collagen discussed in Section 1.1.2.1 may explain this arrangement, as overlapping leaves of collagen fibre bundles will each have subtley different arrangements. As different leaves will curve into a tangential orientation at different depths, the more radially aligned fibres will exhibit less signal making some patches appear darker. The fibre-like patterns observed in the radial zone are unexpected as the literature has clearly shown that collagen in the deep zone is primarily aligned radially. There are two possible explanations for this pattern of signal, the first being that the lines are simply cross sections through leaves of collagen bundles. It is not clear whether the leaf structure penetrates deep into the radial zone, evidence that it does has been based upon SEM-based observations which have been suggested to be artifacts [69]. It is possible that the collagen structure in the radial zone appears leaf-like due to the regularly spaced radial arrangement of groups of chondrocytes which separate the collagen. An alternative explanation may be that the structure is simply a mesh of quasi-randomly orientated fibrils with sizes below the limit of resolution for the imaging technique which are separated by chondrocytes, giving the appearance of ordered fibres when the ordering in fact comes from the dark regions. The presence of disordered fibrils may also explain the higher background signal in the radial layer.

The tensile testing data highlights the large depth-dependent variation in mechanical properties over just the surface 100 μm. The tangential zone is nearly twice as stiff in tension as the transitional zone, and in places is less than 50 μm thick. The stress-strain behaviour of the tangential zone is typical of that of a biological material in tension, as described by Fung [130]. More specifically the behaviour is similar to that of the thicker surface region samples from bovine patellofemoral joints tested by Roth and Mow [123], although the tangential slices used in this investigation were consistently stiffer. Radial zone AC goes completely against the biological material model and exhibits a repeatable trend of strain-softening at strains of approximately 8 %. This rubber-like behaviour has also been documented by Roth and Mow, who found that despite seemingly undergoing plastic deformation over the range of 10 % to 50 %, samples were found to then behave linearly up to strains in excess of 100 %. Tensile tests of full thickness samples performed by Sasazaki et al. [129] yielded behaviour between the two documented here, with samples behaving linearly up to strains of between 20 % and 25 % before becoming more compliant, and failing shortly thereafter. The fact that the mechanical response of the transitional region often matches that of either the tangential or radial zones, and on average falls between the two, would suggest that there is a gradient in tensile properties across the

layer.

Comparison of the parallel and perpendicular stiffnesses yields large differences in the tangential zone, again in line with the results of Roth and Mow [123], however results for the deeper zones disagree with published results by showing little anisotropy. Although there are too few samples to make a valid statistical comparison, it may simply be the case that equine AC from the regions used in this project differ in composition to those from the bovine patellar. This variation in anisotropy was also documented by Verteramo and Seedhom [167]. The difference in tensile stiffness in the surface zone is 2.4:1 which is in line with results from Kempson et al. [124, 125] but greater than more recent investigations. This is likely due to the thickness of the surface samples - the 20 μm slices used in this work are wholly contained in the tangential layer whereas the thinnest published slices are 100 μm thick, and may include cartilage from the transitional layer.

It has been reported that regions of AC that experience lower peak loads are generally thicker than average [168, 169]. Such regions generally withstand a greater proportional amount of shear loading, which is likely to be the case for the thick palmar cartilage of the equine metacarpophalangeal joint, as the sessamoids articulate over the palmar region. Because the deeper zones have to resist smaller normal forces, less laterally isotropic collagen will be needed, meaning an arrangement with preferential orientation in the direction of greatest shear could provide the most efficient load support. This hypothesis is supported by the SAXS data obtained by [7] which show greater spreads in deep collagen orientation in thinner, higher load bearing regions. Data obtained for SAXS was taken with the source in line with the split line, and the thick palmar sample exhibited a narrow band of orientation in the deep zone as expected. The hypothesis is also supported by the PLM images of the thick transitional and radial zones, although the tensile test data is inconclusive. A follow-up study involving testing samples from the thicker regions of the proximal phalanx has been proposed, and preliminary images using second harmonic generation have shown an anisotropic distribution of collagen in the deep zone.

The toe region provides information about the initial reorientation and tensioning of collagen [129]. There has been no conclusive evidence documented in the literature showing differences in the toe region between parallel and perpendicular slices, which is surprising as collagen aligned perpendicular to the split line direction would be expected to undergo greater reorientation, and therefore give rise to a larger toe region (with respect to strain). Such a trend does not appear to be evident in the data collected in this investigation, as on average the data deviates from the linear trendline at around 8 % strain for both perpendicular and parallel samples. This unexpected behaviour calls into question the nature of the toe region, and has two possible solutions. The first is that the amount

of fibre reorientation is proportional to the angular displacement of the fibre prior to loading, meaning that fibres at large angles to the direction of strain simply reorientate more per unit strain than those close to parallel. The second is that the toe region is not related to the reorientation of fibres, and is just associated with the method by which the fibres take up strain. In order to test these hypotheses, a quantitative multimodal imaging study (similar to that performed by Sasazaki et al. [129]) of AC at varying small strains would need to be performed.

In summary, the work presented here provides tensile stiffness data which can be used to create a unique set of parameters for use in the FE model described in the previous chapter. Although a 1:4:12 normal strain ratio across the cartilage layers is exhibited in an unconfined compression, the ratio of lateral stiffness in this configuration is 11:6:3, suggesting the bulk modulus of the radial layer is significantly higher than the others. Clearly the validity of this data for use in a compression model depends upon the degree of lateral expansion. The value of 0.23 ± 0.10 for the ratio of axial strain to lateral strain in the deep zone of AC in an unconfined compression test obtained by Jurvelin et al. [109] would suggest that lateral fibres experience significant strain. Trends in the tensile properties and PLM images have shown that regions with different loading patterns have different collagen network arrangements to provide the best support and force distribution.

Chapter 5

Micromechanics

This chapter concerns the mechanics of the surface layer of cartilage at a microscopic level. Chapter 4 showed that the mechanical properties of the surface layer of AC vary considerably between locations on the joint, and that the arrangement of collagen fibres is anisotropic. The aim of this chapter is to determine the heterogeneous response of the surface layer of AC to tensile load using two photon fluorescence (TPF).

5.1 Introduction

TPF is a multiphoton imaging modality which is used to image materials which exhibit autofluorescence, or to which fluorophores have been attached. In articular cartilage (AC) TPF can resolve detail at depths exceeding $100\,\mu$m and, when tuned to the correct frequency, can be used to clearly image the chondrocytes, chondrocyte pericellular matrices (PCMs) and elastin fibres. The theory of TPF is explained in Section 1.4.1.

TPF is used in this chapter to investigate how strain propagates through cartilage at a microstructural level. There has been little reported work involving the imaging of fresh, unfixed samples under load, and no reported work at all on the role of the recently discovered [68, 66] elastin network in loaded cartilage. The motivation for pursuing this line of investigation follows from the previous chapter, to understand the microstructural response to applied load. The propagation of strain at a microscopic level influences the metabolism of chondrocytes due to mechanotransduction, as well as their nutrition due to the induced fluid flow.

The lack of similar work in the literature is due to the fact that until recently it has not been possible to obtain micron-scale detail of cartilage structure without either staining or fixing it. This means that it has only been possible to observe a sample at a single state

of strain. Although significant findings have been made using techniques such as SEM [170] and confocal laser scanning microscopy [129, 171], a non-invasive technique such as TPF is required to determine the propagation of strain, and the relative deformation of individual components of AC (defined in Section 1.1.2).

The topics of investigation in this chapter can be split into three categories:

- The propagation of strain through AC at a microscopic level, and the relative deformation of individual components.
- Variations of strain with depth.
- The interconnectivity of the elastin network with other components of cartilage, and its response to load.

To address these points, strips of AC from the equine metacarpophalangeal joint have been imaged at increasing strains using a specifically designed loading rig described in Section 2.2. The relative movement of cells and reorientation of elastin fibres is used to quantify the distribution of strain at two different length scales.

5.2 Experiment Outline

The method of imaging cartilage under increasing amounts of strain is explained in Section 2.3. Full thickness cartilage samples are imaged using two photon fluorescence at strains of 0 %, 10 % and 20 % using the nonlinear microscope. z-Stacks of 100 images taken at 1 μm intervals are obtained from the articular surface at each state of strain, and the location and orientation of chondrocytes and elastin fibres noted.

The arching effect of cartilage strips described in Section 4.1 limits the depth at which images can be taken in some samples, as the objective has a working distance of 210 μm which includes the 50 μm thickness of the coverslip. As a result, some stacks only include depths of up to 60 μm.

5.2.1 Cartilage Samples

Table 5.1 describes the location from which each cartilage sample was taken. All samples were taken from the same horse to allow comparison of regions of different weight bearing without influences from variations in lifestyle and pathology. The horse was a yearling (between 1 and 2 years old), at this age the AC is sufficiently developed that the collagen is arranged in a Benninghoff arcade structure [172], whilst yielding low background

Sample	Bone	Location on Bone
1	Metacarpal	Saggital ridge - palmar side
2	Metacarpal	Saggital ridge - middle
3	Metacarpal	Saggital ridge - dorsal side
4	Metacarpal	Cortical ridge - lateral edge
5	Metacarpal	Cortical ridge - midway between lateral edge and saggital ridge
6	Metacarpal	Cortical ridge - near saggital ridge
7	Phalanx	Saggital groove - palmar side
8	Phalanx	Mid point on lateral side

Table 5.1: Location from which cartilage samples were taken.

fluorescence, maximising the clarity of elastin fibres [66]. The regions from which samples were taken are listed in Table 5.1. The choice of regions is intended to provide a representative selection of loading patterns across the joint.

Samples were prepared in the manner explained in Section 2.1. Each sample was approximately 5 mm in the direction of applied strain, 700 μm wide and 300 μm to 500 μm thick. The axis of stretch was aligned with the direction of articulation *in vivo*. By qualitative observation, the samples varied considerably in their mechanical characteristics prior to being fixed to the apparatus, the most prominent difference being between the AC associated with metacarpal and that with the proximal phalanx. Cartilage from the proximal phalanx contained much larger internal stresses than the metacarpal, manifested by a significantly greater tendency to curl. Cartilage from this region also felt more stiff and brittle. As such, cartilage from the phalanx was more difficult to glue to the rig.

5.3 Results

The results of the investigation can be split into two topics: qualitative observations of the structure and deformation of the extracellular matrix (ECM) and cells, and quantitative analysis of the distribution of strain. The first subsection discusses the morphology of chondrocytes and their pericellular matrices, the arrangement, abundance and connectivity of elastin fibres, the presence of helical fibres at the lateral edge of the joint, and surface morphology. The second section focusses on the location of cells and the orientation of elastin fibres for the purpose of determining the distribution of strain at different length scales.

5.3.1 Observations of Cartilage Structure

Pulsed laser light tuned to a wavelength of 800 nm excites TPF primarily from elastin fibres and the pericellular matrices (PCMs) of cells. There is an homogeneous source of TPF from the ECM [33], the source of which is not fully understood, and this provides

contrast for chondrocytes, which appear dark. Elastin fibres appear as bright lines of fluorescence and are usually only one voxel thick. They branch several times over the width of a 250 μm $\times$ 250 μm image, and appear to be connected at PCMs and at nodes that appear as regions between 2 μm and 5 μm across with fluorescence slightly higher than background. Helical fibres were found in sample 4 which were up to 4 μm in diameter, with a diameter of helicity of up to 8 μm and period of helicity of 8 μm-10 μm. The presence of these fibres appeared to affect the morphology of the local chondrocytes. Lastly, the surface of articular cartilage appears to be covered in places by a fluorescent material that can be removed by wiping. The surface of cartilage under tension appears to corrugate in a manner similar to that reported by Sasazaki et al. [129].

5.3.1.1 Chondrocytes

Although individual collagen fibres are not visible under TPF, the collagen leaf structure described in Section 1.1.2.1 is indirectly visible by the arrangement of cells between leaves. Cells in the Ta layer are generally between 8 μm and 10 μm thick and 15 μm in diameter. They are arranged in layers one cell thick parallel to the surface. At a depth of approximately 70 μm the layered structure breaks down, with cells randomly arranged with depth and more spherical.

All cells appear to contain one or more bright spot which are approximately 0.5 μm to 1 μm across. One pixel at 512 by 512 resolution is a square of side length 0.5 μm so precise measurement of the size of these spots is not possible. Figure 5.1 (left) is an image from sample 2 at a depth of 50 μm which clearly shows several cells containing a single bright spot each. The other cells also display bright spots at different depths. Cells displaying a single bright spot account for 80 % to 90 % of the total cell population, with the rest having two or more, such as those in Figure 5.1 (right). It is difficult to ascertain in all cases whether a single cell contains more than one bright spot, or whether the cell has recently undergone mitosis and the bright spots are being shared between two cells. To determine this, an imaging modality which reveals the lipid bilayer around the cell (such as CARS) could be used.

The bright spots within cells appear to be larger in some cases towards the surface of the cartilage. This becomes the case increasingly in later stacks which suggests that growing spot size is an effect of exposure to the laser. In extreme cases the bright spots can become sources of cell ruptures whereby fluorescent material appears to be exuded from the cell into the surrounding matrix. These ruptures can cause the photomultiplier tubes (PMTs) to over-expose and prematurely terminate the z-stack, and prevent any further images from being taken without reducing voltage on the PMTs and thus losing detail. Once a cell has ruptured, the fluorescent material appears to flow until it occupies a volume

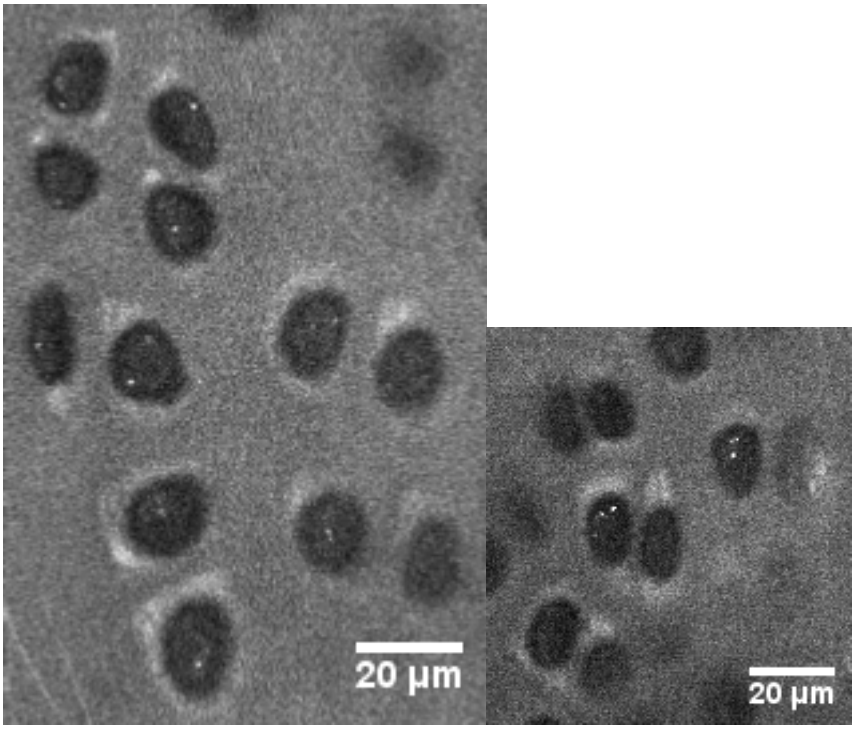

Figure 5.1: Bright spots in cells imaged using TPF. Both images are taken from sample 2 prior to stretching. The left image shows several cells with a single fluorescent spot, while the right image shows two cells with at least two fluorescent spots.

larger than the original cell. It is likely that cell rupturing is due to local heating caused by the absorption of laser light at the bright spots.

Another exposure-related effect exhibited by cells is the 'halo' whereby a ring of fluorescence greater than that of the rest of the cell appears approximately halfway along the cell radius, see Figure 5.2. The region inside the ring is sometimes lighter than outside the ring, especially near the articular surface where the halos are generally more vivid. The positioning of the halo in z is always towards the surface, and in most cases is still visible even when the focus has reached the top of the cell. The bright spots described above are always located on the halo.

The TPF exhibited by the PCM varies considerably between cells. All chondrons appear to exhibit greater TPF than background at a point around the circumference, but the intensity and spatial distribution of the signal around the chondron appears to vary greatly even between neighbouring cells. The circumference of the chondron covered by the fluorescent PCM is in some cases less than 10 % of the total, whereas in other cases the chondron can be completely surrounded. The average brightness of each PCM appears to vary with depth as well as location, being brightest near the surface. The PCM also appears to act as an anchor point for elastin fibres, as is seen in Figure 5.5, appearing in some cases to be connecting five or more fibres.

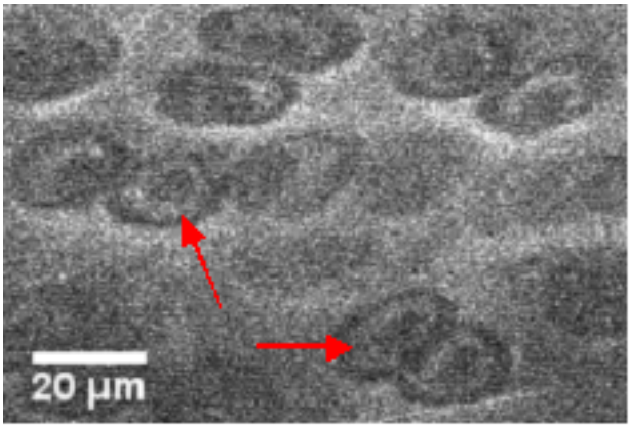

Figure 5.2: 'Halo' effect in surface cells from sample 6. The image is taken from the 10 % stretched stack so it is partly bleached. Cell halos (two of which are marked with red arrows) become more distinct with exposure time.

PCM fluorescence appears to be related to cell morphology, whereby non-circular cells display increased signal at the edge around their long axis (Figure 5.3). Neighbouring cells all appear to mirror this trend, with biases in fluorescence on the same sides irrespective of their morphology. The alignment of the PCM also often coincides with the alignment of the leaf-like structure of the cells on a larger scale.

5.3.1.2 Elastin

Elastin fibres are most abundant in the surface 3 μm of AC, but they can be found at the deepest point of image stacks, and have been reported to exist as deep as 175 μm from the surface [66]. Fibres usually appear only one voxel in diameter, making estimation of their diameter difficult but placing an upper limit of 0.5 μm. They are predominantly aligned parallel to the articular surface. Elastin fibres in the surface region all appear to be aligned parallel to one another, often with a second, less abundant layer of elastin fibres aligned perpendicularly to the surface fibres at a depth of approximately 10 μm. Trends in elastin fibre orientation below 10 μm vary widely, with some samples retaining order in elastin fibre orientation and others seeming randomly orientated.

The relationship between elastin fibres and chondrocytes appears to be quite complex. Some fibres, as mentioned above, appear to connect with cell PCMs whereas others appear to bend around cells before continuing in the same direction before - as though the cell were pushed into the fibre. In samples containing groups of clustered cells there is often a bundle of parallel elastin fibres between each group, and in some cases, particularly at the articular surface, a cluster of cells will be completely cocooned by fibres. See Figure 5.4.

Connectivity between elastin fibres is difficult to ascertain due to their sub-voxel diameter.

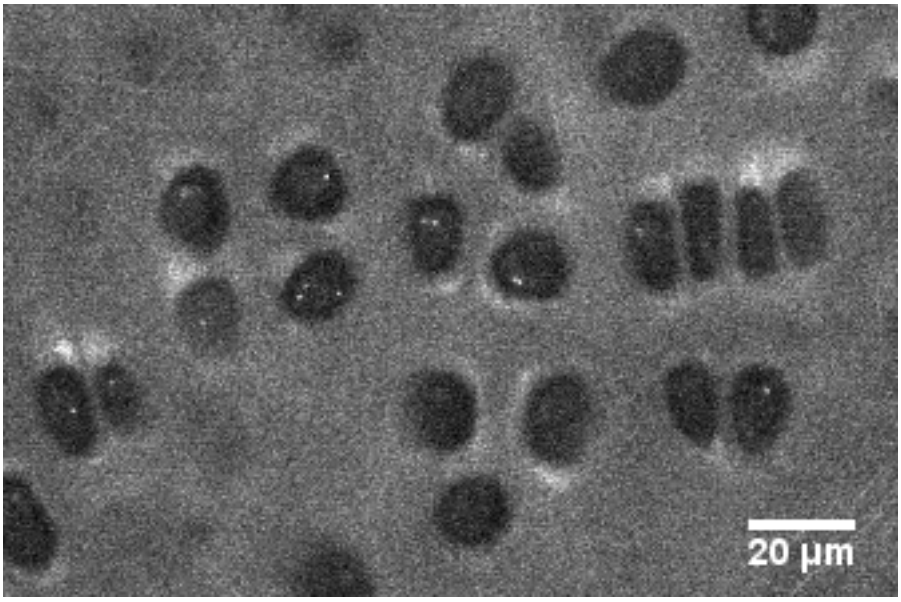

Figure 5.3: Bias in PCM fluorescence. Image taken from sample 2 prior to stretching. Pericellular matrices are clearly biased in the y-direction, as is some cell morphology.

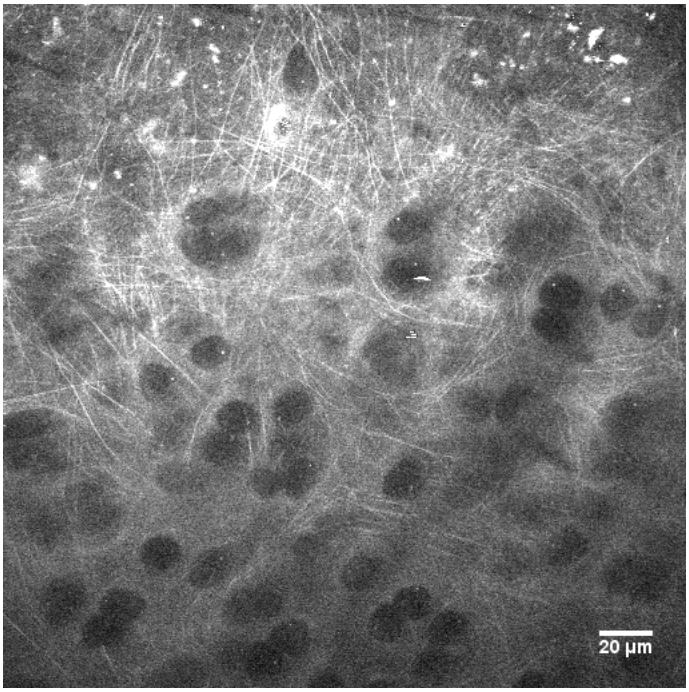

Figure 5.4: Elastin arrangement around cell clusters at the articular surface. Image taken from sample 7 prior to stretching.

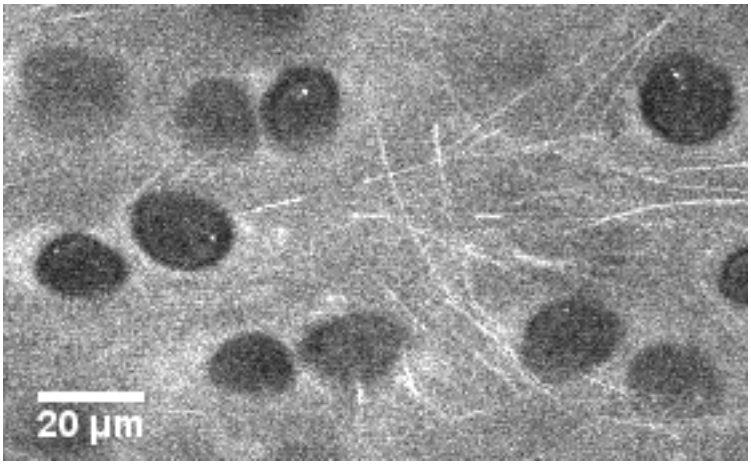

Figure 5.5: Connectivity of PCM with elastin fibres. Image taken from sample 3 prior to stretching.

It would appear however, that elastin fibres connect at nodes which appear as regions in the ECM with slightly higher TPF than background, as well as at PCMs as mentioned above, see Figure 5.5. Elastin fibres also appear to branch, with branching appearing to only occur in one direction, suggesting it may be possible to trace fibres back to their origins.

Trends in orientation throughout the depth of the AC appear to vary from sample to sample, with most samples exhibiting preferential orientations in the surface $3\,\mu$m, becoming increasingly randomly orientated with depth but retaining some preference to a depth of $60\,\mu$m. Surface fibres exhibit considerably less fluorescence than other fibres. Most elastin in the Ta region exists in the layers between cells, and follows the orientation of the leaf structure, suggesting a possible relationship with collagen fibres. In samples less abundant in elastin, fibres often appear to come together in channels which pass around and between groups of cells. Elastin in most samples becomes completely disordered at a depth which coincides with the bottom of the Ta layer.

In samples which have exhibited high compressive y-strain when stretched in x, fibres with prestretch alignments near to vertical have been seen to crimp suggesting that they have lost tension, see Figure 5.6. These regions of the cartilage have experienced a local y-strain of $-36\,\% \pm 2\,\%$, and an x-strain of $8\,\% \pm 2\,\%$ in Figure 5.6, which suggests the downward forking fibres are experiencing a length strain of $-28\,\% \pm 4\,\%$. At a strain of $-20\,\% \pm 4\,\%$ (not shown) there is no evidence of crimping, suggesting that the elastin fibre is strained by between $25\,\% \pm 5\,\%$ and $39\,\% \pm 8\,\%$ in the absense of external loads due to prestress *in vivo*.

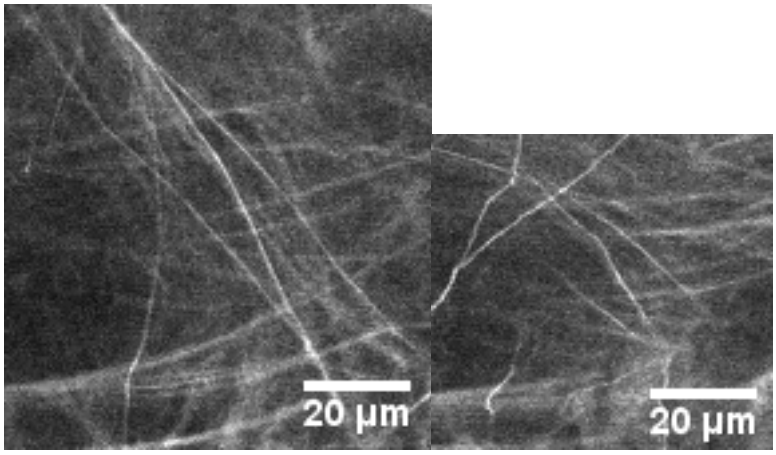

Figure 5.6: Elastin crimping

5.3.1.3 Helical Fibres

The consistency of sample 4 was considerably different to the rest of the samples, containing fibres not found anywhere else (Figure 5.7). Fibres appear to be helical, with periodicity of $3\,\mu$m to $8\,\mu$m depending upon the thickness of the fibre. The thickness of the fibres is considerably greater than elastin fibres found elsewhere in the joint, with fibre diameters of up to $4\,\mu$m and a diameter of helix curvature of up to $8\,\mu$m. Fibres are arranged in bundles up to $30\,\mu$m thick, in which fibres appear to have similar periodicities. The fibres do not appear to show an overall trend in periodicity based on their thickness, so thick fibres appear more tightly coiled than thin ones. The fibres branch into smaller helical fibres in places, similar to a frayed rope, with the average length over which a fibre covers before branching appearing considerably greater than that of elastin fibres. The thickness of the fibres suggests that they are not elastin, and are likely to be collagen. Their fluorescent properties and helical nature suggests that they are not type II collagen.

The sample does not only consist of helical fibres, there also appears to be an elastin network exhibiting the same trends as described earlier in the subsection. The elastin network is most abundant in the surface $4\,\mu$m, below which the helical fibre network dominates. Helical fibres can be resolved down to a depth of $55\,\mu$m, and it is unclear whether this is a natural boundary for the presence helical fibres, or if there is simply too much scattering to resolve them below this point. Elastin fibres can be resolved from the bottom of the stack, which is at a depth of $75\,\mu$m. Elastin fibres can be seen to be contained within bundles of helical fibres in places, but it is unclear whether there is any connectivity between the two fibre types.

Orientation of helical fibres favours the y-direction (perpendicular to the direction of articulation), but there are a number of non-helical fibres which are the same thickness

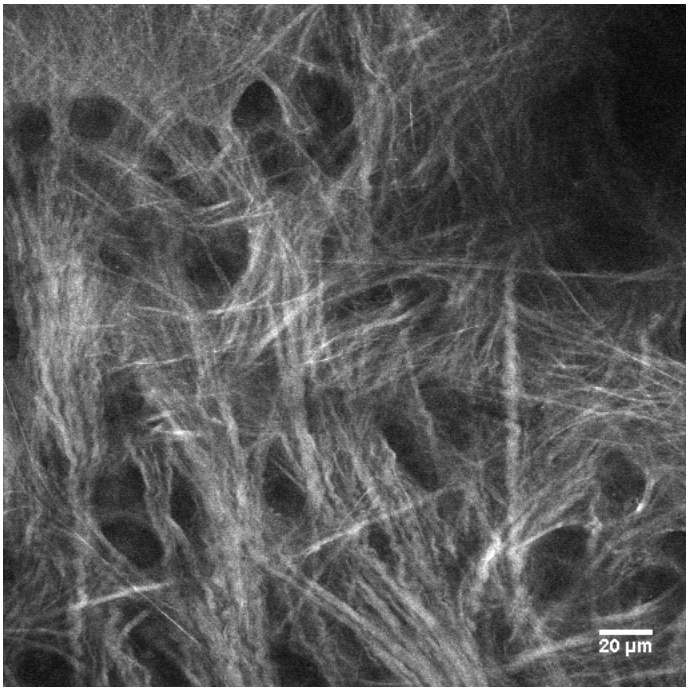

Figure 5.7: Helical collagen fibres

and same fluoresence intensity as helical fibres, which favour the x-direction. These fibres exist predominantly in the top 10 μm of the sample but can still be seen as deep as the lowest helical fibres.

The presence of helical fibres appears to influence the morphology of adjacent cells. Groups of cells are much more tightly clustered between the fibres, appearing in some cases as though they are in fact in the same chondron. Clusters like this appear to contain up to five cells.

5.3.1.4 Surface Morphology

Most samples display regions of high fluorescence at the surface (Figure 5.8), which need to be avoided when taking z-stacks to prevent PMT overload. It is unclear whether the material exhibiting this fluorescence is native to the surface of cartilage (potentially some deposited lubricant from the synovial fluid), or if it is a foreign material which has stuck to the articular surface during sample preparation, or cell debris. TPF imaging of separate, fresh cartilage samples from the same location which have undergone no preparation yields considerably less surface fluorescence, suggesting the fluorescence may be an artifact of the preparation process.

At high strains the surface of some samples appears to corrugate. These corrugations can be up to 10 μm deep and the peak-to-peak displacements are between 20 μm and

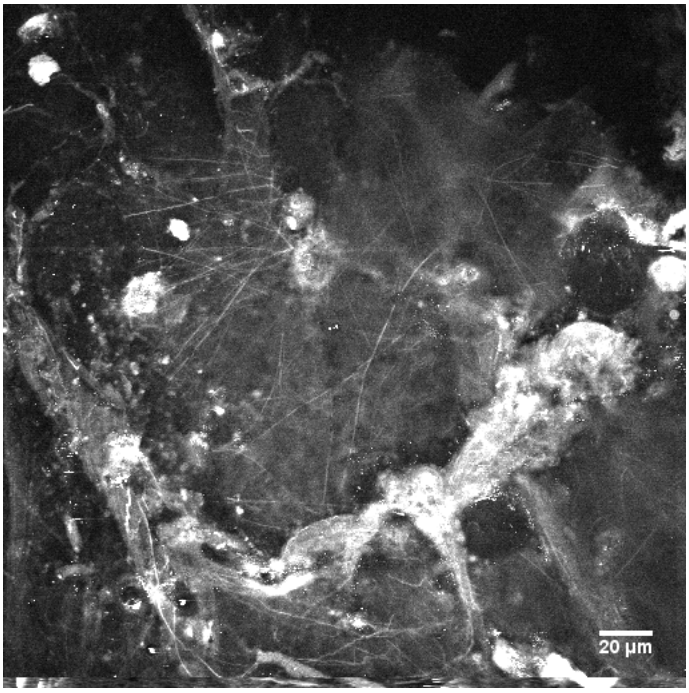

Figure 5.8: Unusual surface fluorescence.

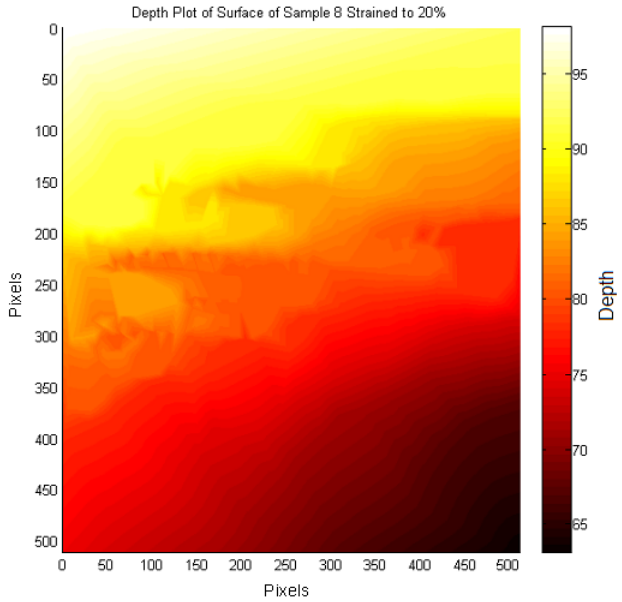

Figure 5.9: Surface height plot of the articular surface of sample 8, illustrating surface corrugation and sample rotation. Ridges can be seen along the lines $y = 170$ and $y = 220$ (pixels), depicted by arrows. The sample has rotated about the axis of strain, resulting in the surface at the top of the image being $30\,\mu$m higher than that of the bottom.

50 μm. These corrugations are morphologically similar to the ridges seen by Sasazaki et al. [129] using SEM, which were associated with collagen fibres under tension. Figure 5.9 is a reconstructed surface map of sample 8 that clearly shows a periodic corrugation over some of the surface. The method by which this surface plot was made is described in Section 5.3.2.1. This map contains surface details which are smeared out in the maps used for depth analysis, however the lack of uniformity in the distance in x and y between each marked point will also result in extra erroneous small-scale details which can not be avoided. When a tensile load is applied to a sample, it will often rotate by a small amount about the axis of strain. This is shown in Figure 5.9. Some samples also appear to curl inwards slightly towards the articular surface, around the axis of stretching. The degree of curvature and rotation varies between samples, with the largest angular displacement from the imaging plane attributed to sample 13 at an angle of 25°. This curling behaviour has been documented by Roth and Mow [123], who attributed the behaviour to the inhomogeneity of the tissue. There is a slight bias for prestretched images of approximately 3°-4° suggesting that the sticking edges of the paddles on the stretching rig were not perfectly parallel to the base. The paddles were fixed in the same position for all samples and not removed nor loosened between experiments. The samples have rotated in both directions about the axis of stretching, suggesting that this twisting behaviour is due to anisotropic stress distributions within the sample and not simply a systematic error attributable to the rig.

5.3.2 Quantitative Analysis of Strain Distribution

The ability to image cells and elastin fibres simultaneously presents an opportunity to measure strain at two lengthscales. The strain at the larger of the two lengthscales is calculated by determining the relative movement of cells and finding the average intercellular strain at different depths. The strain at the smaller lengthscale is calculated by determining the change in angle of individual elastin fibres, and calculating the required strain in x or y to induce such a change in angle (see Figure 5.10). The strains at large and small lengthscales are referred to as the *intercellular* and *specific* strains, respectively, as the large scale strain is calculated from intercellular deformations, and the small scale strain is specific to individual elastin fibres. Comparisons between the two distributions of strain are made at the end of the section.

5.3.2.1 Image Analysis

In order to quantify the strain across the samples, the Cartesian coordinates of the centres of selected cells were found, as well as vectors defining the direction of selected elastin fibres at specified points.

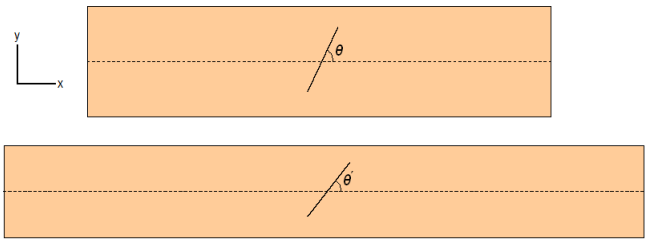

Figure 5.10: Illustration of the change in orientation of elastin fibres θ in a strained sample, which can be used for calculating strain. The solid line represents an elastin fibre and the dashed line represents the central axis of the sample, along which tensile strain is applied. The top image represents the unloaded cartilage, and the bottom image represents the cartilage under a tensile strain.

Cells were selected based on clarity and location within the stack. Heterogeneity in the distribution of cells dictated that it was not possible to take sample evenly distributed with depth, but effort was made to ensure that gaps between cells in z were as regular as possible. Cells are usually arranged in pairs within chondrons, and every cell within a selected chondron was labelled. This is useful for investigating possible variations in intra- and inter-chondronal strain.

It was found that despite being able to locate cells using image manipulation software, the associated error was greater than performing the same procedure by hand. This was due to the considerable differences in the appearances of the cells and elastin fibres, the most detrimental being due to photobleaching in the strained stacks. It was possible to repeatedly find a preselected point within a cell to within ± 1 pixel ($\pm 0.5\,\mu$m) by hand as the cells have features such as variation in brightness of the PCM around the circumference, as well as bright spots which can be used as reference points.

Elastin fibres are selected based on the same criteria as the cells. Locating elastin fibres in bleached images is more difficult than locating cells due to the lack of features to distinguish them from background fluorescence. In light of this, less elastin fibres are labelled than cells. This does not, however, pose a problem for analysis as the quality of the strain data for each fibre is not dependent upon the quantity of other local fibres.

Selected fibres are labelled at points where they are straight, so that only two points are needed to define the direction vector. This also means that the importance of labelling the exact same points in each stack is lessened, as any two points on the line sufficiently far apart can be used.

The method by which depths of cells and elastin fibres were calculated is non-trivial. Surface maps of the cartilage were plotted by first marking points on z-stacks that were on the articular surface. These surface points were marked approximately every 3 microns in z, and the (x, y, n) locations were recorded in a table using a macro in ImageJ, where n refers to the image number in the stack. Typically around 300 points were recorded

per stack, increasing if the surface topology was complex. The desired outcome was a 512×512 matrix defining the surface z-value for each pixel, so an interpolation was required.

To achieve this, a uniform 512×512 grid was meshed using the MESHGRID function in MATLAB. The GRIDDATA function was then used, which fits a surface to the original data and uses a linear Delaunay triangulation method to interpolate the surface at each point on the grid, resulting in a 512×512 grid of z-values, referred to as the surface grid. Depths of points of interest (POIs) can then be found by simply querying the surface grid matrix at the index $(i, j) = (x, y)$, and subtracting the slide number of the POI from this value. This method is considerably more accurate for finding depths than simply using the slide number, as twisted samples can sometimes be up to $30\,\mu$m deeper at the top of the image than at the bottom. Smaller scale surface irregularities (of the order of $10\,\mu$m) are not included when marking surface points, as they are unlikely to contribute towards depth-based variations in the sample.

5.3.2.2 Intercellular Strain

Cells were first split into four groups according to depth. The four groups were approximately equally spaced throughout the depth of the stack. Group sizes were roughly equal and contain 5-10 cells each depending upon the number of labelled cells in the stack. Strain data were calculated by finding a 'centre of gravity' (CoG) of the cells in each cell group and finding the ratio of displacements from the CoG in the prestretch and stretched cases.

$$\varepsilon_i = \frac{x_i' - \frac{1}{N}\sum_{i=1}^{N} x_i'}{x_i - \frac{1}{N}\sum_{i=1}^{N} x_i} - 1 \tag{5.1}$$

Here x_i and $x_i\prime$ denote the location of the ith cell in x or y in the prestretch and stretched cases, respectively. N denotes the number of cells in the group. This method for calculating the strain assumes that chondrons and surrounding ECM deform as a homogeneous, linear elastic material, i.e. there is no translational/relative movement. If a chondron does exhibit translation relative to the other chondrons then cells within that chondron will have different strain values to one another, this difference being inversely proportional to the distance from the CoG. Preliminary results showed that there is some degree of relative movement between chondrons, which will lead to errors inversely proportional to the distance from the CoG when calculating the strain. A filtering step was therefore introduced to the code which balanced accuracy with quantity of data by excluding cells

that fell within a threshold distance from the CoG at any stage of stretch. It was found that a threshold of 7.5 μm (15 pixels) from the CoG sufficiently reduced errors, whilst only reducing the data sample in size by approximately one third.

Group strains are then calculated by finding the average strain value over the cells for each group. Figures 5.11 and 5.12 detail the results found using this analysis technique.

This technique yielded sensible x-strain data for all samples. Samples 4 and 6 were insufficiently clear in the 10 % strain stack at depths below 50 μm to resolve cells clearly, and are thus either missing a data point, or have their data points concentrated at shallower depths. As the 20 % data was taken after the prestretch and 10 % data, the effects of photobleaching were more severe and thus more results were unobtainable from deeper regions of the samples.

The key result shown by this data is the repeatable trend across all samples of a minima in average intercellular strain at depths between 25 μm and 50 μm. This is followed by a distinct rise in strain. Note that the depth values on the x-axes are measures of the *prestretch* depths of the cells.

There is clearly a wide variation in the total amount of strain experienced across the stack in each sample. Samples 2 and 7 display an average intercellular strain greater than 10 % in the first data set, whereas the intercellular strains in other samples are significantly less. This could be due to variations in sample composition and orientation leading to varying strains at the surface, errors in judging whether a cartilage sample is taut prior to initiating an experiment, or a weakness either in the sample or the cartilage-paddle interface.

The most striking result from the 20 % strain data is from that of sample 5, in which cells around a depth of 45 μm exhibit a negative strain, suggesting the cartilage at this depth has contracted. Manual observations of the z-stack verify this result. The sample displays the lowest overall average intercellular strain, so it is not clear whether this trend would have continued at higher applied strains.

The overall trends of the two data sets are similar, see Figure 5.13 for a direct comparison between the 10 % and 20 % results.

The y-strain data contained more gaps than the x-strain data due to the CoG exception rules described earlier. As the cells are converging, a greater number of reference points fall within the threshold value for exception. This was particularly the case for surface cells in samples 1 and 3. Sample 4 was subject to photobleaching, preventing cells from being resolved below depths of 50 μm. More data points were lost in the 20 % case, again due to bleaching. Sample 1 only has one viable data point, at an extremely high strain of 50 %. All other samples have at least 3 data points, apart from sample 7 which was

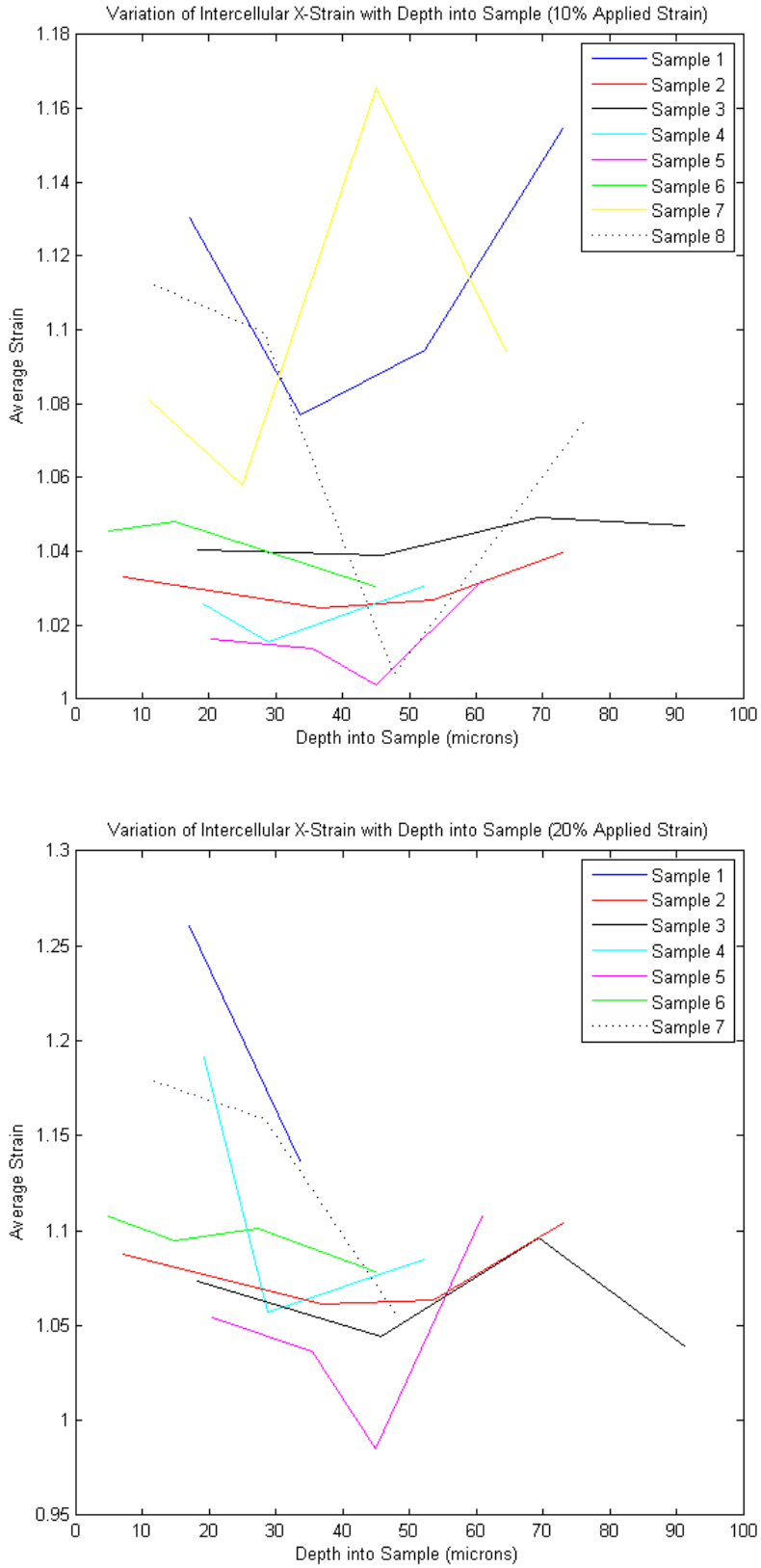

Figure 5.11: Intercellular strain in x when sample strained by 10 % (top) and 20 % (bottom).

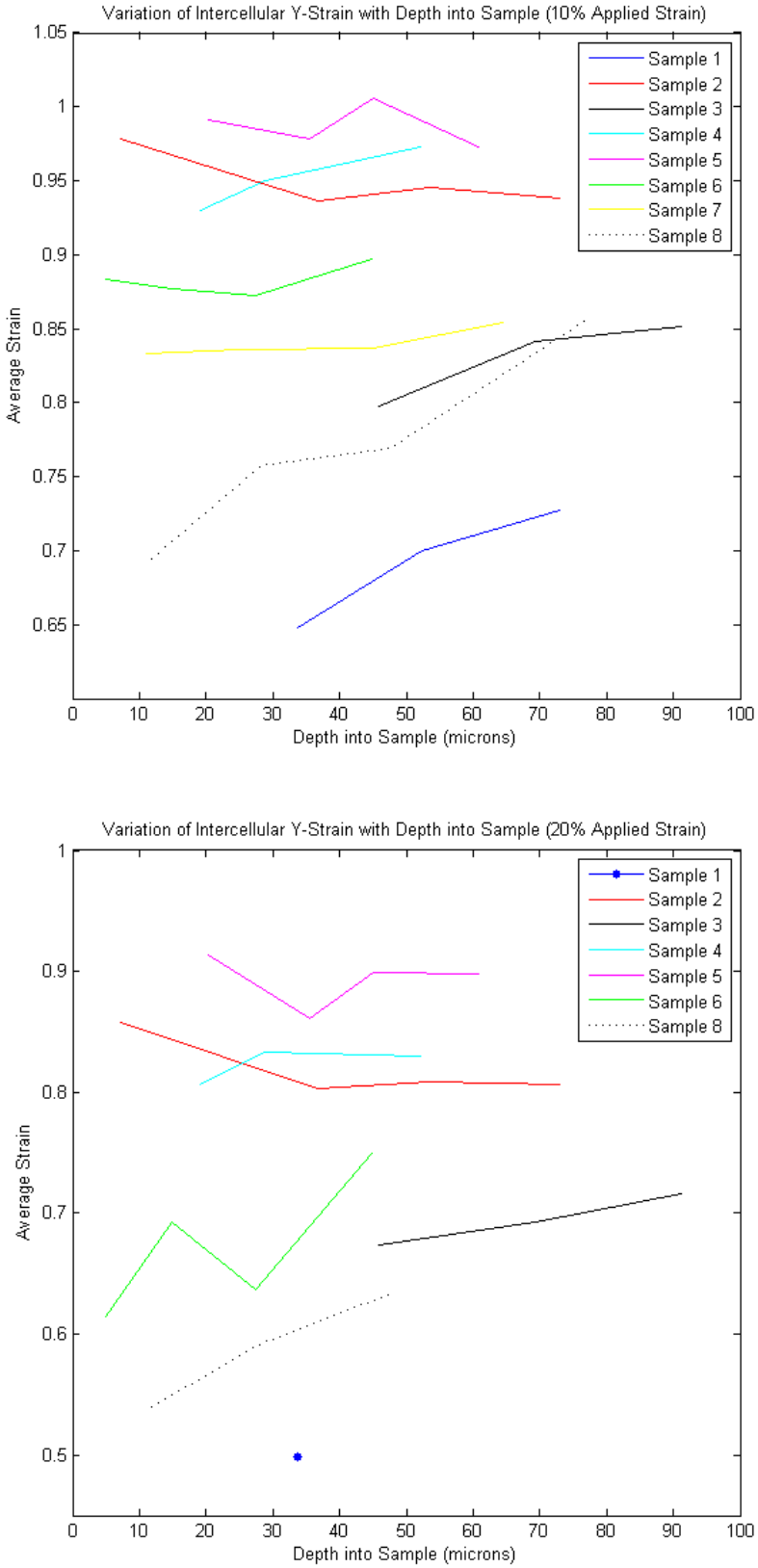

Figure 5.12: Intercellular strain in y when sample strained to 10% (top) and 20% (bottom).

omitted entirely due to photobleaching and twisting in the sample.

The overall average y-strain values are surprising considering the associated x-strain values. Samples which have been strained by 12 % in x have contracted by up to 30 % in y. There is a correlation between the amounts of strain in x and y suggesting that trends between the two may be possible to compare. There appears to be a total strain dependent relationship, whereby samples which have experienced large average negative strains appear to contract most near the surface, whereas samples which have strained less than 10 % in y appear to contract most at the deepest point. Sample 5 appears to expand in y at its 3rd data point, mirroring the dip in x-strain on Figure 5.11.

Trends in the intercellular y-strain at 10 % and 20 % total strain appear to be similar. A direct comparison of the data for the two states of strain for each sample can be found in Figure 5.14. The unusual behaviour in sample 5 appears to have not been mirrored in this case, despite its negative x-strain.

5.3.2.3 Specific Distribution of Strain

In this subsection the orientation change of selected elastin fibres at specific points are used in conjunction with intercellular strain data from cell movement to estimate values of strain at that point. The linear x-strain:

$$\varepsilon_x = \frac{x'}{x} - 1 \tag{5.2}$$

at a specific point in the ECM can be calculated using the reorientation of an elastin fibre and the intercellular y-strain at the depth of the point, assuming there is no relative movement between the elastin fibre and surrounding matrix, using the following equation:

$$\varepsilon_x = (\varepsilon_y + 1)\frac{\tan\theta}{\tan\theta'} - 1 \tag{5.3}$$

where θ is the azimuthal angle of the fibre (Figure 5.10). Here the x-strain ε_x is determined at a specific location (the position of the elastin fibre in question) assuming the y-strain ε_y is equal to the intercellular strain (Equation 5.1). Likewise the y-strain at a specific point can be determined from elastin reorientation and the intercellular x-strain. As the intercellular strain data is discontinuous, with only up to 4 data points, polynomials $P(z)$ are fitted to the intercellular x- and y-strain data with $o(P) = n-1$ where n is the number of data points for a given sample in a certain state of stretch.

Inclination ϕ (the fibre angle with respect to the xy-plane) was also measured, but due to the fact that most elastin fibres are within 5° of tangential, the error in z ($\pm 2\mu m$)

is several times greater than the variation in the z-position of the fibres. The resulting errors in ϕ are therefore unacceptable so the results are omitted.

Figures 5.13 and 5.14 compare the intercellular strain data for each state of strain and specific strain values for selected elastin fibres. Patterns in intercellular strain at 10 % are repeated and emphasised at 20 % (see Figures 5.11 and 5.12), whereas the distribution of specific strain appears to be more random.

Mean values for specific x-strain do not exhibit significantly different values for each state of sample strain. Such a random distribution can be the result if the sample exhibits either or both of the following properties:

1. The distribution of strain at lengthscales of order 10^{-4}m and below are highly heterogeneous.
2. The elastin fibre network moves relative to the other constituents of the ECM.

The y-strain data again shows roughly similar behaviour in the 10 % and 20 % intercellular strains, suggesting trends in the distribution of strain can be believed. The specific strain data also appears to loosely follow the intercellular strain data, with means significantly far apart from each other, and close to mean intercellular strain values. Errors in specific strain are greater than the intercellular strain, as they are dependent upon calculations of the original angle of the fibre and the intercellular strain, and are inversely proportional to the data in Figure 5.15. For example, a fibre which is perfectly vertical should not exhibit any angular displacement when the sample is stretched, so a translation or error induced change in calculated orientation will yield an erroneous specific ε_x from Equation 5.3 of infinity.

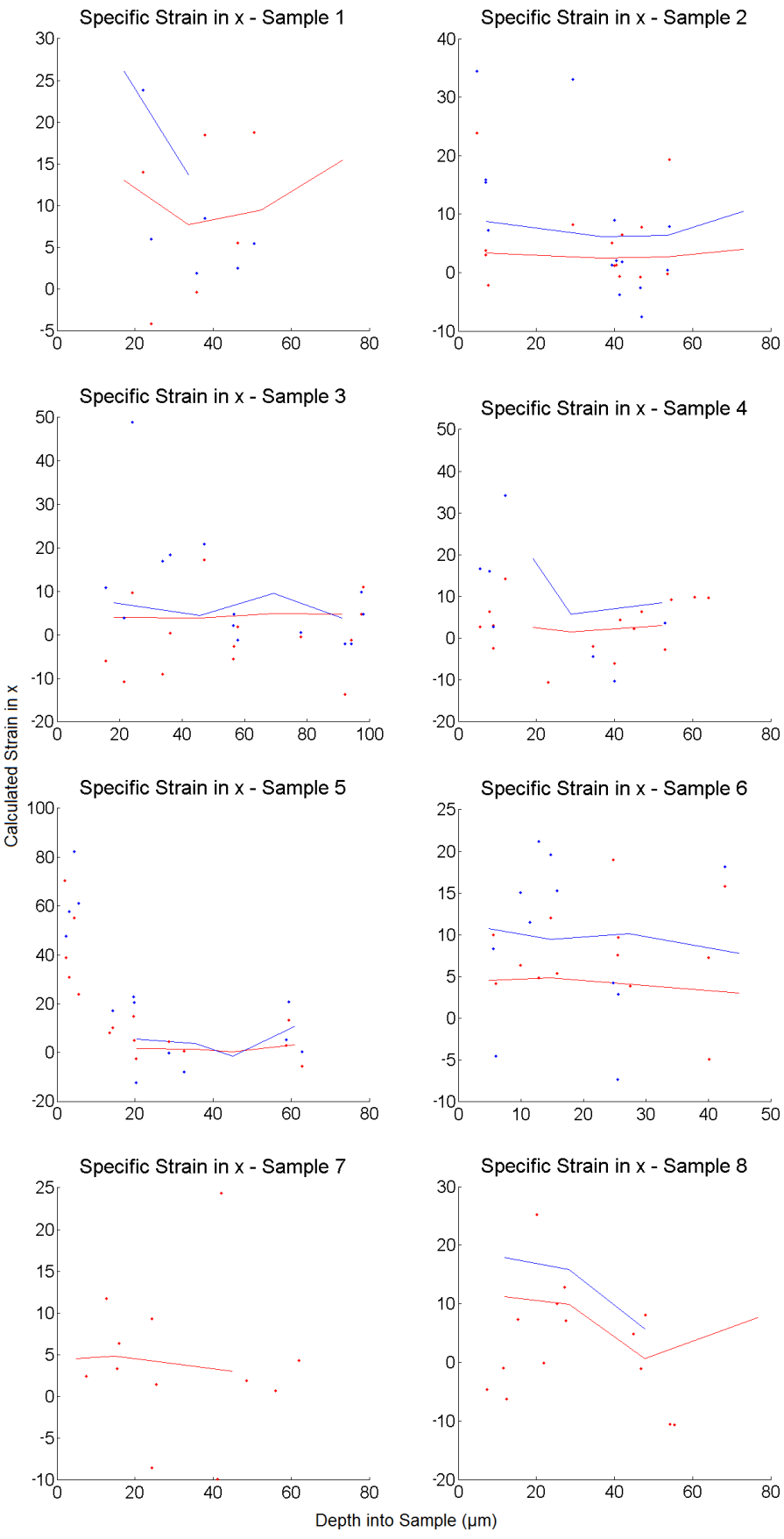

Figure 5.13: Comparison of 10 % and 20 % intercellular x-strains (solid lines) and related specific strains (points).

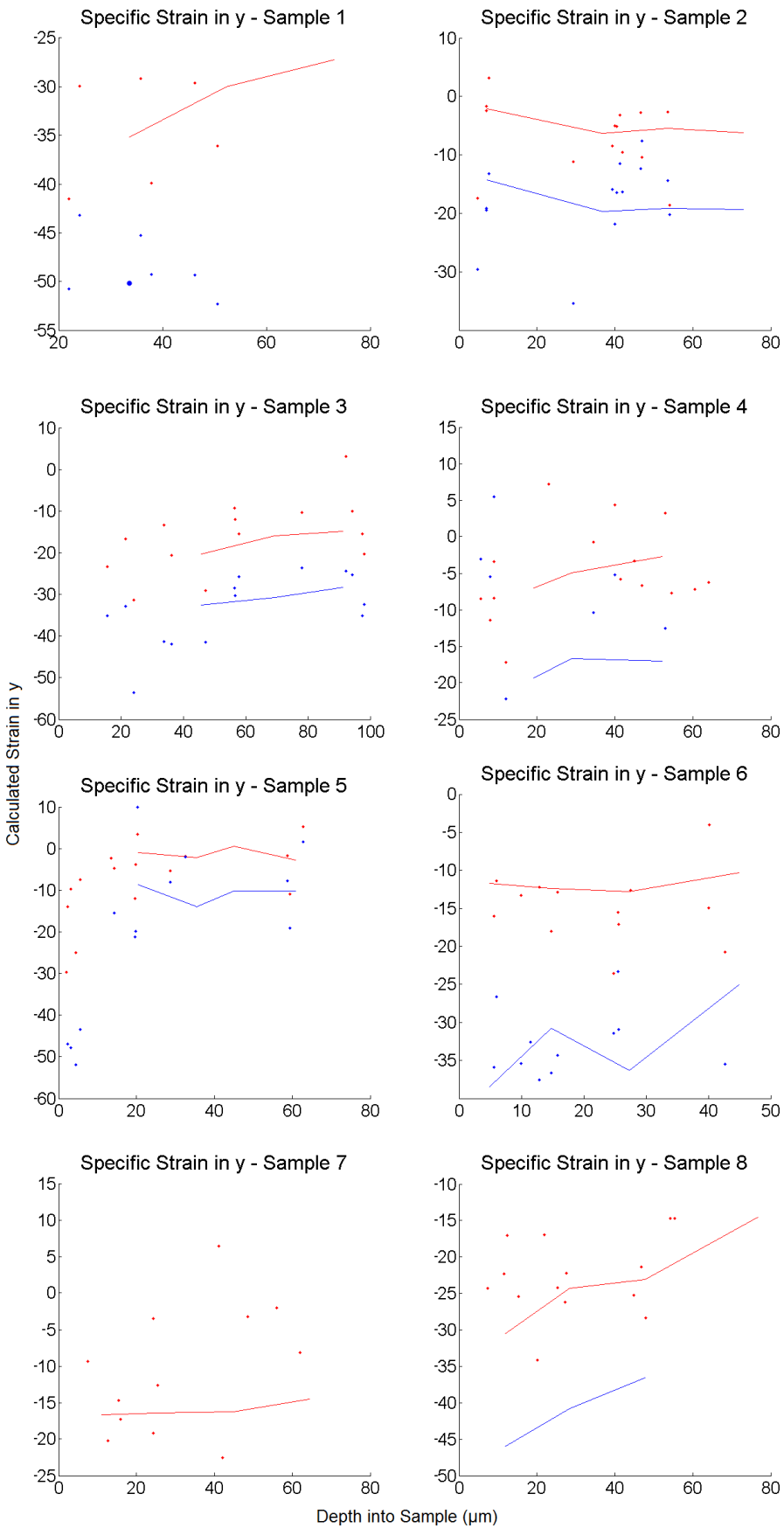

Figure 5.14: Comparison of 10 % and 20 % intercellular y-strains (solid lines) and related specific strains (points).

The distribution of angular displacements of elastin fibres has also been investigated. A single fibre laying in the xy-plane will undergo a change in orientation $d\theta$ when deformed in x and y by dx and dy, respectively, as defined by:

$$d\theta = \left(\frac{\partial\theta}{\partial x}\right) dx + \left(\frac{\partial\theta}{\partial y}\right) dy \tag{5.4}$$

where:

$$\frac{\partial\theta}{\partial x} = \frac{-y}{x^2+y^2} \qquad \frac{\partial\theta}{\partial y} = \frac{x}{x^2+y^2} \tag{5.5}$$

Equation 5.4 can be solved iteratively to find the relationship between $d\theta$ and θ for finite strains (Figure 5.15). These graphs are based on a number of assumptions, including that:

- The cartilage behaves in a linearly elastic manner when strained, and is homogeneous and isotropic in x and y.
- There is no slip between the elastin and ECM (i.e. every point on the fibre maintains the same ECM neighbourhood).
- Force is transduced across the fibre as though it were not there.

The graphs detail trends for materials with Poisson's ratio between 0 and 0.5 as most materials fall within these bounds. Most biological materials are regarded as being close to incompressible ($\nu = 0.5$), and this is also true for cartilage under instantaneous loads, however, in the compression regime at equilibrium cartilage has been shown to have a Poisson's ratio between 0.06 and 0.18 [112]. There has been little work documenting the Poisson's ratio of AC in tension, however Woo et al. [127] documented large lateral contraction during tensile testing, suggesting the Poisson's ratio in tension may be greater than 0.5.

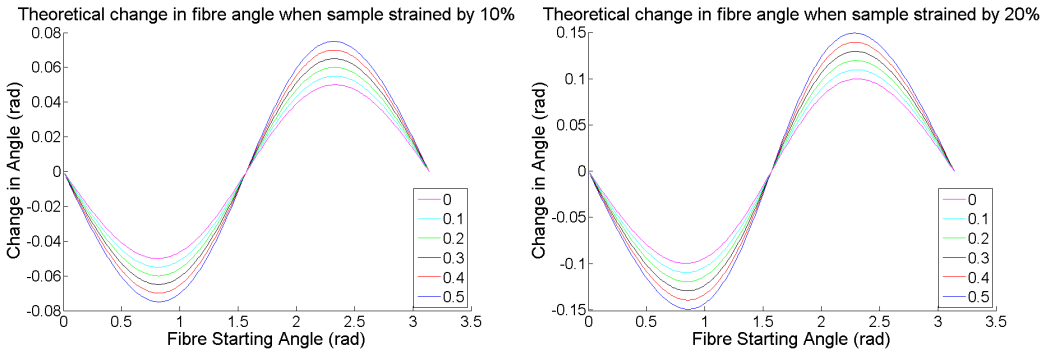

Figure 5.15: Theoretical angular displacement of a single fibre embedded in a homogeneous material which is then strained to 10 % (left) and 20 % (right). The sample is assumed to exhibit linear elastic strain behaviour. The legends refer to values of Poisson's ratio.

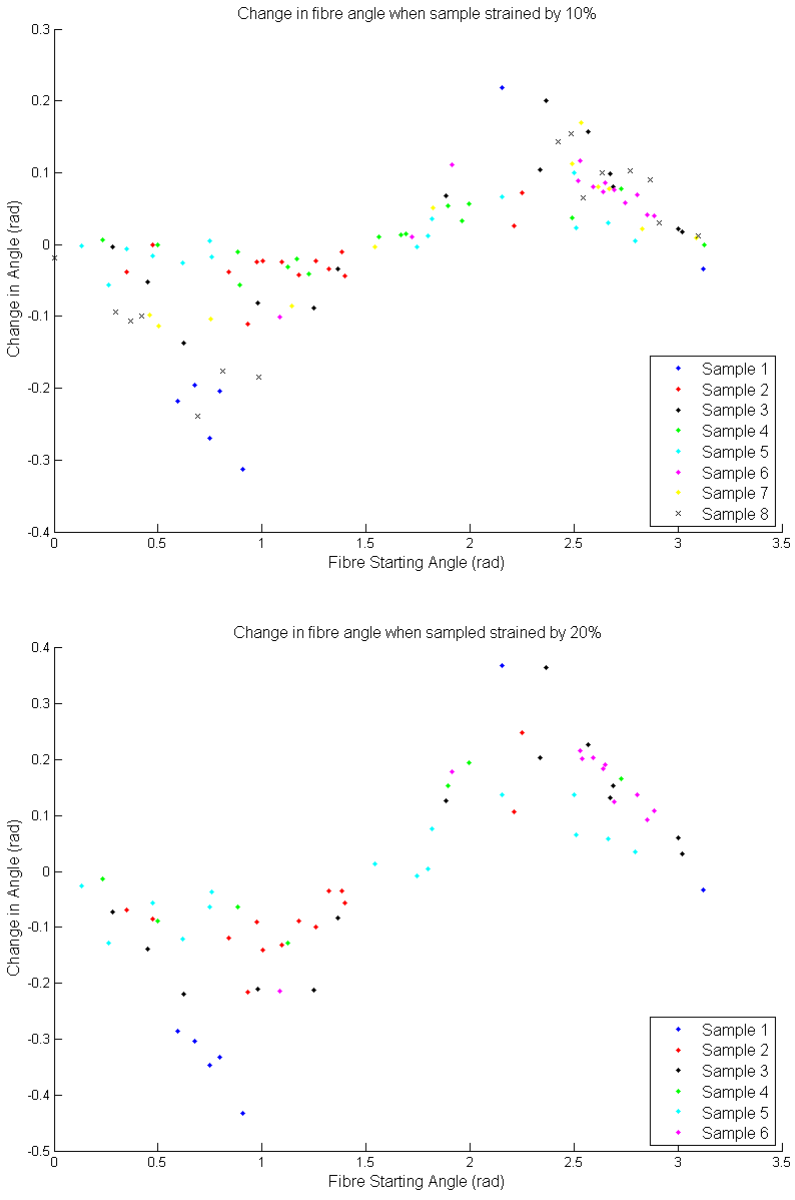

Figure 5.16: Angular displacement of elastin fibres in stretched cartilage samples.

The distribution of measured elastin fibre angular displacements is shown in Figure 5.16. The rough shape of the predicted trend is clear, however there is clearly considerable variation. The main contributor to the spread in this graph is the variation in applied strain to each sample. It is clear from the previous subsection that the total applied x-strain varies considerably, as mean values vary between 1 % and 11 % in the 10 % intercellular strain data, and 5 % to 20 % in the 20 % intercellular strain data. This prevents any meaningful statistical analysis from being performed on the data in bulk, but conclusions can be drawn from individual sample data. There is insufficient data for each sample for individual comparison with with theory, but there are still some striking results.

The amount of angular displacement correlates with the intercellular strains in x and y as expected. There are, however, notable exceptions to this rule, suggesting that there are heterogeneous contributions to the strain. This data is useful alongside that of Figures 5.13 and 5.14 as it also includes data for near-horizontal and near-vertical fibres which were filtered out due to large associated errors in calculating strain. The behaviour of data at $\theta = 0$ and $\theta = \frac{\pi}{2}$ is of particular interest as any data points at these angles which do not have an angular displacement close to 0 are evidence of elastin fibre reorganisation.

The size of the elastin angular displacements are considerably greater than that shown in theory. The strain data already shows that the cartilage exhibits unusual behaviour in the ratio of strain in x and y, and this is verified by elastin reorientation data. In order for a fibre embedded in a homogeneous medium (with assumptions detailed earlier) to undergo the larger orientation changes detailed in Figure 5.16, the medium would need to have a Poisson's ratio of significantly greater than 1.

5.4 Discussion

The aim of this work was to investigate the effect of externally applied strain on the deformation of AC at small scales, and the potential role of elastin in the articular surface. To achieve this, TPF image stacks were taken of samples stretched in the tensile regime at 3 stages of strain. These stacks of images resolve elastin fibres, chondrocytes and PCMs, and analysis of these images provides detail about the depth dependent distribution of strain at the scale of $\sim 200\,\mu$m (relative cell movement) and $\sim 20\,\mu$m (elastin fibre reorientation). It should be noted that by the nature of their calculation, the small scale strains are not direct strain measurements, and should be viewed more as a test of whether the larger scale trends apply to the smaller scale.

The imaged cartilage regions have clearly been exposed to very different amounts of strain. There are a number of potential reasons for this:

1. The lack of force measurement resulted in errors when judging whether the sample is taut.

2. Mechanical failure occurred in another region of the sample.

3. Failure or creep in the adhesive between the sample and the rig.

4. Variation in the composition of samples leading to differences in the surface strain.

The contribution of each point is likely to be nonzero, but variable in significance. Firstly, the errors described in 1. will contribute at most to a variation in applied strain of $\pm 2\%$. Failure in the sample or adhesive would be noticed during imaging, as the x-location of the focus would move relative to the sample. When a sample is strained, there follows a period of stress-relaxation when the focus moves slightly across the sample, but this has a characteristic time and lengthscale which is easily distinguished from failure. Creep caused by adhesive is a possibility, but a series of stretching experiments performed under a normal light microscope have shown that the adhesive holds the sample firmly up to and beyond the strains described in this chapter.

Most of the samples exhibited a larger magnitude of strain in y than they did in x, suggesting that they are shrinking in volume when loaded ($\nu > 1$) . It has been shown that collagen fibres reorientate under tensile loads [129], and data from Chapter 4 documents the associated effect on the mechanical properties. It is possible that the reorientation and straightening of collagen fibres explains the large contraction in y. It has been shown that composite and/or anisotropic structures can have Poisson's ratios greater than or equal to 1 (see e.g. [173]), and this type of behaviour has been documented for AC under tension previously [127].

The large scale y-strain is used in conjunction with the angular displacements of elastin fibres to calculate the small scale x-strain data, which exhibits high spread and little correlation. Errors in the specific x-strain data are compounded by the additional artifact of sample twisting. Twisting can lead to sample inclinations of up to 10° from the y-z plane and cause samples to appear up to 2% more strained in y. The poor specific x-strain data suggests that the y-contraction associated with straightening collagen fibres is very heterogeneous and therefore contains too much variation to be useful for calculating small scale x-strains in the manner described earlier.

The results show a clear heterogeneity in strain at the smaller scale. The variation in strain at the larger scale is considerably smaller than at the smaller scale, and demonstrates repeatable trends across samples. The distribution of strain at the small scale appears to loosely fit the large scale strain trend for each sample in y, but an insufficient number of points lay on the trend line within error to conclude that the trend must be the

same. Instead it must be concluded that there are cellular level variations in the strain distribution caused by the heterogeneous composition of the cartilage.

5.4.1 The Elastin Fibre Network and its Response to Load

The reorientation of elastin fibres is of key interest in this work, and some useful conclusions can be drawn from the data. Firstly, it is clear that although the proteoglycan within cartilage has been shown to behave in a fluid manner over long timescales, the elastin network does not show any relative movement in relation to the rest of the cartilage visible under TPF. This conclusion can be derived from the behaviour of elastin fibres close to to 0 and $\frac{\pi}{2}$ radians, as at these angles the theory states that there should be negligible orientation change if elastin fibres maintain their position relative to the neighbouring ECM. If there were any significant changes in orientation at these angles, it would suggest that connected fibres were applying unequal forces to the fibre in question, and that the fibre is free to move relative to the other constituents of the ECM. It is acknowledged that there are relatively few data points at these orientations, so statistically this conclusion is weak. Of the 11 data points taken within 0.2 radians of the angles of interest, 10 exhibited no angular displacement (within errors) with one outlier.

Although the data does not demonstrate relative rotation of elastin fibres, there is strong evidence of relative movement occuring in cartilage. Intercellular strain data gathered from chondrons containing 2 or more cells has in some cases yielded significantly different data from each cell. In data where this is shown, the chondron's closest cell to the CoG has a higher strain, suggesting two important points:

1. The chondron has been 'pulled away' from the CoG relative to the surrounding ECM.

2. The chondron has not deformed in the same manner as the surrounding ECM.

The first point again suggests heterogeneity in strain at a cellular level. It is unlikely that the chondron is moving relative to local ECM, but rather that there is a strain gradient across the ECM in the vicinity of the cell. The second point has important implications for the understanding of mechanotransduction in chondrocytes, as it suggests that the cells deform relative to the surrounding ECM. Measurements of the Young's modulus of chondrocytes and PCMs using micropipette aspiration have yielded values between 0.36 kPa and 0.7 kPa, and 23 kPa and 40 kPa, respectively [80, 82]. These values are orders of magnitude below that of the bulk values of around 0.5 MPa and 15 MPa for the compressive and tensile moduli of AC, respectively. This highlights the complex method of strain transduction both in and around cells, which has been a topic of extensive

investigation (see e.g. [78, 71]). Elastin may have a role in both of these effects, as it has been noted that elastin fibres appear to attach directly to PCMs, meaning that any stresses associated to the elastin network will be applied directly to the cells. Also, the arrangement of elastin in the surface of cartilage, described in Section 5.3.1.2, often appears to cocoon groups of chondrons, and may have the potential role of transmitting potentially damaging stresses to other regions of the cartilage.

The elastin network has been shown to be highly anisotropic, and appears to be interconnected at PCMs and nodes. Elastin fibres in most samples exhibit a preferential orientation in the surface 3-5 μm and are mostly random in orientation below this point. Weak trends in the orientation of fibres to a depth of 60 μm do appear to demonstrate a correlation with the orientation of collagen leaves [1] and appear most abundant within these leaves, suggesting there may be a mechanical link between elastin and collagen. Being largely random in orientation, spread unevenly (at a cellular level) throughout the surface $\sim 175\,\mu$m of AC, and branched at average intervals of $\sim 20\,\mu$m, the elastin network must distribute stress in a highly anisotropic manner. Although the total volume fraction of elastin in AC is very small, the fraction at the surface may be significant, and so may have a role in stress transduction in that region.

The arrangement of elastin fibres provides insight into growth patterns in AC. Elastin fibres have been shown to frequently branch into two elastin fibres, and it seems reasonable to assume that the fibre has grown in the direction of the open side of the branch. No single, continuous fibres have been found that branch in both directions. There appears to be little pattern in direction of growth in elastin fibres other than at the surface where the ordered elastin fibres appear to show a trend towards the articular surface. The proliferation of cells may also be evident in some of the images, as some elastin fibres appear to have been bent around cells. The clustering of cells within elastin fibre 'capsules' at the surface may also be evidence of cell proliferation taking place faster than elastin production.

5.4.2 Relationships between Strain Distribution and Cartilage Structure

The intercellular x-strain data show clear, repeatable trends with depth. Every sample has a clear minimum in x-strain at a depth between 25 μm and 50 μm and exhibits the largest measured x-strain below this point. This minimum coincides with the mid-deep region of the Ta layer, where collagen fibres are predominantly aligned parallel to the surface and will therefore provide the largest resistance to tensile strain. The depth dependent tensile test data from Chapter 4 may explain the larger strains at the deepest

points of the stacks. The variation in the z-positions of the minima is potentially due to two factors:

- The intercellular strain results were grouped in such a way that there was an equal amount of data contributing to each point. Due to the nonuniform distribution of cells with depth, and the bias towards cells which could be seen clearly in all 3 data stacks, it is not possible to plot the data so that points line up with depth between samples. It is possible for the true position of the minima to be up to midway between the recorded minima and either of the two neighbouring points. Under this assumption there appears to be a common depth of $40\,\mu$m where all samples may have a true minimum in strain.
- The thickness of the tangential layer of AC has been shown previously to vary across the surface in the joint. The intercellular x-strain minima are likely to exist due to the tangential collagen resisting tensile forces, and their z-location is therefore likely to be dependent upon the thickness of this layer.

A potential method of improving the accuracy of the data, and assessing the contribution of each of the two points above, would be to take stacks from several different xy-locations on the sample at each state of strain and compare the strain distributions.

Trends in y-strain are much less clear, with no apparent repeatable trend in the shape of the strain distribution. The only remark that can be made about the graphs in Figure 5.12 are that the strains tend towards a similar value at a point deeper in the cartilage. Assuming each sample is exposed to the same total strain as discussed earlier, this result would suggest that the y-strain behaviour of samples is similar in deeper zones and that the majority of variations are restricted to the surface.

It follows from the Benninghoff model of collagen fibre orientation in cartilage that not only should there be a minimum in x-strain at the depths shown in Figure 5.11, but that the strain should continue to increase through the Tr layer, as the collagen still has a nonzero component in the transverse directions. The FE model in Chapter 3 predicts that the R layer has a transverse stiffness considerably smaller than the Ta layer, and this was verified by tensile testing in Chapter 4. This effect may be accentuated by the findings of the FE model of the straining method (Section 4.1), which shows that the bottom of the sample (the side stuck to the paddles) undergoes the greatest deflection. Introducing anisotropy specific to AC to the model would give a clearer picture of this effect.

It has been shown in Section 3.2 that the Ta layer of cartilage experiences considerably larger z-strain than the rest of the cartilage when loaded normally. It has also been shown

that this region is considerably stiffer in x and y than the rest of the cartilage, suggesting its function is to resist lateral expansion due to normal loading, and shear forces caused by articulation. The presence of elastin almost exclusively in the Ta layer would indicate that its role, if any, is related to these two observations. The fact that the surface layer of cartilage regularly undergoes large strains would suggest that an elastic network may be needed to maintain structure.

5.4.3 Summary

The work detailed in this chapter has provided an insight into the connectivity and deformation behaviour of AC at cellular and intercellular scales. The distribution of strain at the scale of $\sim 20\,\mu$m has been shown to be significantly different to that of $\sim 200\,\mu$m, suggesting a high degree of anisotropy in material parameters at the smaller scale. This is of great importance for understanding mechanotransduction in chondrocytes, and therefore the role of mechanical forces in cartilage metabolism. It is acknowledged that the nature of the experiments do not necessarily reflect loading *in vivo*, but cartilage in its physiological environment does experience tensile forces from lateral expansion under normal loading, and shear associated with joint articulation. This work has made steps towards understanding the role of elastin in the surface of AC, the heterogeneous, anisotropic distribution of strain at a cellular level, and the variation in composition and mechanical properties of AC across the different regions of the metacarpophalangeal joint.

There are several ways in which this work could be taken further. Experiments need to be repeated over the various other regions of the joint surface to find trends in strain distributions. If the experiment can be refined to be conducted on thin samples then it would be possible to simultaneously take SHG and TPF stacks using the epi- and forward imaging directions. SHG images provide detail about the abundance and orientation of collagen fibres, and overlaid images may provide insight into the relationship between collagen and elastin, which have been shown to co-habit the leaf structure in AC. Lastly, the addition of a force transducer and accurate strain gauge to the stretching rig in its multiphoton configuration would reduce errors associated with application of fixed strains.

Chapter 6

Conclusions and Further Work

The aims of this thesis were to investigate the mechanical properties of articular cartilage (AC) and relate them to its structure and composition. This chapter summarises the findings detailed in previous chapters, and discusses potential avenues for future work.

6.1 Summary

The mechanical properties and composition of AC have been investigated at several different length scales in this work. It was shown that consideration of the layered nature of AC (Table 3.1) is necessary to accurately describe the propagation of strain through a normally loaded sample (Figure 3.6). The incorporation of layered anisotropy based on the alignment of collagen was shown to minimise damaging stress to the articular surface as well as interfacial shear (Figure 3.7). The anisotropy in material parameters was investigated using tensile mechanical tests of thin cartilage slices, and the average tensile moduli of each layer were found (Table 4.1). Polarised light microscopy was performed on slices prior to testing (Figure 4.8), which displayed variations in the orientation of collagen with depth and location on the joint surface. There was considerable variation in the mechanical response between samples (Figure 4.9, see also Appendix A), suggesting a complex trend in the distribution of stress and strain within individual slices. This micromechanical behaviour was investigated using nonlinear microscopy to image the relative deformation of the different constituents of AC. The relative movement of cells and the reorientation of elastin fibres were used to determine the distribution of strain at two different length scales (Figures 5.13 and 5.14), and it was found that there was significant variation between the two strain values. This work highlights the highly heterogeneous and anisotropic distribution of stress and strain within AC, and demonstrates the need for mechanical models which incorporate these complexities.

6.1.1 Steady-State Mechanical Model

A finite element (FE) model was designed to determine the steady-state mechanical properties of AC under the assumption that it is either homogeneous or layered. Experimental data on the depth-dependent reorientation of collagen under load were used as a template for defining cartilage layers and calculating the propagation of strain.

It was found that although a homogeneous model could be generated which recreated the aggregate strain distribution, it would be insufficient for determining the propagation of stress and strain inside the cartilage. The suitability of the homogeneous model for cartilage depends upon the scale of interest. Determination of stress propagation through a model of an entire joint, for instance, is unlikely to be enhanced significantly by consideration of the layered structure of AC. However, the determination of stress fields through chondrocytes for the purpose of understanding mechanotransduction will require significant detail of the microscopic structure.

Incorporation of layered inhomogeneity into the model results in the internal strains being recreated accurately. It was found that the relative layer deformations were only accurately described when the Poisson's ratio was set to values between 0.05 and 0.25, which match those in the literature [112]. At these values, the von Mises stress is lowest in the tangential layer, suggesting the compressibility and compliance of surface AC results in a transfer of potentially damaging stress to the deeper layers. The compressibility of AC, particularly at the surface, will also affect the lubrication and congruence between two opposing articular surfaces in a synovial joint.

Incorporation of anisotropy into the model removes the link between the relative layer deformations and bulk modulus of the cartilage, and the results show that it is possible to recreate the strain behaviour in the experiment whilst maintaining a constant bulk modulus for the whole cartilage. The bulk modulus of cartilage is dictated by the structure and volume fractions of each of the constituents of the ECM, as well as the fixed charge density and fluid content, and is unlikely to vary as much as the layered isotropic model predicts. The anisotropic model also demonstrates improved stress propagation characteristics over the layered isotropic model, showing further reduced stresses in the surface layer and minimising interfacial shear between layers.

6.1.2 Tensile Mechanical Properties

The mechanical responses of the three layers of AC to tensile load were the topic of this investigation. Cartilage samples were obtained from three regions of different load bearing within the equine metacarpophalangeal joint, and were tested parallel and perpendicular to the split line. The tangential and transitional layers demonstrated stress-strain

behaviour typical of biological materials in tension [130], exhibiting a clear toe region followed by a region of linearity. The radial region, however, consistently demonstrated a region of strain-softening after the toe region typical of plastic deformation, but did not fail and behaved linearly at higher strains. It was found that the anisotropy in mechanical properties associated with the split line was limited to the tangential layer, where there was a $(2.4 \pm 0.2) : 1$ ratio in tensile modulus between the parallel and perpendicular directions. This is a significantly greater variation than quoted in the more recent literature (see e.g. [123]) and is in fact in line with earlier findings by Kempson et al. [124, 125]. This is due to surface samples being thin enough to be wholly contained within the tangential layer, whereas other reported tensile moduli of articular surface cartilage contain contributions from the less stiff transitional zone. The tangential layer was found to have an average tensile modulus of $31.3 \pm 2.5\,\mathrm{MPa}$, and the transitional and radial layers had tensile moduli of $17.4 \pm 1.4\,\mathrm{MPa}$ and $9.4 \pm 0.8\,\mathrm{MPa}$, respectively, which are similar to those reported by Roth and Mow [123]. The ratio in the two directional moduli and the average tensile modulus of the tangential layer are both significantly greater than values quoted in the literature for the surface layer of cartilage. This is due to the samples in this investigation being sufficiently thin ($20\,\mu\mathrm{m}$) to be wholly contained in the tangential layer, whereas the surface samples used in other reported work incorporate a significant amount of the transitional zone, which is more isotropic and compliant in tension than the tangential zone.

The mechanical responses were compared with polarised light images, which demonstrated location-specific trends in the orientation and isotropy of collagen. The tangential layer revealed thin lines of signal parallel to the split line direction which were assumed to be collagen fibre bundles. The degree of anisotropy of the tangential layer varied considerably across the surface of the cartilage, being greatest in the thick palmar cartilage. The transitional zone contained patches of different signal intensity and arrangement, which were generally between $200\,\mu\mathrm{m}$ and $400\,\mu\mathrm{m}$ across and roughly rectangular. These patches were attributed to the overlapping leaf structure of collagen, in which leaves of radially aligned collagen from the deeper cartilage bend in the transitional zone to become tangentially aligned at the surface. These leaves overlap each other at different angles and depths. The radial layer contained lines of signal which were suggested to be either the bases of collagen leaves, or signal from collagen fibrils separated by radial columns of chondrocytes. The radial layer displayed much more background signal than the other layers, suggesting the presence of a network of fibrils below the resolution of the microscope.

The locations from which samples were obtained will experience varying amounts of shear and normal force *in vivo*, and it is likely that the collagen arrangement changes to suit

the local loading environment. The thick palmar cartilage is not situated in a location of the joint which will be exposed to large normal loads under normal *in vivo* loading conditions, however the sessamoid bone articulates over the palmar region suggesting that it may experience larger shear loads. The anisotropic orientation of collagen evident throughout the depth in this region may improve its ability to resist shear forces in a particular direction. The cortical ridge is the apex of the metacarpal and is thus likely to experience the highest normal loads. The collagen in this region is considerably more isotropic at all depths in the tangential plane than other samples, this will endow the cartilage with the ability to resist lateral swelling associated with normal loading.

6.1.3 Microstructural Response to Load

Two photon fluorescence was used to image the elastin fibres and chondrocytes in AC. The aim of the investigation was to determine the distribution of strain at a microscopic level in AC by applying tensile loads to samples and taking image stacks at increasing states of strain.

The distribution of strain was measured at two scales using the stacks of images. The larger scale strain ($\sim 200\,\mu$m) was calculated by finding the average relative movement of cells, and was referred to as the intercellular strain. It was found that the average intercellular x-strain (for a strain applied in x) varied with depth, and was least at depths between $25\,\mu$m and $50\,\mu$m from the articular surface. This coincides with the middle/lower region of the tangential layer, where collagen fibres are aligned to resist the applied strain. The x-strain increased below this point as expected due to the change in orientation of collagen fibres. The y-strain in most cases was significantly greater in magnitude than the x-strain, suggesting that the Poisson's ratio $\nu_{xy} > 1$. This was attributed to the reorientation of collagen towards the direction of applied strain causing an orthogonal contraction. The reorientation and tensioning of collagen fibres resulted in some cases with them protruding from the articular surface, resulting in a corrugated pattern with periodicity of approximately $50\,\mu$m.

The smaller of the two lengthscales over which strain was calculated ($\sim 20\,\mu$m) involved calculating the reorientation of individual elastin fibres at specific points. The required strain to cause such a reorientation was referred to as the specific strain. The specific strain was found to loosely match the intercellular strain data, but there was considerable spread suggesting that there are large variations in the distribution of strain at this length scale. This result is highly significant as it means chondrocytes experience a large range of stresses and strains, which will have a considerably impact on mechanotransduction and cell metabolism. The mechanical environment of the chondrocyte has been a topic of extensive investigation, see e.g. [78, 71].

The large variation in specific strain motivated an investigation to find further evidence of differences in strain across the image stacks. It was found when analysing a chondron containing multiple cells that intercellular strains associated with each cell were significantly different, suggesting that either the chondron has moved relative to the rest of the cells in the stack, or that the deformation behaviour of the chondron is different to the extracellular matrix. This behaviour was repeated for several other chondrons containing more than one cell.

The elastin fibre network in the surface of AC has only recently been discovered [68, 66], and its function, if any, has yet to be elucidated. It was found that some fibres orientated in the y-direction lost tension at high strains, and the strain in a specific elastin fibre in an unloaded sample was calculated to be between $25\,\% \pm 5\,\%$ and $39\,\% \pm 8\,\%$. It was found that elastin fibres are interconnected at pericellular matrices and at nodes in the extracellular matrix. Fibres in the surface $3\,\mu$m to $5\,\mu$m are finer than in the deeper regions, and exhibit a high degree of order. Below this ordered layer, elastin fibres exist predominantly in the leaves of collagen between cells, suggesting there may be some connectivity between the two fibrous networks. Elastin fibres branch at average intervals of $\sim 20\,\mu$m, and the direction of branching in tangential layer fibres is usually towards the articular surface, suggesting a trend in the growth of the elastin network. Surface fibres have been seen to form cocoons around clusters of cells, which may offer some additional protection to certain loading types. Some elastin fibres appeared to be bent around chondrocytes, suggesting that chondrocyte proliferation has resulted in cells being pushed into the fibres.

6.2 Future Work

The work described in this thesis can be enhanced and taken further in many ways. The following subsections describe some ideas for future work.

6.2.1 Shear Model

The FE model described in Chapter 3 addressed the modelling of internal strains of cartilage under normal load. A transverse isotropic model was proposed for the accurate modelling of steady-state stress and strain distribution, and the determination of elastic moduli for this model was performed in Chapter 4. It was proposed in Chapter 4 that AC is suited to supporting the loads native to its location on the articular surface, and these are likely to vary in bias between shear and normal stresses. The layered FE model could be easily redesigned to test this proposal, by incorporating shear forces as well

as normal forces, and specifying material properties of each layer with the orthotropic tensile moduli calculated in the tensile test. There has been considerable research in the tribological properties of AC (see Section 1.2.1.5) and data from the literature could be used as a basis for determining applied shear and normal loads.

6.2.2 Mechanical Hysteresis Measurements of Radial Cartilage

The radial layer of AC exhibited unusual strain-softening behaviour at tensile strains of approximately 5 %. This is usually typical of plastic deformation and damage to a sample, however none of the radial samples ruptured. Tensile tests documented in the literature [123] have also shown this behaviour, and samples have continued to deform up to strains in excess of 100 % before breaking. In order to determine whether irreversible damage has occurred to these samples, hysteresis measurements need to be made. It is possible that the radial layer deforms plastically due to a reduced ability of the collagen in this region to reorientate. A comparison of the reorientation of collagen between tangential and radial layers under load could be performed using a nonlinear imaging technique such as second harmonic generation (SHG).

6.2.3 Quantifying Strain Heterogeneity

The work detailed in Chapter 5 demonstrated that the distribution of strain at the cellular (10s of microns) scale is highly heterogeneous. The analysis of strain heterogeneity could be enhanced by repeating the experiment using thinner samples, incorporating stress and strain transducers to the rig for more accurate application of strain, and performing repeats with adjacent samples. With more accurate strain data, a statistical analysis could then be performed to find the quality of fit between the specific and intercellular strains. The quality of fit could be used as a value for the strain heterogeneity. It is likely that the heterogeneity of strain increases with pathogenesis, and an understanding of this increase may provide useful information for the treatment of osteoarthritis.

6.2.4 Micromechanics Investigated with CARS, TPF and SHG

The micromechanical behaviour of AC under tensile load was investigated using TPF. The centre points of cells were used as fiducial points of reference and their relative movement was used to calculate strain. This imaging technique could not directly measure the strain experienced by cells as the lipid bilayer surrounding cells does not fluoresce at the same wavelength as elastin, and hence can not be seen in the images. Coherent anti-Stokes Raman scattering (CARS) is an imaging technique which clearly resolves the lipid bilayer

and can be performed at the same time as TPF. This would provide a means of calculating cellular strain in loaded cartilage, whilst simultaneously measuring strains in the ECM using the techniques in Chapter 5.

Another extension to the micromechanics work involves incorporating SHG, which reveals the arrangement of collagen fibres. Simultaneous TPF and SHG imaging of loaded samples could reveal more details of the connectivities of the elastin and collagen networks, as well as provide a means of more accurately determining the reorientation of collagen under load.

Appendix A

Tensile Test Results

In Chapter 4 tensile tests of thin slices of articular cartilage were performed. Samples were taken from three locations on the articular surface of the metacarpal in the metacarpophalangeal joint, from three different horses. Samples were obtained from the tangential, transitional and radial layers and tested parallel and perpendicular to the split line. The results are displayed in Figure 4.9 and discussed in Section 4.4. To maintain flow of the chapter, the results and trendlines were fitted to a single page. Larger versions of the graphs without the trendlines are displayed in figures over the next three pages.

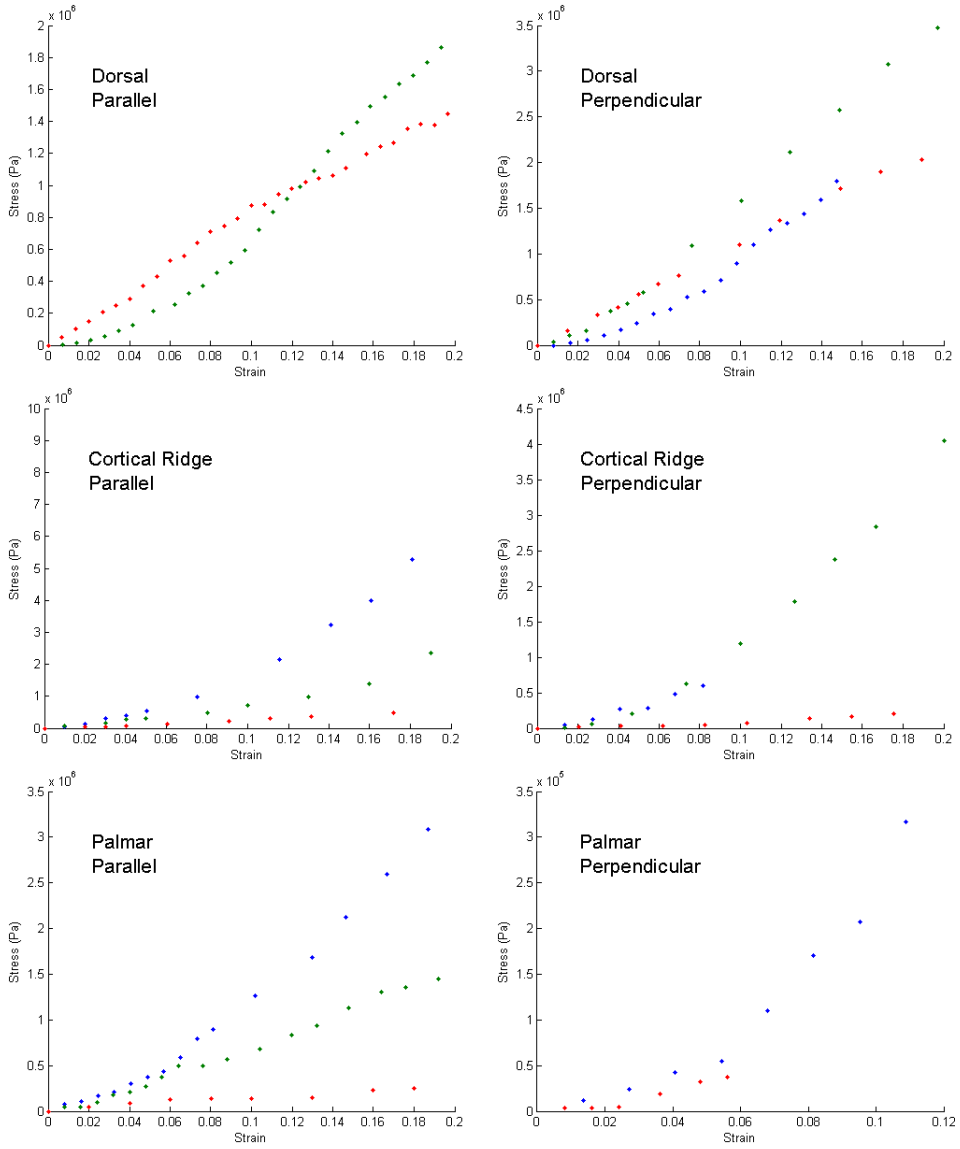

Figure A.1: Stress-strain data for tensile test sample 1. The blue points correspond to tangential layer data, the green points correspond to transitional layer data, and the red points correspond to radial layer data. Samples were obtained from the labelled regions on the metacarpal surface of the equine metacarpophalangeal joint. The cartilage was strained parallel to the split line (left) and perpendicular to the split line (right).

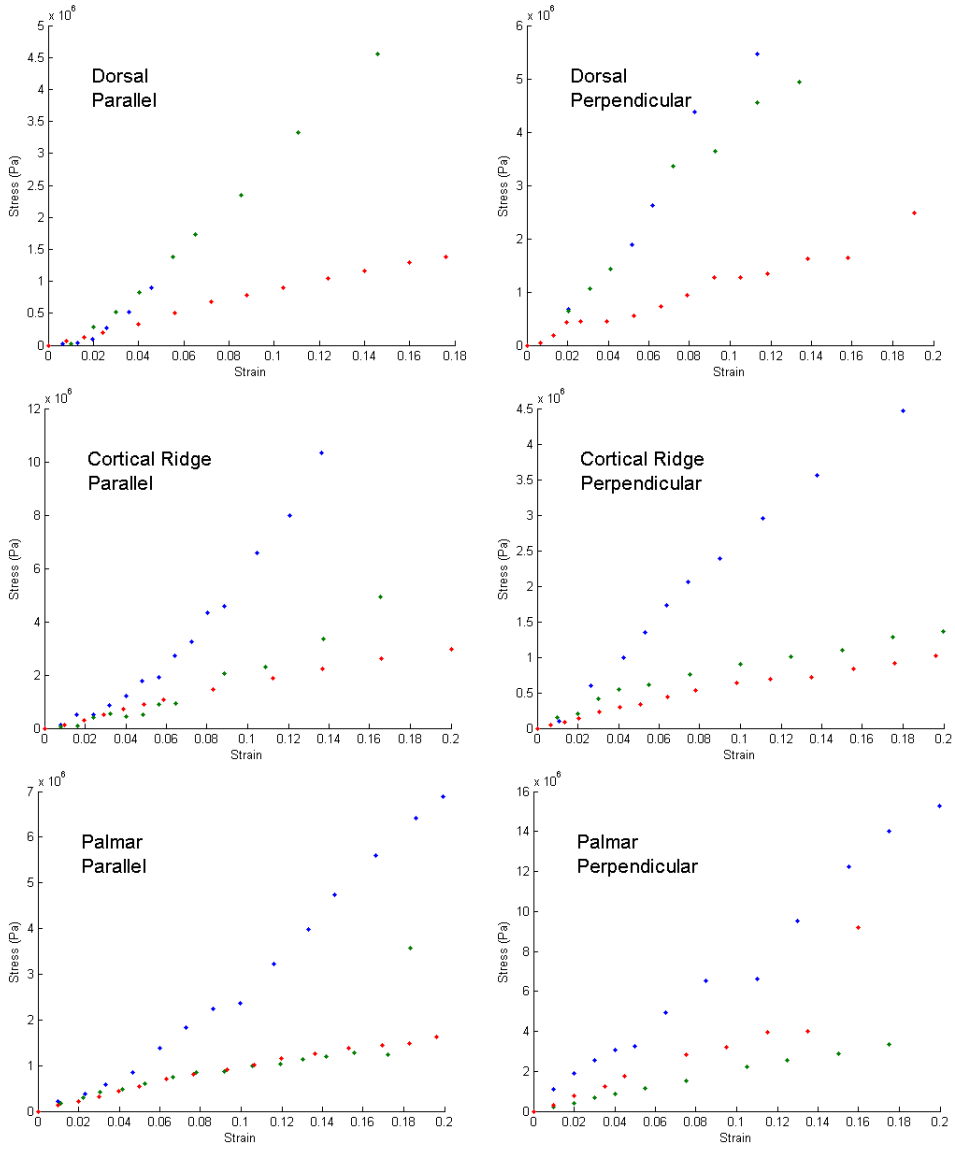

Figure A.2: Stress-strain data for tensile test sample 2. The blue points correspond to tangential layer data, the green points correspond to transitional layer data, and the red points correspond to radial layer data. Samples were obtained from the labelled regions on the metacarpal surface of the equine metacarpophalangeal joint. The cartilage was strained parallel to the split line (left) and perpendicular to the split line (right).

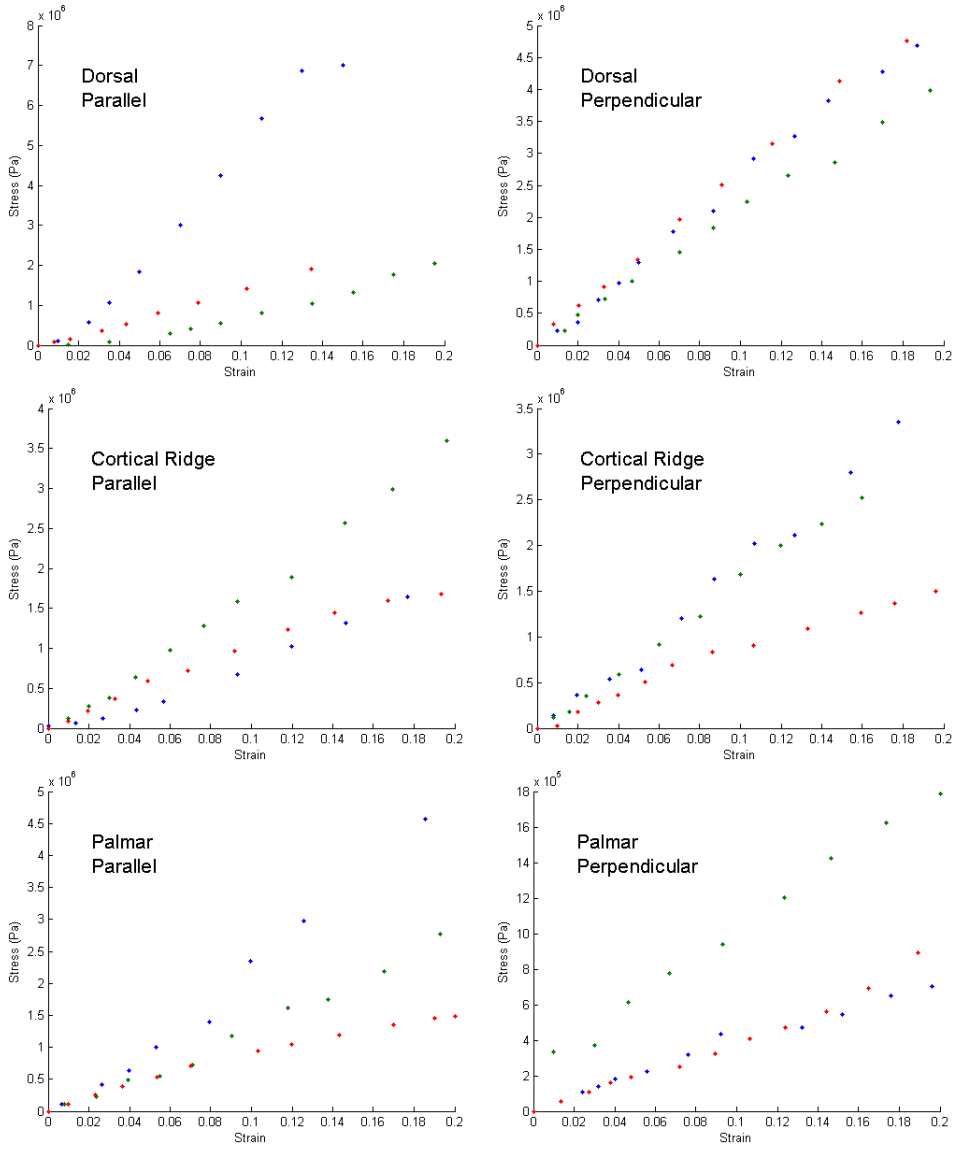

Figure A.3: Stress-strain data for tensile test sample 3. The blue points correspond to tangential layer data, the green points correspond to transitional layer data, and the red points correspond to radial layer data. Samples were obtained from the labelled regions on the metacarpal surface of the equine metacarpophalangeal joint. The cartilage was strained parallel to the split line (left) and perpendicular to the split line (right).

Bibliography

[1] J. M. Mansour. *Kinesiology: the mechanics and pathomechanics of human movement*, chapter Biomechanics of cartilage, pages 66–79. Lippincott Williams & Wilkins, 2004.

[2] A. Maroudas. Balance between swelling pressure and collagen tension in normal and degenerate cartilage. *Nature*, 260(5554):808–809, 1976.

[3] N. Boudreau and M. J. Bissell. *Extracellular matrix*, chapter Regulation of gene expression by the extracellular matrix, pages 246–261. Harwood Academic, 1996.

[4] F. H. Martini. *Fundamentals of anatomy and physiology.* Prentice Hall, London, fifth edition, 2001.

[5] R. A. Stockwell. *Biology of cartilage cells.* Cambridge University Press, 1979.

[6] A. Benninghoff. Form and bau der gelenkknorpel in ihren beziehungen zur funktion. ii: Der aufbau des gelenkkorpels in seinen beziehungen zur funktion. *Z. Zellforsch Mikr. Anat*, 2:783–862, 1925.

[7] C. J. Moger, R. Barrett, P. Bleuet, D. A. Bradley, R. E. Ellis, E. M. Green, K. M. Knapp, P. Muthuvelu, and C. P. Winlove. Regional variations of collagen orientation in normal and diseased articular cartilage and subchondral bone determined using small angle x-ray scattering (saxs). *Osteoarthritis and Cartilage*, 15(6):682–687, 2007.

[8] M. T. Bayliss, M. Venn, A. Maroudas, and S. Y. Ali. Structure of proteoglycans from different layers of human articular-cartilage. *Biochem. J.*, 209(2):387–400, 1983.

[9] M. F. Venn. Variation of chemical composition with age in human femoral head cartilage. *Annals of the Rheumatic Diseases*, 37(2):168–174, 1978.

[10] P. L. Mente and J. L. Lewis. Elastic modulus of calcified cartilage is an order of magnitude less than that of subchondral bone. *Journal of Orthopaedic Research*, 12:637–647, 1994.

[11] T. Lyons, S. McClure, R. Stoddart, and J. McClure. The normal human chondro-osseous junctional region: evidence for contact of uncalcified cartilage with subchondral bone and marrow spaces. *BMC Musculoskeletal Disorders*, 7(1):52, 2006.

[12] A. Maroudas, J. Mizrahi, and E. Benaim. A study of compressive properties of cartilage using unconfined compression: example of an experimental and a theoretical approach. In R. Read, N.G. Machale, J. L. Bert, C. P. Winlove, and G.A. Laine, editors, *Interstitium, connective tissue and lymphatics*, Interstitium, Conective tissue and lymphatics, pages 55–65. Portland Press, London, 1995.

[13] S. Kamalanathan and N. D. Broom. The biomechanical ambiguity of the articular surface. *Journal of Anatomy*, 183:567–578, 1993.

[14] Y. C. Fung. *Biomechanics Mechanical Properties of Living Tissues*. Springer-Verlag New York Inc., 1981.

[15] K. E. Kadler, D. F. Holmes, J. A. Trotter, and J. A. Chapman. Collagen fibril formation. *Biochem. J.*, 316(1):1–11, 1996.

[16] S. Pataridis, A. Eckhardt, K. Mikulikova, P. Sedlakova, and I. Miksik. Identification of collagen types in tissues using hplc-ms/ms. *Journal of Separation Science*, 31: 3483–3488, 2008.

[17] V. Mow and W. M. Lai. Mechanics of animal joints. *Annual Review of Fluid Mechanics*, 11:247–288, 1979.

[18] A. Nerlich, I. Wiest, and K. von der Mark. Immunohistochemical analysis of interstitial collagens in cartilage of different stages of osteoarthrosis. *Virchows Archiv B Cell Pathology Zell-pathologie*, 63:249–255, 1993.

[19] N. Boos, A. G. Nerlich, I. Wiest, K. von der Mark, R. Ganz, and M. Aebi. Immunohistochemical analysis of type x-collagen expression in osteoarthritis of the hip joint. *Journal of Orthopaedic Research*, 17(4):495–502, 1999.

[20] M. Nimni and K. Deshmukh. Differences in collagen metabolism between normal and osteoarthritic human articular cartilage. *Science*, 181:751–752, 1973.

[21] C. W. Smith, I. S. Young, and J. N. Kearney. Mechanical properties of tendons: Changes with sterilization and preservation. *Journal of Biomechanical Engineering-Transactions of the Asme*, 118(1):56–61, 1996. J. Biomech. Eng.-Trans. ASME.

[22] H. Muir, P. Bullough, and A. Maroudas. The distribution of collagen in human articular cartilage with some of its physiological implications. *Journal of Bone and Joint Surgery*, 52B:554–563, 1970.

[23] J. M. Clark. The organization of collagen fibrils in the superficial zones of articular-cartilage. *Journal of Anatomy*, 171:117–130, 1990.

[24] M. J. Kaab, K. Ito, J. M. Clark, and H. P. Notzli. Deformation of articular cartilage collagen structure under static and cyclic loading. *Journal of Orthopaedic Research*, 16(6):743–751, 1998.

[25] P. Bullough and J. Goodfellow. The significance of the fine structure of articular cartilage. *J Bone Joint Surg Br*, 50(4):852–7, 1968.

[26] W. Hultkrantz. Uber die spaltrichtungen der gelenkknorpel. *Verh Anat Ges*, 12: 248–256, 1898.

[27] R. M. Aspden and D. W. L. Hukins. Collagen organization in articular-cartilage, determined by x- ray-diffraction, and its relationship to tissue function. *Proceedings of the Royal Society of London Series B-Biological Sciences*, 212(1188):299–304, 1981.

[28] C. J. Moger, K. P. Arkill, R. Barrett, P. Bleuet, R. E. Ellis, E. M. Green, and C. P. Winlove. Cartilage collagen matrix reorientation and displacement in response to surface loading. *Journal of Biomechanical Engineering-Transactions of the Asme*, 131(3):031008, 2009.

[29] N. D. Broom, T. Ngo, and E. Tham. Traversing the intact/fibrillated joint surface: a biomechanical interpretation. *Journal of Anatomy*, 206(1):55–67, 2005.

[30] M. H. Chen and N. D. Broom. Concerning the ultrastructural origin of large-scale swelling in articular cartilage. *Journal of Anatomy*, 194:445–461, 1999.

[31] T. Reinert, U. Reibetanz, J. Vogt, T. Butz, A. Werner, and W. Grunder. Visualisation of collagen fibrils in joint cartilage using stim. *Nuclear Instruments and Methods in Physics Research Section B: Beam Interactions with Materials and Atoms*, 181 (1-4):511–515, 2001.

[32] P. Julkunen, P. Kiviranta, W. Wilson, J. S. Jurvelin, and R. K. Korhonen. Characterization of articular cartilage by combining microscopic analysis with a fibril-reinforced finite-element model. *Journal of Biomechanics*, 40(8):1862–1870, 2007.

[33] J. C. Mansfield, C. P. Winlove, J. Moger, and S. J. Matcher. Collagen fiber arrangement in normal and diseased cartilage studied by polarization sensitive nonlinear microscopy. *Journal of Biomedical Optics*, 13:044020, 2008.

[34] P. A. Torzilli, D. A. Dethmers, D. E. Rose, and H. F. Schryuer. Movement of interstitial water through loaded articular-cartilage. *Journal of Biomechanics*, 16 (3):169–179, 1983.

[35] C. P. Winlove and K. H. Parker. *Interstitium, connective tissue and lymphatics*, chapter The physiological functions of extracellular matrix macromolecules, pages 137–166. Portland Press, 1995.

[36] T. E. Hardingham and H. Muir. Hyaluronic acid in cartilage and proteoglycan aggregation. *Biochemical Journal*, 139(3):565–581, 1974.

[37] L. Rosenberg, W. Hellmann, and A. K. Kleinschmidt. Electron microscopic studies of proteoglycan aggregates from bovine articular cartilage. *Journal of Biological Chemistry*, 250(5):1877–1883, 1975.

[38] A. Maroudas. Physicochemical properties of cartilage in the light of ion exchange theory. *Biophysical Journal*, 8:575–595, 1968.

[39] V. C. Mow, A. Ratcliffe, and A. R. Poole. Cartilage and diarthrodial joints as paradigms for hierarchical materials and structures. *Biomaterials*, 13(2):67–97, 1992.

[40] S. Ehrlich, N. Wolff, R. Schneiderman, A. Maroudas, K. H. Parker, and C. P. Winlove. The osmotic pressure of chondroitin sulphate solutions: Experimental measurements and theoretical analysis. *Biorheology*, 35:383–397, 1998.

[41] S. R. Eisenberg and A. J. Grodzinsky. Swelling of articular-cartilage and other connective tissues - electromechanochemical forces. *Journal of Orthopaedic Research*, 3(2):148–159, 1985.

[42] A. J. Grodzinsky, V. Roth, E. Myers, W. D. Grossman, and V. C. Mow. The significance of electromechanical and osmotic forces in the nonequilibrium swelling behavior of articular cartilage in tension. *Journal of Biomechanical Engineering*, 103:221–231, 1981.

[43] A. Maroudas, E. Wachtel, G. Grushko, E. P. Katz, and P. Weinberg. The effect of osmotic and mechanical pressures on water partitioning in articular-cartilage. *Biochimica Et Biophysica Acta*, 1073(2):285–294, 1991.

[44] N. D. Broom and A. Oloyede. The importance of physicochemical swelling in cartilage illustrated with a model hydrogel system. *Biomaterials*, 19(13):1179–1188, 1998.

[45] V. C. Mow and W. M. Lai. Recent developments in synovial joint biomechanics. *Siam Review*, 22(3):275–317, 1980.

[46] A. Maroudas. *Adult articular cartilage*, chapter Physicochemical properties of articular cartilage, pages 215–290. Pitman Medical, 1979.

[47] H. Lipshitz, R. Etheredge, and M. J. Glimcher. Changes in the hexosamine content and swelling ratio of articular cartilage as functions of depth from the surface. *The Journal of Bone and Joint Surgery*, 58(8):1149–1153, 1976.

[48] M. Venn and A. Maroudas. Chemical composition and swelling of normal and osteoarthrotic femoral head cartilage. i. chemical composition. *Annals of the Rheumatic Diseases*, 36(2):121, 1977.

[49] J. A. Buckwalter and L. C. Rosenberg. Electron microscopic studies of cartilage proteoglycans. *Electron microscopy reviews*, 1(1):87–112, 1988.

[50] E. Garcia-Seco, D. A. Wilson, J. L. Cook, K. Kuroki, J. M. Kreeger, and K. G. Keegan. Measurement of articular cartilage stiffness of the femoropatellar, tarsocrural, and metatarsophalangeal joints in horses and comparison with biochemical data. *Veterinary Surgery*, 34(6):571–578, 2005.

[51] X. L. Lu, D. D. N. Sun, X. E. Guo, F. H. Chen, W. M. Lai, and V. C. Mow. Indentation determined mechanoelectrochemical properties and fixed charge density of articular cartilage. *Annals of Biomedical Engineering*, 32(3):370–379, 2004.

[52] T. G. Myers, G. K. Aldis, and S. Naili. Ion-induced deformation of soft-tissue. *Bulletin of Mathematical Biology*, 57(1):77–98, 1995.

[53] J. E. Scott. Proteoglycan-collagen interactions. *Ciba Foundation Symposia*, 124: 104–124, 1986.

[54] N. D. Broom and R. Flachsmann. Physical indicators of cartilage health: the relevance of compliance, thickness, swelling and fibrillar texture. *Journal of Anatomy*, 202(6):481–494, 2003.

[55] C. W. McCutchen. The frictional properties of animal joints. *Wear*, 5(1):1–17, 1962.

[56] P. Julkunen, T. Harjula, J. Marjanen, H. J. Helminen, and J. S. Jurvelin. Comparison of single-phase isotropic elastic and fibril-reinforced poroelastic models for indentation of rabbit articular cartilage. *Journal of Biomechanics*, 42(5):652–656, 2009.

[57] C. G. Armstrong and V. C. Mow. Variations in the intrinsic mechanical properties of human articular cartilage with age, degeneration, and water content. *Journal of Bone & Joint Surgery*, 64:88–94, 1982.

[58] M. A. Soltz and G. A. Ateshian. Experimental verification and theoretical prediction of cartilage interstitial fluid pressurization at an impermeable contact interface in confined compression. *Journal of biomechanics*, 31(10):927–934, 1998.

[59] V. C. Mow, G. A. Ateshian, W. M. Lai, and W. Y. Gu. Effects of fixed charges on the stress-relaxation behavior of hydrated soft tissues in a confined compression problem. *International Journal of Solids and Structures*, 35(34-35):4945–4962, 1998.

[60] R. Flachsmann, N. D. Broom, and A. E. Hardy. Deformation and rupture of the articular surface under dynamic and static compression. *Journal of Orthopaedic Research*, 19(6):1131–1139, 2001.

[61] E. G. Cleary and M. A. Gibson. *Extracellular matrix*, volume 2, chapter Elastic tissue, elastin and elastin associated microfibrils, pages 95–140. Harwood Academic, 1996.

[62] D. W. Urry. *Elastin and Elastases*, chapter Physicochemical Properties of Elastin and Constituent Peptides, pages 141–174. Florida CRC Press Inc., 1989.

[63] R. P. Mecham and E. C. Davis. *Extracellular Matrix Assembly and Structure*, chapter Elastic Fiber Structure and Assembly, pages 281–314. Academic Press, 1994.

[64] J. M. Davidson. *Connective Tissue Disease: Molecular Pathology of the Extracellular Matrix*, chapter Elastin: Structure and Biology, pages 29–53. CRC Press, 1986.

[65] I. Hesse. The occurrence of elastic system fibers in the matrix of normal articular-cartilage. *Cell and Tissue Research*, 248(3):589–593, 1987.

[66] J. Mansfield, J. Yu, D. Attenburrow, J. Moger, U. Tirlapur, J. Urban, Z. Cui, and C. Winlove. The elastin network: its relationship with collagen and cells in articular cartilage as visualized by multiphoton microscopy. *Journal of Anatomy*, 215:682–691, 2009.

[67] A. Naumann, J. E. Dennis, A. Awadallah, D. A. Carrino, J. M. Mansour, E. Kastenbauer, and A. I. Caplan. Immunochemical and mechanical characterization of cartilage subtypes in rabbit. *The Journal of Histochemistry & Cytochemistry*, 50: 1049–1058, 2002.

[68] A. T. Yeh, M. J. Hammer-Wilson, D. C. Van Sickle, H. P. Benton, A Zoumi, B. J. Tromberg, and G. M. Peavy. Nonlinear optical microscopy of articular cartilage. *Osteoarthritis and Cartilage*, 13:345–352, 2005.

[69] I. C. Clarke. Articular cartilage: a review and scanning electron microscope study: 1. the interterritorial fibrillar architecture. *Journal of Bone & Joint Surgery, British Volume*, 53(4):732–750, 1971.

[70] R. Honner and R. C. Thompson. The nutritional pathways of articular cartilage: an autoradiographic study in rabbits using 35s injected intravenously. *The Journal of Bone and Joint Surgery*, 53(4):742–748, 1971.

[71] A. J. Grodzinsky, M. E. Levenston, M. Jin, and Eliot H. Frank. Cartilage tissue remodelling in response to mechanical forces. *Annual Review of Biomedical Engineering*, 2:691–713, 2000.

[72] I. Kiviranta, M. Tammi, J. Jurvelin, A. Saamanen, and H. J. Helminen. Moderate running exercise augments glycosaminoglycans and thickness of articular cartilage in the knee joint of young beagle dogs. *Journal of Orthopaedic Research*, 6:188–195, 1988.

[73] J. J. Parkkinen, M. J. Lammi, H. J. Helminen, and M. Tammi. Local stimulation of proteoglycan synthesis in articular cartilage explants by dynamic compression in vitro. *Journal of Orthopaedic Research*, 10:610–620, 1992.

[74] M. Wong, P. Wuethrich, M. D. Buschmann, P. Eggli, and E. Hunziker. Chondrocyte biosynthesis correlates with local tissue strain in statically compressed ardult articular cartilage. *Journal of Orthopaedic Research*, 15:189–196, 1997.

[75] R. L. Mauck, S. L. Seyhan, G. A. Ateshian, and C. T. Hung. Influence of seeding density and dynamic deformational loading on the developing structure/function relationships of chondrocyte-seeded agarose hydrogels. *Annals of Biomedical Engineering*, 30:1046–1056, 2002. ISSN 0090-6964.

[76] M. D. Buschmann, Y. A. Gluzband, A. J. Grodzinsky, and E. B. Hunziker. Mechanical compression modulates matrix biosynthesis in chondrocyte/agarose culture. *Journal of Cell Science*, 108:1497–1508, 1995.

[77] K. W. Ng, C. C.-B. Wang, R. L. Mauck, T.-A. N. Kelly, N. O. Chahine, K. D. Costa, G. A. Ateshian, and C. T. Hung. A layered agarose approach to fabricate depth-dependent inhomogeneity in chondrocyte-seeded constructs. *Journal of Orthopaedic Research*, 23:134–141, 2005.

[78] C. A. Poole. Articular cartilage chondrons: Form, function and failure. *Journal of Anatomy*, 191:1–13, 1997. J. Anat.

[79] F. Guilak, W. R. Jones, H. P. Ting-Beall, and G. M. Lee. The deformation behavior and mechanical properties of chondrocytes in articular cartilage. *Osteoarthritis and Cartilage*, 7(1):59–70, 1999.

[80] F. Guilak, L. G. Alexopoulos, M. A. Haider, H. P. Ting-Beall, and L. A. Setton. Zonal uniformity in mechanical properties of the chondrocyte pericellular matrix:

Micropipette aspiration of canine chondrons isolated by cartilage homogenization. *Annals of Biomedical Engineering*, 33(10):1312–1318, 2005.

[81] R. K. Korhonen and W. Herzog. Depth-dependent analysis of the role of collagen fibrils, fixed charges and fluid in the pericellular matrix of articular cartilage on chondrocyte mechanics. *Journal of Biomechanics*, 41(2):480–485, 2008.

[82] L. G. Alexopoulos, L. A. Setton, and F. Guilak. The biomechanical role of the chondrocyte pericellular matrix in articular cartilage. *Acta Biomaterialia*, 1(3): 317–325, 2005.

[83] J. Draper. *Encyclopedia of the Horse*, chapter Principle Horse Breeds, pages 42–71. Peerage Books, 1977.

[84] J. Barker. *Encyclopedia of the Horse*, chapter Principle Pony Breeds, pages 72–87. Peerage Books, 1977.

[85] C. W. McIlwraith. Current concepts in equine degenerative joint disease. *Journal of American Veterinary Medical Association*, 180:239–250, 1982.

[86] C. M. Riggs. Osteochondral injury and joint disease in the athletic horse. *Equine Veterinary Education*, 18:100–112, 2006.

[87] P. D. Rossdale. *Encyclopedia of the horse*, chapter The health of the horse, pages 200–210. Peerage Books, 1985.

[88] E. M. Röck S. Budras, K.-D. Sack. *Anatomy of the horse: An illustrated text.* Schlütersche GmbH & Co., 2001.

[89] N. Smith. *Easy steps to riding and horse care.* Regency House Publishing, 1996.

[90] M. Langford. *Story of photography.* Focal Press, 1997.

[91] P. A. J. Brama, D. Karssenberg, A. Barneveld, and P. R. van Weeren. Contact areas and pressure distribution on the proximal articular surface of the proximal phalanx under sagittal plane loading. *Equine Veterinary Journal*, 33(1):26–32, 2001.

[92] S. Akizuki, V. C. Mow, F. Muller, J. C. Pita, D. S. Howell, and D. H. Manicourt. Tensile properties of human knee joint cartilage: I. influence of ionic conditions, weight bearing, and fibrillation on the tensile modulus. *Journal of Orthopaedic Research*, 4(4):379–392, 1986.

[93] R. E. Outerbridge. The etiology of chondromalacia patellae. *Journal of Bone Joint Surgery*, 43B:752–757, 1961.

[94] H. Lipiello L. Zarins A. Mankin, H. J. Dorfman. Biochemical and metabolic abnormalities in articular cartilage from osteo-arthritic human hips: Ii. correlation of morphology with biochemical and metabolic data. *Journal of Bone & Joint Surgery*, 53:523–537, 1971.

[95] C. M. Thomas, C. J. Fuller, C. E. Whittles, and M. Sharif. Chondrocyte death by apoptosis is associated with cartilage matrix degradation. *Osteoarthritis and Cartilage*, 15(1):27–34, 2007.

[96] M. A. Haider. A radial biphasic model for local cell-matrix mechanics in articular cartilage. *SIAM Journal on Applied Mathematics*, 64:1588–1608, 2004.

[97] L. Wan and G. A. Li. *In-vivo cartilage contact biomechanics: An experimental and computational investigation of human ankle joint complex*. PhD thesis, Massachusetts Institute of Technology Dept. of Physics, 2008.

[98] D. Holderbaum, T. M. Haqqi, and R. W. Moskowitz. Genetics and osteoarthritis - exposing the iceberg. *Arthritis and Rheumatism*, 42(3):397–405, 1999.

[99] K. M. O'Connor. Unweighting accelerates tidemark advancement in articular cartilage at the knee joint of rats. *Journal of Bone and Mineral Research*, 12(4):580–589, 1997.

[100] R. B. Salter, D. F. Simmonds, B. W. Malcolm, E. J. Rumble, D. MacMichael, and N. D. Clements. The biological effect of continuous passive motion on the healing of full-thickness defects in articular cartilage: An experimental investigation in the rabbit. *The Journal of Bone and Joint Surgery*, 62(8):1232–1251, 1980.

[101] A. J. Grodzinsky, E. H. Frank, Y.-J. Kim, and M. D. Buschmann. *Extracellular matrix*, chapter The role of specific macromolecules in cell-matrix interactions and matrix function: Physicochemical and mechanical mediators of chondrocyte biosynthesis, pages 310–334. Harwood Academic, 1996.

[102] B. B. Seedholm, T. Takeda, M. Tsubuku, and V. Wright. Mechanical factors and patellofemoral osteoarthrosis. *Annals of the Rheumatic Diseases*, 38(4):307–316, 1979.

[103] V. C. Mow, M. H. Holmes, and W. M. Lai. Fluid transport and mechanical properties of articular cartilage: A review. *Journal of Biomechanics*, 17:377–394, 1984.

[104] V. C. Mow, S. C. Kuei, W. M. Lai, and C. G. Armstrong. Biphasic creep and stress-relaxation of articular-cartilage in compression - theory and experiments. *Journal of Biomechanical Engineering-Transactions of the Asme*, 102(1):73–84, 1980.

[105] W. Y. Gu, H. Yao, C. Y. Huang, and H. S. Cheung. New insight into deformation-dependent hydraulic permeability of gels and cartilage, and dynamic behavior of agarose gels in confined compression. *Journal of Biomechanics*, 36(4):593–598, 2003.

[106] M. A. Soltz and G. A. Ateshian. Interstitial fluid pressurization during confined compression cyclical loading of articular cartilage. *Annals of Biomedical Engineering*, 28(2):150–159, 2000.

[107] R. M. Schinagl, D. Gurskis, A. C. Chen, and R. L. Sah. Depth-dependent confined compression modulus of full-thickness bovine articular cartilage. *Journal of Orthopaedic Research*, 15(4):499–506, 1997.

[108] S. S. Chen, Y. H. Falcovitz, R. Schneiderman, A. Maroudas, and R. L. Sah. Depth-dependent compressive properties of normal aged human femoral head articular cartilage: relationship to fixed charge density. *Osteoarthritis and cartilage*, 9(6): 561–569, 2001.

[109] J. S. Jurvelin, M. D. Buschmann, and E. B. Hunziker. Optical and mechanical determination of poisson's ratio of adult bovine humeral articular cartilage. *Journal of Biomechanics*, 30(3):235–241, 1997.

[110] L. Li, J. Cheung, and W. Herzog. Three-dimensional fibril-reinforced finite element model of articular cartilage. *Medical and Biological Engineering and Computing*, 47 (6):607–615, 2009.

[111] J. S. Jurvelin, J. P. A. Arokoski, E. B. Hunziker, and H. J. Helminen. Topographical variation of the elastic properties of articular cartilage in the canine knee. *Journal of Biomechanics*, 33(6):669–675, 2000.

[112] V. C. Mow and X. E. Guo. Mechano-electrochemical properties of articular cartilage: Their inhomogeneities and anisotropies. *Annual Review of Biomedical Engineering*, 4(1):175–209, 2002.

[113] C. C. B. Wang, N. O. Chahine, C. T. Hung, and G. A. Ateshian. Optical determination of anisotropic material properties of bovine articular cartilage in compression. *Journal of Biomechanics*, 36(3):339–353, 2003.

[114] L. Sokoloff. Elasticity of articular cartilage: effect of ions and viscous solutions. *Science*, 141:1055–1057, 1963.

[115] S. H. Park, R. Krishnan, S. B. Nicoll, and G. A. Ateshian. Cartilage interstitial fluid load support in unconfined compression. *Journal of Biomechanics*, 36(12): 1785–1796, 2003.

[116] S. Naili, C. Oddou, and D. Geiger. A method for the determination of mechanical parameters in a porous elastically deformable medium: Applications to biological soft-tissues. *International Journal of Solids and Structures*, 35(34-35):4963–4979, 1998.

[117] J. Toyras, T. Lyyra-Laitinen, M. Niinimaki, R. Lindgren, M. T. Nieminen, I. Kiviranta, and J. S. Jurvelin. Estimation of the young's modulus of articular cartilage using an arthroscopic indentation instrument and ultrasonic measurement of tissue thickness. *Journal of Biomechanics*, 34(2):251–256, 2001.

[118] L. M. Herrmann G. Mockros L. F. Hayes, W. C. Keer. A mathematical analysis for indentation tests of articular cartilage. *Journal of Biomechanics*, 5:541–551, 1972.

[119] J. R. Parsons and J. Black. Mechanical behavior of articular cartilage: quantitative changes with alteration of ionic environment. *Journal of Biomechanics*, 12(10): 765–773, 1979.

[120] M. L. Hall, D. A. Krawczak, N. K. Simha, and J. L. Lewis. Effect of dermatan sulfate on the indentation and tensile properties of articular cartilage. *Osteoarthritis and Cartilage*, 17(5):655–661, 2009.

[121] R. C. Appleyard, D. Burkhardt, P. Ghosh, R. Read, M. Cake, M. V. Swain, and G. A. C. Murrell. Topographical analysis of the structural, biochemical and dynamic biomechanical properties of cartilage in an ovine model of osteoarthritis. *Osteoarthritis and Cartilage*, 11(1):65–77, 2003.

[122] A. F. Mak, W. M. Lai, and V. C. Mow. Biphasic indentation of articular cartilage - i. theoretical analysis. *Journal of Biomechanics*, 20:703–714, 1987.

[123] V. Roth and V. C. Mow. The intrinsic tensile behavior of the matrix of bovine articular cartilage and its variation with age. *The Journal of Bone and Joint Surgery*, 62(7):1102–1117, 1980.

[124] G. E. Kempson, M. A. R. Freeman, and S. A. V. Swanson. Tensile properties of articular cartilage. *Nature*, 220(5172):1127–1128, 1968.

[125] G. E. Kempson, H. Muir, C. Pollard, and M. Tuke. The tensile properties of the cartilage of human femoral condyles related to the content of collagen and glycosaminoglycans. *Biochimica et Biophysica Acta (BBA) - General Subjects*, 297 (2):456–472, 1973.

[126] S. Woo, W. H. Akeson, and G. F. Jemmott. Measurements of nonhomogeneous, directional mechanical properties of articular cartilage in tension. *Journal of Biomechanics*, 9(12):785–791, 1976.

[127] S. L. Y. Woo, P. Lubock, M. A. Gomez, G. F. Jemmott, S. C. Kuei, and W. H. Akeson. Large deformation nonhomogeneous and directional properties of articular cartilage in uniaxial tension. *Journal of Biomechanics*, 12(6):437–446, 1979.

[128] Astm standard d3039/d3039m - 07 standard test method for tensile properties of polymer matrix composite materials, 2008. URL `www.astm.org`.

[129] Y. Sasazaki, R. Shore, and B. B. Seedhom. Deformation and failure of cartilage in the tensile mode. *Journal of Anatomy*, 208(6):681–694, 2006.

[130] Y. C. B. Fung. Elasticity of soft tissues in simple elongation. *American Journal of Physiology*, 213(6):1532–1544, 1967.

[131] J. Katta, Z. Jin, E. Ingham, and J. Fisher. Biotribology of articular cartilage - a review of the recent advances. *Medical Engineering & Physics in Medicine and Biology*, 30:1349 – 1363, 2008.

[132] G. A. Ateshian. The role of interstitial fluid pressurization in articular cartilage lubrication. *Journal of Biomechanics*, 42(9):1163–1176, 2009.

[133] C. W. McCutchen. Sponge-hydrostatic and weeping bearings. *Nature*, 184:1284–1285, 1959.

[134] P. R. Lewis and C. W. McCutchen. Experimental evidence for weeping lubrication in mammalian joints. *Nature*, 184:1285, 1959.

[135] C. W. McCutchen. More on weeping lubrication: Experiments with hydron, a micropourous polyhydroxyalkylacrylic ester resin. In V Wright, editor, *Lubrication and wear in joints*, pages 117–121. Biological Engineering Society, Sector Publishing Ltd., 1969.

[136] Q. T. Nguyen, B. L. Wong, J. Chun, Y. C. Yoon, F. E. Talke, and R. Sah. Macroscopic assessment of cartilage shear: Effects of counter-surface roughness, synovial fluid lubricant, and compression offset. *Journal of Biomechanics*, 43:1787–1793, 2010.

[137] H. Forster and J. Fisher. The influence of loading time and lubricant on the friction of articular cartilage. *Proceedings of the Institution of Mechanical Engineers, Part H*, 210:109–119, 1996.

[138] H. Forster and J. Fisher. The influence of continuous sliding and subsequent surface wear on the friction of articular cartilage. *Proceedings of the Institution of Mechanical Engineers, Part H*, 213:329–345, 1999.

[139] T. A. Schmidt, N. S. Gastelum, Q. T. Nguyen, B. L. Schumacher, and R. L. Sah. Boundary lubrication of articular cartilage: Role of synovial fluid constituents. *Arthritis and Rheumatism*, 56:882–891, 2007.

[140] T. A. Schmidt and R. L. Sah. Effect of synovial fluid on boundary lubrication of articular cartilage. *Osteoarthritis and Cartilage*, 15:35–47, 2007.

[141] P. Kumar, M. Oka, J. Toguchida, M. Kobayashi, E. Uchida, T. Nakamura, and K. Tanaka. Role of uppermost superficial surface layer of articular cartilage in the lubrication mechanism of joints. *Journal of Anatomy*, 199:241–250, 2001.

[142] J. Katta, Z. Jin, E. Ingham, and J. Fisher. Effect of nominal stress on the long term friction, deformation and wear of native and glycosaminoglycan deficient articular cartilage. *Osteoarthritis and Cartilage*, 17(5):662–668, 2009.

[143] E. I. Drewniak, G. D. Jay, B. C. Fleming, and J. J. Crisco. Comparison of two methods for calculating the frictional properties of articular cartilage using a simple pendulum and intact mouse knee joints. *Journal of Biomechanics*, 42(12):1996–1999, 2009.

[144] S. L. Graindorge and G. W. Stachowiak. Changes occurring in the surface morphology of articular cartilage during wear. *Wear*, 241(2):143–150, 2000.

[145] G. R. Higginson, M. R. Litchfield, and J. Snaith. Load-displacement-time characteristics of articular-cartilage. *International Journal of Mechanical Sciences*, 18 (9-10):481–486, 1976.

[146] W. C. Hayes and A. J. Bodine. Flow-independent viscoelastic properties of articular cartilage matrix. *Journal of Biomechanics*, 11(8-9):407–419, 1978.

[147] R. K. June, K. L. Mejia, J. R. Barone, and D. P. Fyhrie. Cartilage stress-relaxation is affected by both the charge concentration and valence of solution cations. *Osteoarthritis and Cartilage*, 17(5):669–676, 2009.

[148] W. Wilson, C. C. van Donkelaar, B. van Rietbergen, K. Ito, and R. Huiskes. Stresses in the local collagen network of articular cartilage: A poroviscoelastic fibril-reinforced finite element study. *Journal of Biomechanics*, 37:357–365, 2004.

[149] W. Wilson, C. C. van Donkelaar, B. van Rietbergen, K. Ito, and R. Huiskes. Erratum to: Stresses in the local collagen network of articular cartilage: a poroviscoelastic fibril-reinforced finite element study (vol 37, pg 357, 2004). *Journal of Biomechanics*, 38(10):2138–2140, 2005.

[150] G. Limbert and J. Middleton. A transversely isotropic viscohyperelastic material - application to the modeling of biological soft connective tissues. *International Journal of Solids and Structures*, 41(15):4237–4260, 2004.

[151] A. F. Mak. The apparent viscoelastic behavior of articular-cartilage - the contributions from the intrinsic matrix viscoelasticity and interstitial fluid-flows. *Journal of Biomechanical Engineering-Transactions of the Asme*, 108(2):123–130, 1986.

[152] S. C. Cowin. A recasting of anisotropic poroelasticity in matrices of tensor components. *Transport in Porous Media*, 50(1-2):35–56, 2003.

[153] S. C. Cowin and M. M. Mehrabadi. Compressible and incompressible constituents in anisotropic poroelasticity: The problem of unconfined compression of a disk. *Journal of the Mechanics and Physics of Solids*, 55(1):161–193, 2007.

[154] R. E. Craine, A. E. Green, and P. M. Naghdi. A mixture of viscous elastic materials with different constituent temperatures. *Quarterly Journal of Mechanics and Applied Mathematics*, 23:171–184, 1970.

[155] R. M. Bowen. Incompressible porous media models by use of theory of mixtures. *International Journal of Engineering Science*, 18:1129–1148, 1980.

[156] Y. Lu. *Theoretical studies on the transport of fluid and solutes in soft tissues and across biological membranes.* PhD thesis, Queen Mary, University of London, 2006.

[157] W. M. Lai and V. C. Mow. Drag-induced compression of articular-cartilage during a permeation experiment. *Biorheology*, 17(1-2):111–123, 1980.

[158] W. M. Lai, J. S. Hou, and V. C. Mow. A triphasic theory for the swelling and deformation behaviors of articular-cartilage. *Journal of Biomechanical Engineering-Transactions of the Asme*, 113(3):245–258, 1991.

[159] D. N. Sun, W. Y. Gu, X. E. Guo, W. M. Lai, and V. C. Mow. A mixed finite element formulation of triphasic mechano-electrochemical theory for charged, hydrated biological soft tissues. *International Journal for Numerical Methods in Engineering*, 45(10):1375–1402, 1999.

[160] M. A. Bhatti. *Fundamental finite element analysis and applications.* John Wiley and Sons, 2005.

[161] E Hecht. *Optics.* Addison-Wesley, 1998.

[162] A. Diaspro and C. J. R. Sheppard. Two-photon excitation flouresence microscopy. In Alberto Diaspro, editor, *Confocal and two-photon microscopy: Foundations, applications and advances*, pages 39–73. Wiley-Liss Inc., 2002.

[163] R. Richards-Kortum, R. Drezek, K. Sokolov, I. Pavlova, and M. Pollen. Survey of endogenous biological fluorophores. *Handbook of biomedical fluorescence*, pages 237–264, 2003.

[164] L. Hsu, K. H. Kim, C. Y. Dong, P. Kaplan, T. Hancewicz, C. Buehler, K. Berland, B. R. Masters, and P. T. C. So. *Confocal and two-photon microscopy: Foundations, applications and advances*, chapter Two-Photon Imaging of Tissue Physiology Based on Endogenous Fluorophore, pages 431–448. Wiley-Liss Inc., 2002.

[165] J. A. Palero, H. S. de Bruijn, A. V. van den Heuvel, H. J. C. M. Sterenborg, and H. C. Gerritsen. Spectrally resolved multiphoton imaging of in vivo and excised mouse skin tissues. *Biophysical Journal*, 93:992–1007, 2007.

[166] J. Rieppo, J. Hallikainen, J. S. Jurvelin, I. Kiviranta, H. J. Helminen, and M. M. Hyttinen. Practical considerations in the use of polarized light microscopy in the analysis of the collagen network in articular cartilage. *Microscopy Research and Technique*, 71(4):279–287, 2008.

[167] A. Verteramo and B. B. Seedhom. Zonal and directional variations in tensile properties of bovine articular cartilage with special reference to strain rate variation. *Biorheology*, 41:203–213, 2004.

[168] P. A. J. Brama, J. Holopainen, P. R. van Weeren, E. C. Firth, H. J. Helminen, and M. M. Hyttinen. Effect of loading on the organization of the collagen fibril network in juvenile equine articular cartilage. *Journal of Orthopaedic Research*, 27: 1226–1234, 2009.

[169] P. S. Eggli, E. B. Hunziker, and R. K. Schenk. Quantitation of structural features characterizing weight- and less-weight bearing regions in articular cartilage: a stereological analysis of medial femoral condyles in young adult rabbits. *The Anatomical Record*, 222:217–227, 1988.

[170] C. Glaser and R. Putz. Functional anatomy of articular cartilage under compressive loading quantitative aspects of global, local and zonal reactions of the collagenous network with respect to the surface integrity. *Osteoarthritis and Cartilage*, 10(2): 83–99, 2002.

[171] F. Guilak, A. Ratcliffe, and V. Mow. Chondrocyte deformation and local tissue strain in articular cartilage: A confocal microscopy study. *Journal of Orthopaedic Research*, 13:410–421, 1995.

[172] J. Rieppo, M. M. Hyttinen, E. Halmesmaki, H. Ruotsalainen, A. Vasara, I. Kiviranta, J. S. Jurvelin, and H. J. Helminen. Changes in spatial collagen content

and collagen network architecture in porcine articular cartilage during growth and maturation. *Osteoarthritis and Cartilage*, 17(4):448–455, 2009.

[173] L. J. Gibson, M. F. Ashby, G. S. Schajer, and C. I. Robertson. The mechanics of two-dimensional cellular materials. *Proceedings of the Royal Society of London Series A*, 382:25–42, 1982.